

dc_11_10

MTA doktori értekezés

CELL AND LIPID MEMBRANE STRUCTURES.
EFFECTS OF ELECTRIC, THERMAL AND CHEMICAL
INTERACTIONS

István P. Sugár

New York, 2010

Table of Contents

Introductory Notes	5
1. <u>Effect of electric field on the structure of cell membranes</u>	
1.1. <u>Stochastic theory of cell electroporation</u>	
1.1.1. Introduction	6
1.1.2. The model	6
1.1.2.1. General pore structure	7
1.1.2.2. The stochastic variable	7
1.1.2.3. Transition probabilities	8
1.1.2.4. Free energy function at zero electric field	9
1.1.2.5. Free energy function in the presence of an electric field	9
1.1.2.6. Master equations of electroporation	10
1.1.3. Results and discussion	11
1.1.3.1. Stationary solutions	11
1.1.3.1.1. Reversible electroporation in stable membranes	13
1.1.3.2. Quasi-stationary solutions	13
1.1.3.2.1. Mechanical breakdown, reversible and irreversible electroporation	14
1.1.3.3. Nonstationary solutions	14
1.1.3.3.1. Time delay of mechanical breakdown – Membrane lifetime	15
1.1.3.3.2. Time delay of electroporation	16
1.1.3.4. Transition kinetics	18
1.1.3.4.1. Poreless \rightleftharpoons Porous transition	18
1.1.3.5. Membrane rupture	19
1.1.3.5.1. Resealing process	19
1.2. <u>Phenomenological theory of low voltage electroporation</u>	
1.2.1. Introduction	20
1.2.2. Model	23
1.2.2.1. Geometry of the model of low voltage electroporator	23
1.2.2.2. Laplace equation of the model of low voltage electroporator	25
1.2.2.2.1. Boundary conditions	25
1.2.2.2.2. Laplace equation in inhomogeneous medium	26
1.2.2.2.3. The matching conditions	26
1.2.2.2.4. Numerical solution of the Laplace equation	26
1.2.3. Results	26
1.2.4. Discussion	29
1.2.4.1. Transmembrane voltage	29
1.2.4.2. Distribution of electropores	32
1.2.4.3. Electric field and potential	33
1.2.4.4. Minimal applied voltage	35
1.2.4.5. Efficiency of electroporation	36
1.2.5. Conclusions	37
1.2.6. Appendix 1 - Joule Heating in LVEP	37
1.2.7. Appendix 2 - Estimation of the thickness of the narrow passage	39
1.2.8. Appendix 3 - On the deviations of the model's geometry from the electroporator's geometry	40

<u>2. Effect of temperature and composition on the structure of two-component lipid membranes</u>	
2.1. Introduction	42
2.2. Lattice model of DMPC/DSPC bilayers	43
2.2.1. Lattice geometry, states and configuration	43
2.2.2. Configurational energy and degeneracy	45
2.2.3. Configurational probability	46
2.2.4. Steps in the Monte Carlo simulations	46
2.2.5. Generation of trial configurations	47
2.2.5.1. Local state alteration	47
2.2.5.2. Exchanging different molecules	47
2.2.5.3. Reorientation of a pair of nearest-neighbor molecules	47
2.2.6. Decision making	47
2.2.7. Defining the Monte Carlo cycle	48
2.2.8. Global state alteration	48
2.2.9. Determination of the model parameters	49
2.3. Results and discussion	50
2.3.1. System size and type of transition	50
2.3.2. Excess heat capacity curves and melting curves	52
2.3.3. Domain structure of the membranes	55
2.3.4. Cluster statistics	56
2.3.5. Cluster number	58
2.3.6. Cluster percolation	59
2.3.7. 'Small' clusters	61
2.3.8. Membrane permeability	63
2.4. Conclusions	65
<u>3. Lipid monolayer structure controls protein adsorption. Model of peripheral protein adsorption to the water/lipid interface</u>	
3.1. Introduction	66
3.2. The model	68
3.2.1. Structure of PL/DG monolayers	68
3.2.2. Free area and discrete molecular area	69
3.2.3. Characterization of monolayer configuration	70
3.2.4. The normalized initial adsorption rate	71
3.2.5. Probability density of free area under a colipase - p_f	72
3.2.6. Probability density of discrete area of uncomplexed molecules under a colipase - p_u	73
3.2.7. Numerical integration	74
3.3. Results and discussion	74
3.3.1. Protein adsorption to POPC monolayers	74
3.3.2. Protein adsorption to DO/POPC monolayers	75
3.3.3. Protein adsorption to DO/POPC monolayers at collapse pressure	77
3.4. Conclusions	79
3.5. Appendix 1 - <i>Definitions of frequently used symbols</i>	79
3.6. Appendix 2 - The probability density that the free area of n lipid molecules is f	80
3.7. Appendix 3 - Calculation of A_{CP} and q	81

3.8. Appendix 4	82	
3.8.1. Incomplete beta function and the binomial distribution	82	
3.8.2. Extensions of the incomplete beta function	84	
4. <u>Membrane geometry regulates intercellular communication. Model of autocrine/paracrine signaling in epithelial layer</u>		
4.1. Introduction	86	
4.2. Model	87	
4.2.1. Model geometry	87	
4.2.2. Diffusion equation of the model	89	
4.2.3. Numerical Solution of the Diffusion Equation	90	
4.3. Results and discussion	92	
4.3.1. Plot types of trapping site distributions	92	
4.3.2. Ligands emission from the top of a microvillus	93	
4.3.2.1. Geometrical parameters g and d decrease simultaneously, while $g = d$	93	
4.3.2.2. Geometrical parameter g decreases gradually, while d remains constant	95	
4.3.3. Ligand emission from the side of a microvillus	97	
4.3.4. Probability of autocrine signaling	99	
4.4. Conclusions	102	
4.5. Appendix 1	102	
4.6. Appendix 2	105	
4.7. Appendix 3 - Calculating the area accessible for ligand absorption		107
5. References		
5.1. References to Chapter 1.1.	109	
5.2. References to Chapter 1.2.	109	
5.3. References to Chapter 2.	110	
5.4. References to Chapter 3.	112	
5.5. References to Chapter 4.	113	

Introductory Notes

The structure of a cell membrane determines its functions. By changing the external conditions one can change the membrane structure and consequently its functions. The work presented here intends to demonstrate these simple statements on four different membranes: single cell membrane, lipid vesicle, lipid monolayer and epithelial layer. We reveal the physical mechanism of how external fields, such as electric field or temperature, are able to change the membrane structure (Sec. 1, 2). In these cases the external conditions result in the structural and consequently the functional changes. In other cases the cell itself can change either the composition or geometry of its membrane that result in functional changes (Sec. 4).

The theoretical models presented here are so called minimal models. The assumptions made by these models are both physically and biologically plausible and absolutely necessary for the correct description of the observed phenomena. As a consequence the number of model parameters is minimal and the parameters have explicit physical meaning. The unique feature of this approach is that experimental data are utilized to estimate the values of the model parameters. In contrast to ab-initio calculations development of these minimal models assume close collaboration with the experimentalists.

The mathematical approach utilized in the model depends on the studied system and the questions that we intend to answer. The kinetics of electropore formation is described by using the theory of stochastic processes (Sec. 1.1). Membrane heterogeneity or equilibrium lateral distribution of membrane components is described by means of Monte Carlo simulation techniques (Sec. 2). In the cases of systems with complicated overall geometries, such as the distorted cell shape in low voltage electroporator or the rugged surface of the epithelial layer, we use numerical methods to solve the respective partial differential equations (Sec. 1.2, 4).

A model that is able to describe a broad range of experiments has predictive power. One becomes able to calculate yet un-measured or currently un-measurable properties of the system. For example the model of two-component phospholipid membranes reveals the size distribution and even the inner structure of the compositional clusters (Sec. 2), while experimentally we are able to detect only the large clusters in the micrometer range.

It is important to emphasize that besides the purely theoretical values the presented work can lead to applications in medical- and biotechnology. For example low voltage electroporation, that is discussed in Sec. 1.2 is the most promising method for ex-vivo cell transfection by foreign gene.

1. Effect of electric field on the structure of cell membranes

1.1 Stochastic theory of cell electroporation

1.1.1. Introduction

In 1972 Neumann and Rosenheck¹ discovered the permeabilization of lipid vesicles when a certain threshold value of the field strength is exceeded. The electrically induced permeability increase, called electroporation, leads to transient exchange of matter across the perturbed membrane structures. An important aspect of electric field effects on membrane structures is the artificial transfer of macromolecules or particles into the interior of biological cells and organelles. Super-critical electric fields can be used to transfect culture cells in suspension with foreign genes.

Two basic mechanisms have been suggested to describe the experimentally observed properties of electroporation: the electromechanical model and the statistical model of pore expansion. These models have been reviewed by Dimitrov and Jain². This chapter develops an exactly solvable statistical model of electroporation for one-component planar lipid bilayer membrane. At zero electric field, the membrane is populated with microscopic pores by the fluctuation clustering of vacancies (i.e. lipid molecule-free sites) in the bilayer. Under the effect of transmembrane electric field, the average pore size increases. The driving force of the electric field-mediated pore opening is associated with the enhancement of the electric polarization of the solvent molecules during their transfer from the bulk solvent space to the region of the larger electric field spreading from the pore wall into the solution of the pore interior (see Fig.1 and Sugar and Neumann³; Powell et al.⁴).

The characteristic features of the present model are the following: (1) the model results are valid independently from the molecular details of the pore structure; (2) the phenomena of electroporation are described quantitatively in the case of both stable and metastable planar bilayer membranes when the transmembrane voltage is changed stepwise; (3) the uniform description of reversible and irreversible electroporation and mechanical breakdown is presented; exact solutions of the stochastic equations of the electroporation are determined; (5) the pores are considered to be independent from each other. The consequences of pore-pore interaction, pore coalescence, and integral proteins are discussed elsewhere⁵. The results of the model are compared with the available experimental data, such as membrane lifetime, critical transmembrane voltage, and membrane conductance during the resealing process.

1.1.2. Model

On the basis of energetic considerations, different pore structures have been proposed: hydrophobic pore and inverted pore model⁶, and periodic block model³. The description of the present electroporation model does not require a detailed knowledge of the pore structure.

1.1.2.1. General Pore Structure

The following general pore properties are assumed in the model (Fig. 1): (1) A common feature of every pore model is that the water-filled pore interior is surrounded by the pore wall, and the pore wall is surrounded by the bulk bilayer lipid membrane. The structure of the lipid molecules within the pore wall is different from the bilayer structure of the bulk membrane. Consequently the specific energy of the pore wall is different from that of the bulk membrane. (2) During the pore opening and closing process, the number of lipid molecules within the pore wall increases and decreases, respectively. In the case of planar membranes, lipid transfer into the pore wall takes place simultaneously from both monolayers of the bilayer membrane. However, it is assumed that the sites of these two transfer processes along the pore circumference are independent of each other.

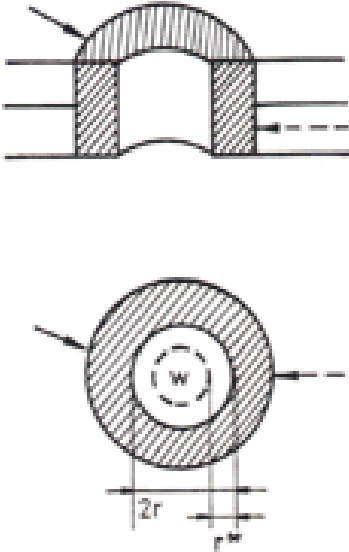


Figure 1. Side and top views of the general pore structure. The water-filled pore interior (w) is surrounded by the pore wall (shaded area), which in turn is surrounded by the bulk bilayer lipid membrane. r is the pore radius; r^* is the thickness of the region of the larger electric field; solid and dashed arrows show possible sites of lipid transfer from the upper and lower monolayer of the bilayer to the pore wall, respectively

1.1.2.2. The Stochastic Variable

Assuming circular pore geometry, both the state of the pore and the process of electroporation can be described by one stochastic variable, a . This variable is proportional to the number of lipid molecules in the pore wall. The stochastic variable a and the pore radius r are related by:

$$a = INT(2r\pi/l) \quad (1)$$

where INT integer part of a numerical value $p.qrs$, e.g., $INT(p.qrs) = p$, and l is the characteristic length along the pore circumference. The value of the characteristic length depends on the molecular structure of the pore wall. For example, in the case of the periodic block model³, l is twice the cross-sectional diameter of a lipid molecule.

(see Eq.1); β is the proportionality constant. Since the sites of transfer from or to the two layers of the bilayer to or from the pore wall are independent (see Section 1.1.2.1), the square of $\beta[a+0.5]$ gives the thermodynamic probability of the activated pore between a and $a+1$ states.

1.1.2.4. Free Energy Function at Zero Electric Field

According to the nucleation theory of bilayer stability^{8,9} at zero electric field, the free energy change of the membrane/solution system when a single pore of radius r forms is

$$\Delta G(r) = -r^2 \pi (\mu_b - \mu_s) / A_0 + 2r\pi\gamma \quad (6)$$

Where μ_s and μ_b are the chemical potential of the monomer lipid molecule in the solution (s) and in the bilayer membrane (b), respectively; A_0 is the cross-sectional area of a lipid molecule. The second term is the energy expended on the creation of the pore wall; γ is the energy of the pore wall per unit length. When $\Delta\mu = (\mu_b - \mu_s) < 0$, the free energy change $\Delta G(r)$ increases with increasing pore radius. In this case, pores of any size tend to shrink and the bilayer is stable with respect to rupture. However, in the case of $\Delta\mu > 0$ the $\Delta G(r)$ function decreases from a certain pore radius r_c ; if $r < r_c$ the pore tends to shrink and the bilayer is metastable with respect to rupture; if $r > r_c$ the pore can grow spontaneously and the bilayer is unstable.

The chemical potential difference, and consequently the bilayer stability, depends on the monomer lipid concentration C in the solution. Denoting C_e as the concentration where $\Delta\mu = 0$ and denoting CMC as the critical micelle concentration⁸, then the bilayer is stable when $C_e < C < CMC$. The bilayer is metastable when $C < C_e < CMC$ or $C < CMC < C_e$.

Although experimental data are not available on stable planar bilayers, the model calculations were performed for stable systems. These calculations have biological relevance because the electroporation of the stable planar bilayer should be analogous to the electroporation of giant lipid vesicles¹⁰ or to the electroporation of the protein-free domains of cell membranes (see Section 1.1.3.1).

1.1.2.5. Free Energy Function in the Presence of an Electric Field

In the presence of a transmembrane electric field, one has to introduce additional energy terms into the free energy function (Eq.6) describing the change in the electric polarization energy of the system $\Delta G_{el}(r)$ when a single pore of radius r forms in the bilayer³. If $r < r^*$

$$\Delta G_{el}(r) = 0.5\epsilon_0(\epsilon_m - \epsilon_w)\pi r^2 dE_m^2 \quad (7)$$

If $r > r^*$

$$\Delta G_{el}(r) = 0.5\epsilon_0\pi dE_m^2[(\epsilon_m - 1)r^2 - (\epsilon_w - 1)(r^2 - \{r - r^*\}^2)] \quad (8)$$

In Eq.7 and 8, d is the bilayer thickness, E_m is the electric field strength in the bilayer, and ε_0 , ε_m , and ε_w are the vacuum dielectric permittivity, relative dielectric permittivity of the membrane, and relative dielectric permittivity of water, respectively. During the derivation of Eqs.7 and 8, the following assumptions were made.

- (1) At higher ionic strengths ($>0.1M$), the electric conductivity of the aqueous solution is so much larger than that of the planar bilayer that the applied voltage U only drops across the bilayer. In terms of the constant field approximation, the average field in the bilayer is given by $E_m = U/d$; the field strength in the bulk electrolyte may be approximated by $E_s \cong 0$.
- (2) The electric field within the solvent-filled pore is inhomogeneous, decreasing from the value $E_m (=U/d)$ at the pore wall/solvent interface toward the pore center. In the layer of solvent molecules adjacent to the inner cylindrical part of the pore wall of thickness r^* , the field intensity is approximated by $E_p = E_m$ (Fig.1). For larger pores where $r > r^*$, the electric field strength in the central region of radius $r - r^*$ is considered to be $E_s \cong 0$. For small pores where $r < r^*$, the homogeneous field approximation $E_p \cong E_m$ holds. According to Jordan¹¹, at 1M ionic strength the electric field becomes highly inhomogeneous if $r > d/5$. For these conditions, the relation $r^* \cong d/5$ specifies the largest pore size to which the small-pore field approximation $E_p = E_m$ may be applied. In the case of oxidized cholesterol membranes, $d = 3.3nm$ (Benz et al.¹²). Thus, $r^* = 0.86nm$ at 0.1M ionic strength; r^* increases with decreasing ionic strength¹¹.

Introducing the pore state a , defined in Eq.1, into Eqs.6-8, the Gibbs free energy function is given by $\Delta\bar{G}(a) = \Delta G(a) + \Delta G_{el}(a)$; see the transition probability functions in Eqs.2-5. Eqs. 2-8 permit the calculation of the transition probabilities as a function of the pore state and transmembrane voltage. For this purpose, the numerical values characteristic to the oxidized cholesterol bilayer we utilized¹²; $\gamma = 1.25 \cdot 10^{-11} N$ (Abidor et al.⁶), $l = 1.8nm$ (Sugar and Neumann³), $T = 313K$, $\varepsilon_m = 2.1$, $\varepsilon_w = 80$. The calculations were performed with three values of $\Delta\mu/A_0 (= \Delta g)$: -0.001, 0.0, and 0.001 N/m . These values are typical for stable and metastable bilayers¹³, respectively.

1.1.2.6. Master Equations of Electroporation

The probability $P_{a,a_0}(t + \Delta t)$ of occurrence of a pore state a at time $t + \Delta t$ if the state is a_0 at time $t = 0$ is given by

$$P_{a,a_0}(t + \Delta t) = \bar{w}_{a-1} \Delta t P_{a-1,a_0}(t) + \bar{w}_{a+1} \Delta t P_{a+1,a_0}(t) + (1 - [\bar{w}_a + \bar{w}_a] \Delta t) P_{a,a_0}(t) \quad (9)$$

This difference equation may be transformed into the forward master equation⁷:

$$dP_{a,a_0}(t)/dt = \bar{w}_{a-1} P_{a-1,a_0}(t) + \bar{w}_{a+1} P_{a+1,a_0}(t) - [\bar{w}_a + \bar{w}_a] P_{a,a_0}(t) \quad (10)$$

1.1.3. Results and Discussion

Since the transition probabilities \vec{W}_a and \bar{W}_a in the master equation of the electroporation (Eq.10) are nonlinear functions of the pore state a , no general solution is possible. However, one can determine the exact stationary and quasi-stationary solutions, the lifetime of the metastable membrane, the kinetics of pore opening and closing as well as other parameters.

1.1.3.1. Stationary Solutions

If the pore state a is confined in the $(0, a^*)$ interval, the stationary pore size distribution $P_{a,a_0}(t = \infty)$ can be determined by means of Eq.11 in Table 1. The different solutions of the master equations (Eq.10) in Table 1 were taken from Goel and Richter-Dyn⁷.

Table 1. Expressions for the Equilibrium Distribution $P_{a,a_0}(\infty)$ and for the First Passage Time $T_{a,a_0}^{(1)}$

$0 \leq a_0 \leq a^*$	$P_{a,a_0}(\infty) = \frac{\vec{W}_0 \vec{W}_1 \dots \vec{W}_{a-1}}{\vec{W}_1 \vec{W}_2 \dots \vec{W}_a} \bigg/ \sum_{i=1}^{a^*} \frac{\vec{W}_0 \vec{W}_1 \dots \vec{W}_{i-1}}{\vec{W}_1 \vec{W}_2 \dots \vec{W}_i} \quad (11)$
$0 \leq a_0 \leq a < \infty$	$T_{a,a_0}^{(1)} = \sum_{i=a_0}^{a-1} \sum_{n=0}^i \vec{W}_n^{-1} \prod_{n+1,i} \quad (12)$
$0 \leq a < a_0 < a^*$	$T_{a_0,a}^{(1)} = \sum_{i=a_0}^{a^*-1} \sum_{n=a+1}^i \vec{W}_n^{-1} \prod_{n+1,i} R_{a,n} - R_{a,a_0} \sum_{i=a+1}^{a^*-1} \sum_{n=a+1}^i \vec{W}_n^{-1} \prod_{n+1,i} R_{a,n} \quad (13)$
$0 \leq a < a_0 < \infty$	$T_{a_0,a}^{(1)} = \sum_{i=a+1}^{a_0} M_{i-1,i} \quad (14)$

$$\prod_{i,j} = \frac{\vec{W}_i \vec{W}_{i+1} \dots \vec{W}_j}{\vec{W}_i \vec{W}_{i+1} \dots \vec{W}_j} \text{ if } i \leq j \text{ and } \prod_{i,i-1} = 1$$

$$R_{a,a_0} = \sum_{i=a_0}^{a^*-1} \prod_{a+1,i} \bigg/ \sum_{i=a}^{a^*-1} \prod_{a+1,i}$$

$$M_{i-1,i} = \frac{1}{\vec{W}_i} + \frac{\vec{W}_i}{\vec{W}_i \vec{W}_{i+1}} + \frac{\vec{W}_i \vec{W}_{i+1}}{\vec{W}_i \vec{W}_{i+1} \vec{W}_{i+2}} + \dots$$

Physically, the upper limit of the pore size is comparable to the membrane size itself, i.e., $a^* = \infty$ is a good approximation. In the case of *stable membranes*, the infinite sum in Eq.11 is convergent. The logarithm of the pore state distributions are shown in Fig. 2a at different transmembrane voltages. At subcritical electric fields ($U < U_{cr}^s = 0.4V$), the pore size distribution is unimodal with a cusplike maximum at $a=0$. This maximum of the distribution curve defines a phase termed the poreless phase of the stable bilayer. At supercritical electric fields ($U > U_{cr}^s = 0.4V$), the pore size distribution has two maxima: one at $a=0$ represents the poreless phase and one at $a>0$ defines the so-called porous

phase of the membrane. When the maximum belonging to the porous phase exceeds the cusplike maximum at the poreless phase, the membrane lipids form pore walls almost exclusively. In the frame of our independent pore model, this loose net structure of the membrane *is still stable*. This is a transmembrane voltage-induced phase transition of the membrane from the poreless phase into the porous phase.

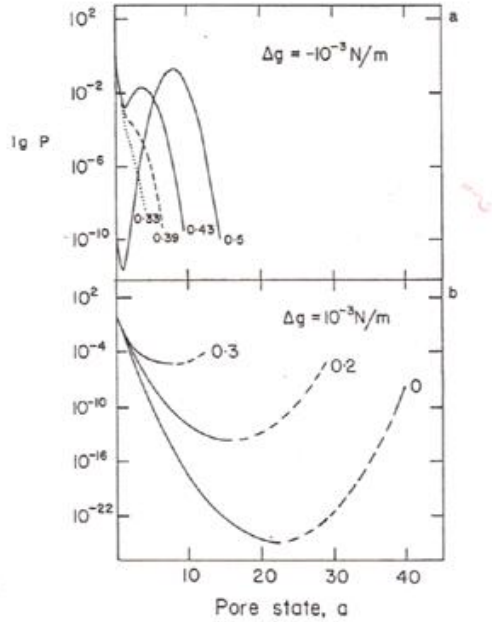


Figure 2. Stationary and quasi-stationary pore state distributions at different transmembrane voltages. a) Stable membrane (dashed and dotted line: $U < U_{cr}^s$, solid line: $U > U_{cr}^s$; b) metastable membrane (solid line: quasi-stationary pore state distribution. Beginning of dashed line defines a^* - the limit state of the quasi-stationary pores.)

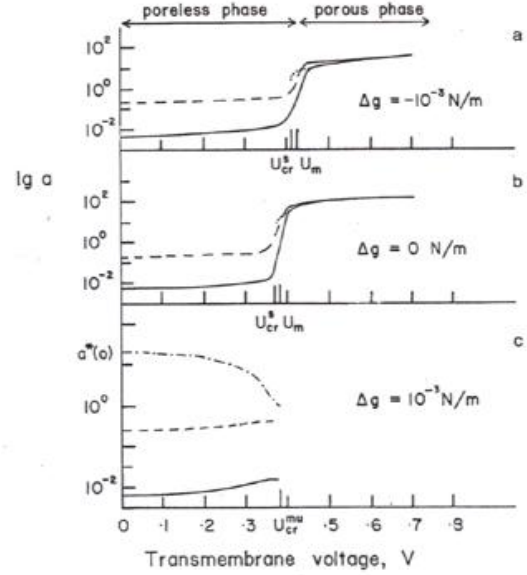


Figure 3. Characteristic quantities of electroporation as a function of transmembrane voltage. a),b) Stable membranes; c) metastable membrane. Solid line: average pore state calculated by Eq.15; dashed line: pore state fluctuation calculated by Eq.16; dotted line: the most probable state of the porous phase; dash-dotted line: limit state of quasi-stationary pores, a^* .

In Fig. 3a and b, characteristic values of the pore state distribution curves are plotted as a function of transmembrane voltage. The solid lines represent the average pore state calculated by

$$\langle a \rangle = \sum_{a=0}^{a^*} a P_{a,a_0}(t = \infty) \quad (15)$$

The average pore state sharply changes at the transition voltage U_m defined by the voltage where $d\langle a \rangle / dU$ is maximal. The transition voltage decreases with increasing Δg (see Fig. 3a,b), while the width of the phase transition remains about 0.05V. The

broken lines show the deviation of the pore states from the average value at large fluctuations, as calculated by

$$\langle a \rangle + 3\langle \Delta a \rangle = \langle a \rangle + 3 \cdot \left[\sum_{a=0}^{a^*} (a - \langle a \rangle)^2 P_{a,a_0}(\infty) \right]^{1/2} \quad (16)$$

During the phase transition, the relative pore state fluctuation ($\langle \Delta a \rangle / \langle a \rangle$) drops by two orders of magnitude! The dotted lines show the most probable state in the porous phase. The porous phase appears at the critical voltage, U_{cr}^s , and the size of the pores increases with increasing transmembrane voltage. In this voltage range, the *membrane acts as a filter*, where the pore size is in the nanometer range and can be regulated by the transmembrane voltage.

1.1.3.1.1. Reversible Electroporation in Stable Membranes

The poreless-porous phase transition is reversible. Upon application of supercritical voltage, opening of the pores takes place, resulting in the equilibrium porous phase. Upon switching off the field, coherent resealing of the pores starts immediately (see Sec. 1.1.3.4).

Electroporation measurements have not been performed on stable planar lipid bilayer membranes. However, phenomenologically a large unilamellar vesicle or the protein-free domain of a cell membrane may be analogous to a stable planar bilayer. This is the case because the free energy change of a large vesicle $\Delta G_v(r) = \gamma 2r\pi$ increases with increasing pore radius³ which is the criterion of stability. Comparing $\Delta G_v(r)$ with Eq.6, we get $\Delta g = 0$ N/m for large vesicles. In the case of large unilamellar DPPC vesicles, the critical transmembrane voltage was found to be 0.25 V (Teissie and Tsong¹⁴) and 1.1-1.8 V (Needham and Hochmuth¹⁰) while according to the model $U_{cr}^s = 0.36V$ (Fig.3b).

1.1.3.2. Quasi-Stationary Solutions

In the case of *metastable membranes*, the infinite sum in Eq.11 is divergent, i.e., there is *no stationary state* of a metastable system. However, one can define the *quasi-stationary pore size distribution* if the free energy barrier $\Delta \bar{G}(r_c)$ is much higher than the thermal energy unit kT . Within the lifetime of the metastable membrane, the upper limit of the pore state a^* is defined by the minimum of the $P_{a,a_0}(t = \infty)$ function.

In Fig. 2b the quasi-stationary pore state distributions are shown at different transmembrane voltages. The limit state of the membrane, a^* , decreases with increasing transmembrane voltage (see the beginning of the dashed lines in Fig. 2b). When a^* is close to zero, i.e., $\Delta \bar{G}(r_c) \approx kT$, the metastable state of the membrane ceases to exist. The transmembrane voltage at which the metastable state of the membrane disappears is U_{cr}^{mu} . Using Eqs.11,15 and 16 for the voltage-dependent limit state a^* , the average pore state $\langle a \rangle$ and the deviation of the pore state from the average are determined within the voltage range $0 < U < U_{cr}^{mu}$; see solid line and broken line in Fig.3c.

1.1.3.2.1. Mechanical Breakdown, Reversible and Irreversible Electroporation

The average pore size is essentially zero while the membrane is in its metastable phase. Because of the thermal fluctuations, pores are opening temporarily, but their state exceeds $a=1$ very rarely (see Fig. 3c). In spite of this, there is a finite probability, $P_{a^*,a_0}(t = \infty)$ that the state of the pore exceeds the limit state $a^*(U)$. As a consequence of this, the membrane becomes unstable and pore opening proceeds until the mechanical rupture of the membrane (*mechanical breakdown*) takes place. Since $P_{a^*,a_0}(t = \infty)$ increases with increasing transmembrane voltage, the probability of the mechanical breakdown increases or the *lifetime* of the metastable membrane decreases.

Applying supercritical transmembrane voltage ($U > U_{cr}^{mu}$), the membrane becomes unstable immediately and coherent unlimited opening of the micropores takes place. This results in rupture of the membrane (*irreversible electroporation*). If, however, the voltage is switched off before none of the pore states have attained the limit state $a^*(U = 0V)$, the membrane jumps back into the metastable state and resealing of the pores takes place. This is the mechanism of *reversible electroporation* in the case of metastable membranes. In the voltage interval $U_{cr}^{mu} < U < U_{cr}^{us}$ there is neither a stationary nor a quasi-stationary solution of Eq.11 and therefore the membrane is unstable. Strong electric fields ($U > U_{cr}^{us}$) stabilize the membrane. Qualitatively, this is equivalent to the porous phase of stable membranes (see Sec. 1.1.3.1). According to the calculations for oxidized cholesterol membranes, $U_{cr}^{us} \cong 1.2V$. At $U > U_{cr}^{us}$ the most probable pore state decreases with increasing transmembrane voltage, while it levels off after 1.7V at $a \cong 1000$ (not shown in Fig. 3c). Since these states are larger than $a^*(U = 0V)$, if the field is switched off, the membrane becomes unstable and ruptures.

The phenomena of mechanical breakdown and electroporation (reversible and irreversible) have been demonstrated on oxidized cholesterol membranes^{6,12}. It is interesting to mention that bilayers made from phosphatidylcholine, phosphatidylethanolamine, and monoolein were fragile and always ruptured after the application of the supercritical field¹². In spite of this, the voltage relaxation curves of these membranes just after the application of charge pulses of $400\mu\text{sec}$ duration were similar to those of the oxidized cholesterol membranes. This is presumably because the threshold pore state of conductivity, a_{th} (where the pore size is equal with the size of the hydrated ions), and the threshold pore state of metastability $a^*(U = 0V)$, are comparable for the fragile membranes while $a^*(U = 0V) > a_{th}$ in the case of oxidized cholesterol membranes. Therefore, when a fragile membrane has attained its highly conducting state, some of its pores have exceeded $a^*(U = 0V)$, too. After switching off the field the majority of the pores start annealing. This leads to a characteristic voltage relaxation. The largest pores continue opening until rupture of the membrane.

1.1.3.3. Nonstationary Solutions

If the pore state at $t = 0$ is a_0 , the function $F_{a,a_0}^{(1)}(t)dt$ is the probability that the pore reaches state a for the first time within the time interval t and $t+dt$. The first passage time is the average time of the $a_0 \rightarrow a$ process:

$$T_{a,a_0}^{(1)} = \int_0^{\infty} t F_{a,a_0}^{(1)}(t) dt \quad (17)$$

where $F_{a,a_0}^{(1)}(t)$ is related to $P_{a,a_0}(t)$ through the relation⁷:

$$P_{n,a_0}(t) = \int_0^t F_{a,a_0}^{(1)}(t-\tau) P_{n,a}(\tau) d\tau \quad (18)$$

The first passage time is an exact function of the transition probabilities in Eq.10. The form of the function depends on the actual restrictions of the stochastic process. The stochastic variable of the electroporation a is restricted; it is never a negative value. The lowest permitted state, $a = 0$, is called the reflecting state of the process.

In the case of metastable membranes, the upper limit state, a^* , is called the *adsorbing state* of the process. After reaching this state, rupture of the membrane takes place and the stochastic variable never returns to the $(0, a^*)$ interval.

In Table 1, expressions for first passage time are shown in the case of different restrictions on the stochastic process. Using these exact formulas, we can calculate: the time delay of mechanical breakdown; reversible and irreversible electroporation; and the time course of the coherent pore opening and closing process, when stepwise change of the transmembrane voltage takes place.

1.1.3.3.1. Time Delay of Mechanical Breakdown – Membrane Lifetime

In the case of metastable membrane, sooner or later the system becomes unstable. This takes place when one of the pores exceeds the limit state of metastability. Considering only a *single pore*, one can determine the first passage time from the closed pore state ($a_0 = 0$) to the limit state (a^*) by means of Eq.12. The obtained first passage time, $T_{a^*,0}^{(1)}$ as a function of transmembrane voltage ($0 < U < U_{cr}^{mu}$) is shown in Fig. 4. If the average number of pores in the membrane is larger than one, the membrane lifetime is shorter. An approximate relationship between the membrane lifetime $T_{a^*,0}^{(N)}$ and the average number of the pores N has been derived by Arakelyan et al.¹⁵ in the case of large number of pores:

$$T_{a^*,0}^{(N)} \cong T_{a^*,0}^{(1)} N^{-1/2} \quad (19)$$

Thus apart from a constant term, semilogarithmic plots of $T_{a^*,0}^{(1)}(U)$ and $T_{a^*,0}^{(N)}(U)$ functions are the same. In accordance with the experimental lifetime data (Abidor et al.⁶ and Green and Andersen, personal communication), the logarithmic plot of $T_{a^*,0}^{(1)}(U)$ is a straight line within the 0.1-0.2V interval and then the curve starts to level off.

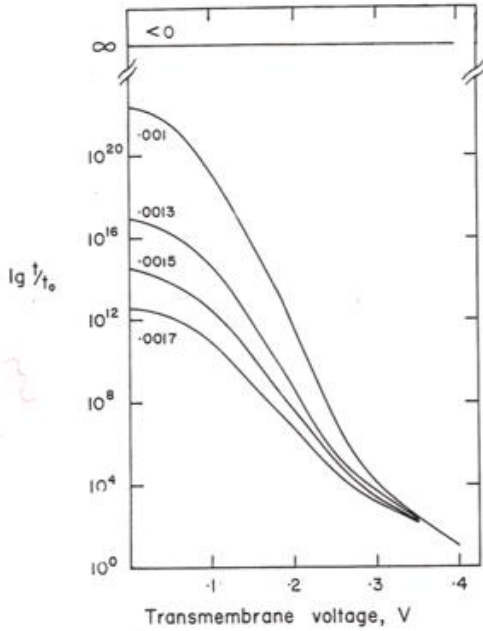


Figure 4. Lifetime of planar metastable membranes as a function of transmembrane voltage at different values of $\Delta g (= \Delta\mu / A_0)$ shown at each curve in N/m. $t = T_{a^*,0}^{(1)}$ and $t_0 = (\beta^2 / \tau) e^{-\alpha/kT}$ (τ , α and β are defined by Eqs.2,4).

According to the calculations, the membrane lifetime is very sensitive to Δg especially at zero electric field (Fig. 4). Since $\Delta g = \Delta\mu / A_0$ is strongly related to the lipid concentration in the aqueous solution (Sec. 1.1.2.5), reliable lifetime data cannot be obtained without a controlled lipid concentration in the aqueous medium.

1.1.3.3.2. Time Delay of Electroporation

After applying a supercritical voltage $U > U_{cr}^{mu}$, a more or less coherent opening of the pores takes place. When the average pore size a becomes comparable to the size of the hydrated ions in the aqueous medium a_{th} , the electric conductivity of the membrane increases by about 10 orders of magnitude¹². The *delay time* between the application of the electric field and the increase of the membrane conductivity has been estimated by determining $T_{a_{th},0}^{(1)}$ {Eq.12} at different transmembrane voltages [Fig. 5a and Fig. 5b at ($U_{cr}^s < U < 1V$) and ($U_{cr}^{mu} < U < 1V$) interval, respectively].

The calculated $T_{3,0}^{(1)}$ is the upper limit of the delay time because for example, pores with $a_0 = 1$ reach $a_{th} = 3$ much faster than pores with $a_0 = 0$. In the case of Fig.5b, the vertical line at U_{cr}^{mu} separates the metastable and unstable nonconducting states of the membrane, while in Fig. 5a the vertical line at U_{cr}^s separates the poreless and porous conducting states of the stable membrane.

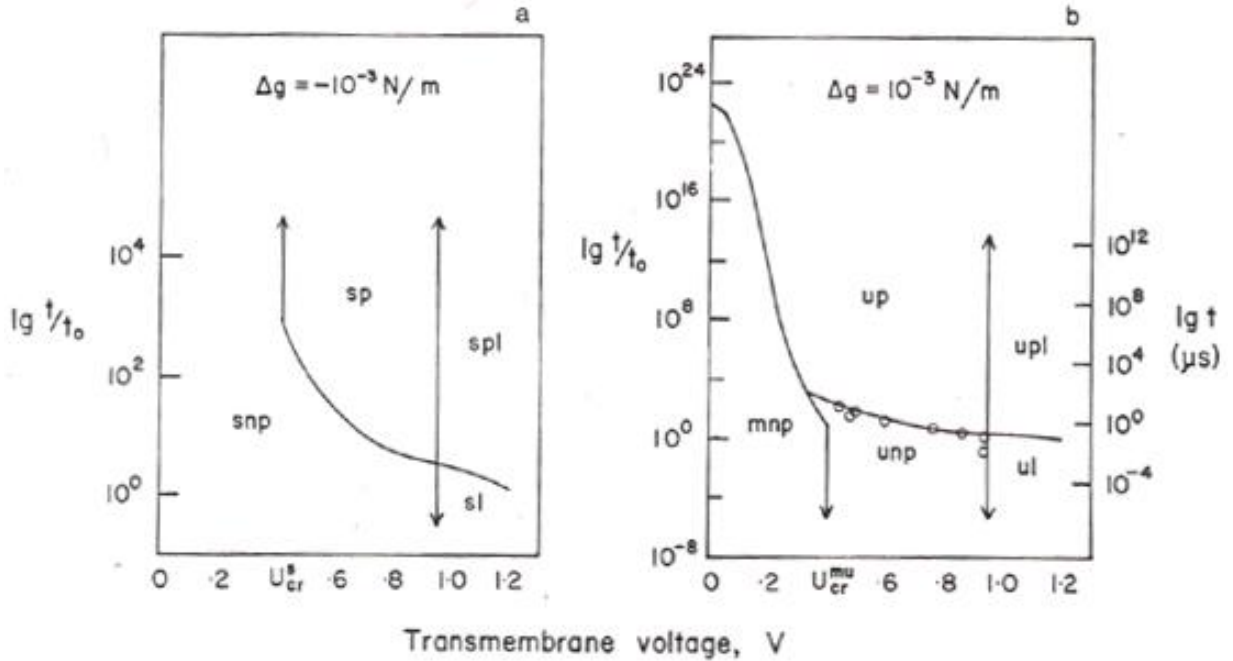


Figure 5. Time delay of electroporation as a function of transmembrane voltage.

a) Stable membrane; b) metastable membrane. Circles: experimental data from Benz and Zimmermann¹⁶, right side ordinate. m, metastable membrane; u, unstable membrane; s, stable membrane; np, non-conductive (small) pores; p, conductive pores; l, conductive lipid membrane. The threshold pore state of the conductive pores is $a_{th} = 3$ (Benz and Zimmermann¹⁷), $t = T_{3,0}^{(1)}$ and $t_0 = (\beta^2 / \tau) e^{-\alpha/kT}$ (τ , α and β are defined by Eqs.2,4). In the transmembrane voltage interval $(0V, U_{cr}^{mu})$ the membrane lifetime is plotted; in this interval $t = T_{a^*,0}^{(1)}$.

At a subcritical field, the metastable membrane becomes conductive after a very long delay time and then the mechanical breakdown takes place [Fig. 5b, solid line in $(0V, U_{cr}^{mu})$ interval]. In the case of *metastable membranes*, the measured and calculated delay time data of oxidized cholesterol membranes are in good agreement if t_0 is properly chosen (see circles in Fig.5b). In spite of the encouraging agreement, it is important to note that the calculations assume a stepwise change of the transmembrane voltage and this is not the case in the experiments of Benz and Zimmermann¹⁶. Powell et al.⁴ developed a model of the electroporation which simulates the conditions of these experiments properly. The experimental data show a drastic change in the tendency of the delay time-voltage curve at 0.95V. According to Benz and Zimmermann¹⁶, at this voltage not only the aqueous membrane pores but also the bulk lipid part of the membrane becomes conductive. At this transmembrane voltage, the electric field energy becomes comparable with the Born energy of the ion in the membrane.

1.1.3.4. Transition Kinetics

Up to this point, the first passage time was calculated as a function of transmembrane voltage at given starting and final state. Let us now determine the first passage time as a function of the final state both at a given starting state and at a given transmembrane voltage. Physically, this function is analogous to the time dependence of the average pore state, $\langle a(t) \rangle$.

Here we use the advantage that the exact form of the first passage time is known (Table 1) while in the case of the $\langle a(t) \rangle$ function only approximate solutions are available³.

1.1.3.4.1. Poreless \rightleftharpoons Porous Transition

In the case of *stable membranes*, a poreless \rightarrow porous transition can be induced by supercritical fields. The starting state is $a_0 = 0$ and the most probable stationary porous state (Fig. 3a) is the final state of the transition process. The first passage time can be determined by Eq.12. In Fig. 6a the kinetics of this transition are shown at different transmembrane voltages.

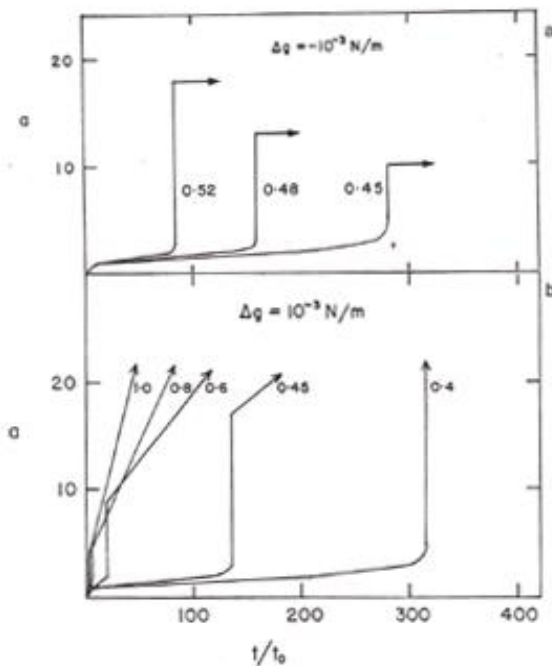


Figure 6. Transition kinetics of electroporation. a) Poreless \rightarrow porous transition in a stable membrane; b) rupture process in an unstable membrane. Transmembrane voltage is shown for each curve in volts. $t = T_{a,0}^{(1)}$ and $t_0 = (\beta^2 / \tau) e^{-\alpha/kT}$ (τ , α and β are defined by Eqs.2,4).

In every case the transition process begins with a small increase in the pore state. During a latency period, the pore state increases very slowly. The higher the transmembrane voltage the shorter is the latency period. Finally, the pore state reaches the stationary value with a very fast process. Upon switching off the field, the porous \rightarrow poreless process takes place. By means of Eq.14 the time course of the resealing process has been calculated in the case of two different starting states. The semilogarithmic plot of the relaxation process is shown in Fig. 7a.

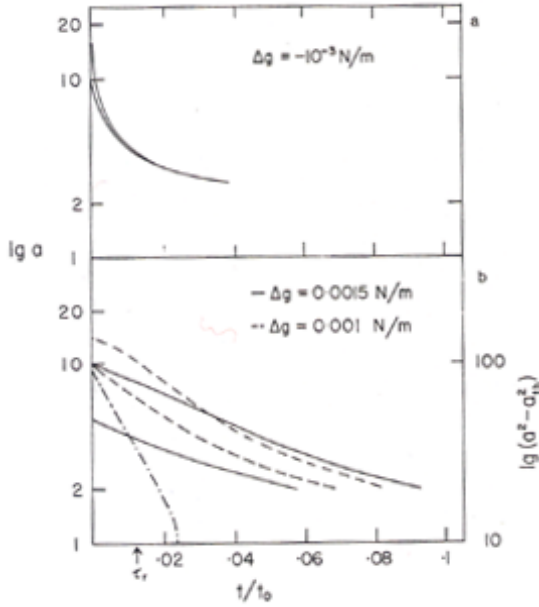


Figure 7. Resealing process. a) Porous \rightarrow poreless transition in stable membrane at different starting states, a_s . Upper curve: transmembrane voltage is 0.5V at $t < 0$ and 0.0V at $t > 0$; lower curve: transmembrane voltage is 0.45V at $t < 0$ and 0.0V at $t > 0$. b) Resealing process of metastable membrane both at different starting states, $a_s < a^*(0)$ and Δg . $t = T_{a_s}^{(1)}$ and $t_0 = (\beta^2 / \tau) e^{-\alpha/kT}$ (τ , α and β are defined by Eqs.2,4). The dot-dash line represents the function $a^2 - a_{th}^2$ with the respective ordinate at the right-hand side; $a_{th} = 3$ (Benz and Zimmermann¹⁷); $\Delta g = 0.001$ N/m, $a_s = 10$ and τ_r is the relaxation time of the annealing process.

1.1.3.5. Membrane Rupture

After applying supercritical field, the *metastable membrane* becomes unstable immediately. The beginning state is $a_0 = 0$. The time course of the process can be determined by Eq.12. In Fig. 6b the rupture process is shown at different transmembrane voltages. The process is similar to the poreless \rightarrow porous transition, but the pore state further increases after the very fast increase in pore state, resulting in the rupture of the membrane.

1.1.3.5.1 Resealing Process

Upon switching off the supercritical field before the limit state of metastability, $a^*(U = 0V)$, has been attained, the membrane becomes metastable again. By means of Eq.13 the time course of the relaxation process, $a(t/t_0)$ has been calculated both at different starting states, a_s and at different Δg values (see Fig. 7b). The dot-dash line is the $a^2(t/t_0) - a_{th}^2$ function in the case of $\Delta g = 0.001$ N/m, $a_s = 10$, $a_{th} = 3$. For $a < a_{th}$, no ions are conducted. The shape of this dot dashed curve is the same as that of the measured conductivity versus time curves during the resealing of oxidized cholesterol membranes¹⁷. Therefore, as is physically plausible, the ion conductance is proportional to $a^2(t/t_0) - a_{th}^2$. Using the relaxation time ($\tau_r = 0.55 \mu\text{sec}$) of the experimental resealing process at 40°C (Benz and Zimmermann¹⁷) and the calculated relaxation curve in Fig. 7b, one can determine the absolute time scale: $t_0 = 0.55 \mu\text{sec} / 0.0125 = 44 \mu\text{sec}$.

1.2. Phenomenological theory of low voltage electroporation

In common electroporators cells can be transfected with foreign genes by applying 150–700V pulse on the cell suspension. Because of Joule heating, the cell survival rate is 10–20% in these electroporators. In a recently developed electroporator, termed the low-voltage electroporator (LVEP), cells are partially embedded into the pores of a micropore filter. In LVEP cells can be transfected by applying 25V or less under normal physiological conditions, at room temperature. The large increase in current density in the filter pores, produced by the reduction of current shunt pathways around each embedded cell, amplifies a thousandfold the local electric field across the filter and results in high enough transmembrane voltage for cell electroporation. The Joule heat generated in the filter pore is fast dissipated toward the bulk solution on each side of the filter, and thus cell survival in the low-voltage electroporator is very high, above 98% while the transfection efficiency for embedded cells is above 90%. In this chapter the phenomenological theory of LVEP is developed. The transmembrane voltage is calculated along the membrane of the cell for three different cell geometries. The cell is either fully, partially or not embedded into the filter pore. By means of the calculated transmembrane voltage the distribution of electropores along the cell membrane is estimated. In agreement with the experimental results cells, partially embedded into the filter pore, can be electroporated by as low as 1.8–3.5V applied voltage. In the case of 25V applied voltage 90% of the cell surface can be electroporated if the cell penetrates further than half of the length of the filter pore.

1.2.1. Introduction

Biological membranes are known to become transiently more permeable by the action of short electric field pulses¹⁻⁴ when the threshold value of the transmembrane voltage, about 0.5–1V, is exceeded. (The transmembrane voltage is defined by the potential difference between the inner and outer surfaces of the cell membrane.) This phenomenon is called electroporation or electropermeabilization and it can be used to transfect cells with foreign genes⁵. Electroporation of biological cells is commonly carried out in a cell suspension using parallel plate capacitor chamber⁶. The field between the plates is essentially homogeneous since the cell density is low. The voltage required for electroporation varies from 150V to 700V across a 0.2cm gap of physiologic solution ($\approx 0.15MNaCl$). The applied voltage depends on factors such as the spacing between the

capacitor plates, the cell type, and solution temperature. The field strengths needed for suspension electroporation normally vary between 750-2000 V/cm. The resulting current produced by these fields in the low resistivity physiologic solution is in the range of 25-100A. Substantial Joule heating, electrode products, and solution electrolysis are byproducts produced by these fields in cell suspension⁷, and thus the cell survival rate is low. For COS-7 cells the survival rate in suspension experiments varies from 10% (Ref.8) to 20% (Ref.9). These survival rates are in agreement with the rates quoted by commercial companies for their systems (Personal communications with BTX Corp., Life Technologies, Inc., and Savant/E-C Apparatus, Inc.)

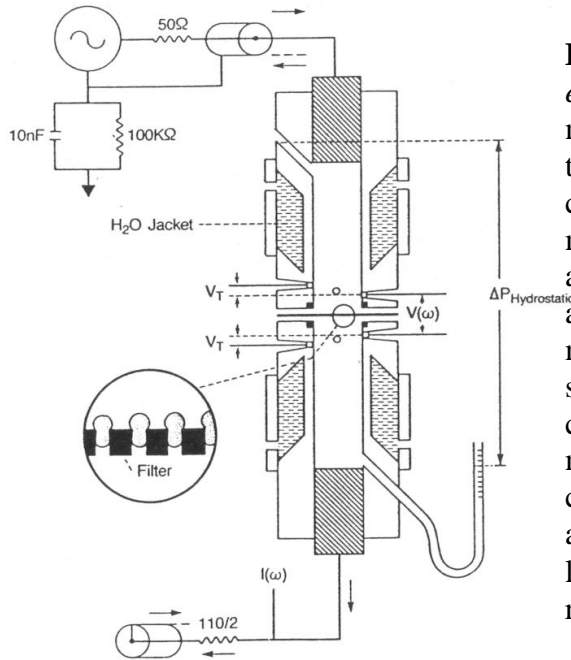


Figure 1. Schematic of low-voltage electroporator (LVEP). Shaded areas mark the cylindrical carbon electrodes at the top and the bottom of the vertical chamber. The chamber is divided by a micropore filter. The plane of the filter aligned perpendicular to the symmetry axis of the cylindrical chamber is marked by a heavy solid line. The inset shows a magnified part of the filter with cells partially embedded into the micropores. Note that in the figure the chamber is stretched along its symmetry axis. In reality the chamber's inner length and diameter is 2 and 1 cm, respectively.

Recently, an alternative to cell suspension electroporation (SEP); the method of low-voltage electroporation (LVEP), was introduced¹⁰⁻¹⁶. The schematic of the low-voltage electroporator (LVEP) is shown in Fig.1 (reproduced from Ref.17). The vertical chamber consists of two mirror image halves. The inside diameter of the cylindrical chamber is 1cm, with cylindrical porous carbon electrodes enclosing the upper and lower ends of the chamber. The carbon electrodes apply the input signal, and are separated by 2cm. This produces a cylindrical measurement volume with dimension of 1cm in diameter and 2cm in length. A polycarbonate NucleporeTM filter (its plane aligned perpendicular to the symmetry axis of the chamber) is sealed into the center of the chamber, and the cells are then embedded into the filter pores (see enlargement in Fig.1) by using a hydrostatic pressure of 25–30mmHg. In LVEP as low as 2–25V applied voltage is sufficient to induce electroporation because 40% of the applied voltage drops in the 13μm long micropores of the filter¹⁷. The average field across the entire chamber for 10V input is less than 5V/cm, while the average field across the filter with cells is about 3000V/cm.

Thus the field in a LVEP is highly inhomogeneous, amplified about 1000 times in conjunction with the increase in current density through the filter pores. However, the current produced in this system is only 25-50mA. The bulk temperature increase caused by a 90ms pulse of 10V is less than $0.003^{\circ}C$ and the local Joule heating generated in the filter pore is dissipated in less than 0.3 ms (Appendix 1). Because of the negligibly small Joule heating the cell survival rate is above 98% (Refs.12,16).

The development of the phenomenological theory of SEP started almost 40 years ago. The transmembrane voltage around a spherical cell placed into a constant, subcritical electric field, $V(\theta)$, was determined by solving the Laplace equation^{18,19}. The field is subcritical as long as the absolute value of the transmembrane voltage is below the critical value, $V_{cr} \approx 0.5-1\text{ V}$. When the field is switched on at time $t = 0$ the steady state transmembrane voltage, $V(\theta)$, is attained after the charging of the membrane. In this case the solution can be separated to the steady state and transient part, $f(t)$, as follows:

$$V(\theta, t) = [V(\theta)][f(t)] = [1.5RE_o \cos(\theta)][1 - e^{-t/\tau}] \quad (1)$$

where R is the radius of the cell, E_o is the field strength far from the cell, θ is the angle (azimuthal angle) between the direction of E_o and the vector directed from the center of the cell to the considered membrane segment, and τ is the membrane's charging time constant. According to Eq.1 the absolute value of $V(\theta)$ is maximal at the poles of the cell, while it is zero at the equator.

In the case of supraccritical fields, when electroporation takes place, however, there is no closed form solution of the Laplace equation. The azimuthal dependence of the transmembrane voltage, $V_{exp}(\theta, t)$ was measured on a spherical sea urchin egg, stained with voltage sensitive fluorescence dye, at different time points after the application of supraccritical electric field²⁰⁻²². These measurements showed that: i) those regions of the cell membrane which would experience supraccritical transmembrane voltage appear to be porated within less than $1\mu\text{s}$, ii) the transmembrane voltage remains symmetric around the z-axis (the axis going through the poles of the egg), although it decreases significantly within a certain range around the pole.

We notice that the transmembrane voltage, $V(\theta, t)$, can be calculated by means of Eq.1 not only at subcritical pulses but also at supraccritical pulses if the cell membrane is assumed to be unporated. In reality pore formation takes place where the absolute value of this calculated transmembrane voltage exceeds the critical voltage, V_{cr} . In the case of supraccritical electric pulses the phenomenological theory of SEP has been developed by Kinoshita and his co-workers. They assumed that the probability of pore formation is directly proportional to $|V(\theta, t) - V_{cr}|$, where $V(\theta, t)$ is defined by Eq.1. Thus, at any time t after the application of the supraccritical pulse, the excess specific conductivity in the porated region of the membrane, $\Delta\sigma_m(\theta, t)$, is:

$$\Delta\sigma_m(\theta,t) = \Delta\sigma_m(\theta_o,t) \frac{|V(\theta,t)| - V_{cr}}{|V(\theta_o,t)| - V_{cr}} = \Delta\sigma_m(\theta_o,t) \frac{|V(\theta)| f(t) - V_{cr}}{|V(\theta_o)| f(t) - V_{cr}} \quad (2)$$

where at $\theta = \theta_o$, $|V(\theta)|$ assumes its global maximum. By using the above function for the excess membrane specific conductivity the Laplace equation was solved numerically by Hibino et al.^{21,22}. The solution was in accordance with the measured transmembrane voltage, $V_{exp}(\theta,t)$. At any given time, t , the excess specific conductivity of the membrane at the pole, $\Delta\sigma_m(0,t)$, was the only adjusted parameter of the theory of SEP. The analysis of the experimental data revealed that $\Delta\sigma_m(0,t)$ gradually increased as long as the electric field was on. After switching off the field the decrease of $\Delta\sigma_m(0,t)$ could be described by two exponentials with time constants $7\mu s$ and $500\mu s$. We note that the above theory is more complicated in the case of an asymmetric electroporation model²².

In this chapter, after defining the geometrical and material parameters of the system in the 1.2.2. Model section the solutions of the Laplace equation are presented in the 1.2.3 Results section for different lengths of cell penetration into the filter pore. In the 1.2.4. Discussion section the calculated electric field is compared with the field around a single spherical cell in cell suspension and the importance of the current density amplification (CDA) is discussed. The distribution of the electropores along the membrane is calculated for different cell geometries. The calculated minimal applied voltage needed to induce electroporation is compared with the available experimental result and the efficiency of electroporation is defined and calculated for different cell geometries.

1.2.2. Model

1.2.2.1. Geometry of the Model of Low-Voltage Electroporator

The LVEP can be modelled by N electrically identical, parallel units, where N is the total number of the filter pores. One unit consists of a filter pore and its surrounding. The pore is cylindrical (pore length is $13\mu m$ and pore radius is $1\mu m$) and its symmetry axis is perpendicular to the surface of the filter. The unit itself is assumed to be a cylinder too, its symmetry axis (z axis) coincides with the symmetry axis of the pore, while its cross sectional area, $254.5\mu m^2/unit$, is equal with the average filter area per filter pore.

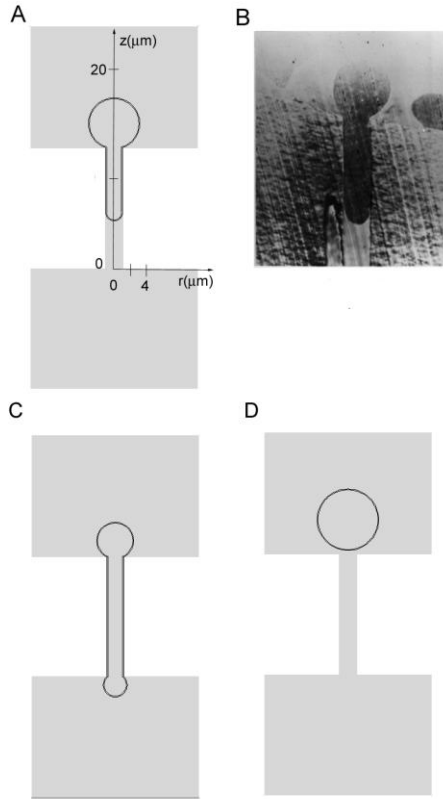


Figure 2. The geometry of a unit of the low voltage electroporator. White area represents the filter, while gray area marks the bulk solution regions on both side of the filter and the filter pore. Solid line shows the cell membrane. (A) Cell is partially and (C) fully embedded into the filter pore. (D) Cell is out of the filter pore. (B) Transmission electron micrograph of human erythrocyte in the filter pore; the finger length is about $8\mu m$.

The cross section of a unit along the z axis is shown in Fig.2a. Grey area marks the filter pore and the bulk regions on both side of the filter, while white areas represent the filter around the pore. Solid line show the cell membrane. The vertical, z axis is the symmetry axis of the unit, while the horizontal axis measures the radial distance, r , from the symmetry axis. The unit contains one cell of surface area $137.3\mu m^2$, which is the average surface area of an erythrocyte²³. In Fig.2a,c and d the cell is partially embedded, fully embedded into the filter pore, and outside the pore, respectively. In each case the center or symmetry axis of the cell coincides with the z axis of the unit. Outside the filter pore the cell is assumed to be spherical (Fig.2d). The geometry and location of the cell can be given by its radius ($r_2 = 3.305\mu m$) and the coordinate of its center, z_2 . When the cell is fully embedded into the filter pore its geometry is assumed to be two truncated spheres connected with a cylindrical tube (Fig.2c). In this case the geometry and location of the cell can be described by the center and radius of the lower truncated sphere (z_1 and r_1), the outer radius of the tube ($r_t = 0.9\mu m$) and the center and radius of the upper truncated sphere (z_2 and r_2). In the case of partially embedded cells the same parameters define the location and geometry of the cell with the restriction that one of the truncated spheres is a hemisphere (at the tip of the finger) of radius r_t . The part of the cell which is penetrated into the filter pore is called the finger of the cell. The geometry of the cell partially and fully embedded into the filter pore has been confirmed by direct observation^{10,14,17}. Fig.2b

shows the transmission electron micrograph of a human erythrocyte partially embedded in a filter pore. When physiologic solution is in the extracellular space the finger length of the embedded erythrocyte cell is about $8\mu m$ (Fig.2b). The flaccidity of the cell and thus the finger length can be modified by changing the salt concentration of the extracellular space.

The geometry of the model system agrees almost completely with the geometry of the LVEP. There are only three aspects in the geometry of the model which differ from the experimental geometry: 1) the membrane thickness of the cell in the model is $0.1\mu m$, while in reality the thickness of the cell membrane is about $0.01\mu m$ (Ref.23); 2) the thickness of the narrow passage between the finger surface and the filter pore wall is $0.1\mu m$, while in reality it is estimated to be $0.01\mu m$ (see Appendix 2 and Ref.17); 3) the thickness of the bulk region on each side of the filter is $13\mu m$ while in reality it is 1 cm . In the case of this model geometry we are able to obtain reliable numerical solutions of the partial differential equation of the electric potential. The effect of the deviations 1) and 2) on the transmembrane voltage is negligibly small (see Appendix 3), while deviation 3) can be easily corrected. It was shown by Schmukler¹⁷ that 40% of the applied voltage drops in the filter. Thus in our model calculations the voltage, applied very close to the filter surfaces, represents 40% of the voltage applied to the capacitor plates of the LVEP chamber. For example if 10V is applied to the LVEP unit the corresponding voltage applied to the LVEP chamber is 25V.

1.2.2.2. Laplace Equation of The Model of Low-Voltage Electroporator

In this section the partial differential equation of the electric potential of a unit of the LVEP is described.

1.2.2.2.1. Boundary Conditions

In every calculation the potential applied at $z = 26\mu m$, the top of the cylindrical unit, is $u(r,26) = 10V$, while the applied potential at $z = -13\mu m$, the bottom of the cylindrical unit, is $u(r,-13) = 0V$.

A Neumann type boundary condition was utilized at every other boundary (the wall of the filter pore, the top and bottom surfaces of the filter, the borders to the neighbor units and the symmetry axis of the unit) because the normal component of the current to each of these boundaries is zero:

$$-\mathbf{n} \cdot (\sigma_f r \nabla u) = \mathbf{n} \cdot \mathbf{j} = 0 \quad (3)$$

where \mathbf{n} is the normal vector to the surface of the boundary, r is the radial distance from the symmetry axis (z-axis), σ_f is the electric conductivity of the extra- and intracellular space, while \mathbf{j} is the current density.

1.2.2.2.2 Laplace Equation in Inhomogeneous Medium

The steady state electric potential in an axially symmetric unit of the LVEP can be determined by solving the following Laplace equation:

$$\frac{\partial}{\partial r} \left(\sigma r \frac{\partial u}{\partial r} \right) + \frac{\partial}{\partial z} \left(\sigma r \frac{\partial u}{\partial z} \right) = 0. \quad (4)$$

1.2.2.2.3 The Matching Conditions

The electric conductivity, $\sigma = \sigma(r, z)$ is piecewise continuous and is discontinuous on the outer and inner surfaces of the cell membrane. In our calculations the same conductivity, σ_f , is taken in the extra- and intracellular regions, while the conductivity of the cell membrane is σ_m . The conductivity ratio of the extra- or intracellular space (0.15M NaCl) to the human erythrocyte membrane at 25 °C is $\sigma_f/\sigma_m = 2.3 \cdot 10^4$ (Ref.23) while the conductivity of the filter is assumed to be zero. The matching conditions on the membrane surface of normal vector \mathbf{n} are

$$u_f = u_m \quad (5)$$

$$\sigma_f \frac{\partial u_f}{\partial n} = \sigma_m \frac{\partial u_m}{\partial n} \quad (6)$$

1.2.2.2.4 Numerical Solution of The Laplace Equation

The numerical solution of the Laplace equation is obtained by using the PDE toolbox of the Matlab program (The Math Works, Inc.). This program package is capable of calculating the electric potential u at every (r, z) point of our model system, i.e. to solve a 3D Laplace equation when the system possesses axial symmetry. The program uses the finite element method to solve PDE's. It approximates the two-dimensional, (r, z) , computational domain with a union of triangles. The triangles form a mesh. The triangular mesh is automatically generated and can be further refined. Before solving the PDE, in order to get fine meshes everywhere in the membrane, the original mesh is refined twice. In solving the Laplace equation the default parameters of the program are utilized.

1.2.3. Results

The electric field in a unit of the LVEP was calculated in the case of different cell positions. The cell position is characterized by z_{min} the z -coordinate of the bottom of the cell. Table 1. lists the geometrical parameters of the cell at each calculated cell position.

TABLE 1. Geometrical Parameters of the Cell at Different Cell Positions^a.

z_{min}	z_1^b	r_1^b	z_2^c	r_2^c	cell position
(μm)					
14.822	-	-	18.127	3.305	outside
14.322	-	-	17.627	3.305	outside
13.822	-	-	17.127	3.305	outside
13.322	-	-	16.627	3.305	outside
12.822	-	-	16.127	3.305	outside
11.1	12	0.9	16.03	3.2092	partially embedded
10.1	11	0.9	15.96	3.1382	partially embedded
9.1	10	0.9	15.89	3.0657	partially embedded
8.1	9	0.9	15.81	2.9916	partially embedded
7.1	8	0.9	15.73	2.9153	partially embedded
6.1	7	0.9	15.65	2.8372	partially embedded
5.1	6	0.9	15.57	2.7566	partially embedded
4.1	5	0.9	15.48	2.6738	partially embedded
3.1	4	0.9	15.40	2.5886	partially embedded
2.1	3	0.9	15.29	2.5002	partially embedded
1.1	2	0.9	15.20	2.4085	partially embedded
0.1	1	0.9	15.10	2.3133	partially embedded
-0.9	0	0.9	15.00	2.2141	partially embedded
-1.20371	-0.26	0.94371	14.884	2.18457	fully embedded
-1.51733	-0.48	1.03733	14.819	2.13315	fully embedded
-1.83513	-0.68	1.15513	14.763	2.06523	fully embedded
-2.14626	-0.86	1.28626	14.673	1.98595	fully embedded
-2.46576	-1.04	1.42576	14.563	1.88683	fully embedded
-2.79084	-1.22	1.57084	14.417	1.76784	fully embedded

^aThe surface area of the cell $S = 137.3\mu m^2$ is related to the above parameters as follows:

$$S = \pi(h_1^2 + r_1^2) + 2r_1\pi[(z_2 + r_2 - h_2) - (z_1 - r_1 + h_1)] + \pi(h_2^2 + r_2^2) \quad (7)$$

where the first and third term is the surface area of the truncated sphere at the bottom and top of the cell, respectively, while the second term is the surface area of the connecting tube of radius

r_i . The height of the i th truncated sphere is: $h_i = r_i + \sqrt{r_i^2 - r_i^2}$,

where $i = 1, 2$. ^b z_1 and r_1 is the center's z coordinate and the radius of the truncated sphere on the bottom of the cell. ^c z_2 and r_2 is the center's z coordinate and the radius of the truncated sphere on the top of the cell.

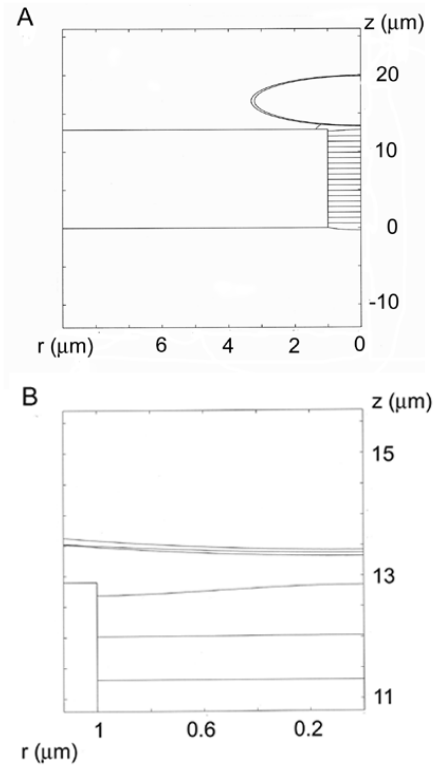


Figure 3. *Calculated electric potential when the cell is out of the filter.* The contour lines are 0.5V apart from each other. The cell position is $z_{min} = 13.322$. (A) Solution for the entire unit. (B) Solution at the bottom of the cell. The voltage applied to the capacitor plates of the LVEP chamber is $V_{app} = 25V$.

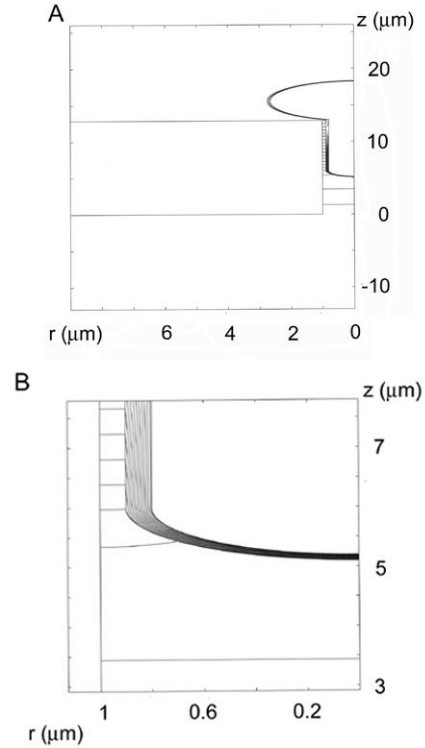


Figure 4. *Calculated electric potential when the cell is partially embedded into the filter pore.* The contour lines are 0.5V apart from each other. The cell position is $z_{min} = 5.1$. (A) Solution for the entire unit. (B) Solution at the bottom of the cell. The voltage applied to the capacitor plates of the LVEP chamber is $V_{app} = 25V$.

In Figs.3,4 and 5, the contour plots of the calculated potential u are shown at three different cell positions. Because of the LVEP unit's axial symmetry the calculated potential is symmetric too. Thus in Figs.3,4 and 5 it is sufficient to show only half of the LVEP unit. In the figures the consecutive contour lines are 0.5V apart from each other. In order to make the contour lines more visible in the membrane and in the narrow passage

the figures are stretched in the direction of the horizontal axis, and thus the shape of the cell is distorted too. These plots show that the strongest electric field in the cell membrane is at $r=0$ and $z=z_{min}$, i.e.: at the bottom of the cell. Note, that there is another local maximum of the density of the contour lines in the membrane at the top of the cell, i.e.: at $r=0$ and $z=z_{max}$, however the respective electric field strength is lower than the field at the bottom of the cell membrane.

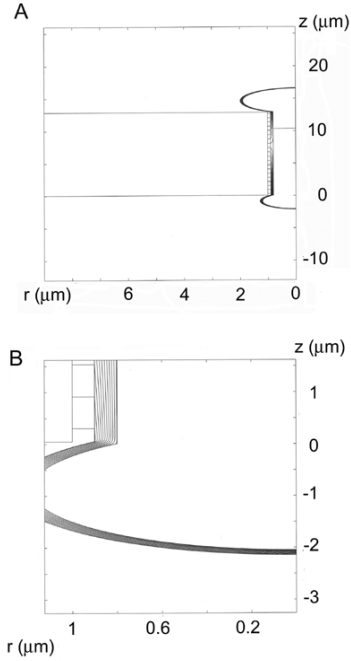


Figure 5. *Calculated electric potential when the cell is fully embedded into the filter pore. The contour lines are 0.5V apart from each other. The cell position is $z_{min} = -2.14626$. (A) Solution for the entire unit. (B) Solution at the bottom of the cell. The voltage applied to the capacitor plates of the LVEP chamber is $V_{app} = 25V$.*

The transmembrane voltage (the potential at the inner membrane surface minus at the outer membrane surface) has been calculated along the cell membrane. In Figs.6a,b and c the transmembrane voltage, $V(z)$ is plotted against the z coordinate of the membrane segment for cases when the cell is out of the filter, partially and totally embedded into the filter pore, respectively.

1.2.4. Discussion

1.2.4.1 Transmembrane Voltage

Figs.6a,b and c show that at every considered cell position, the transmembrane potential is maximal at z_{min} , the bottom of the cell. If the cell is fully embedded into the pore the transmembrane voltage is essentially constant along the cell membrane protruding at the bottom of the filter pore. The transmembrane voltage then linearly decreases along the tubular section of cell. The transmembrane voltage changes sign at the point where the

increasing potential along the outer membrane surface becomes equal with the potential inside the cell.

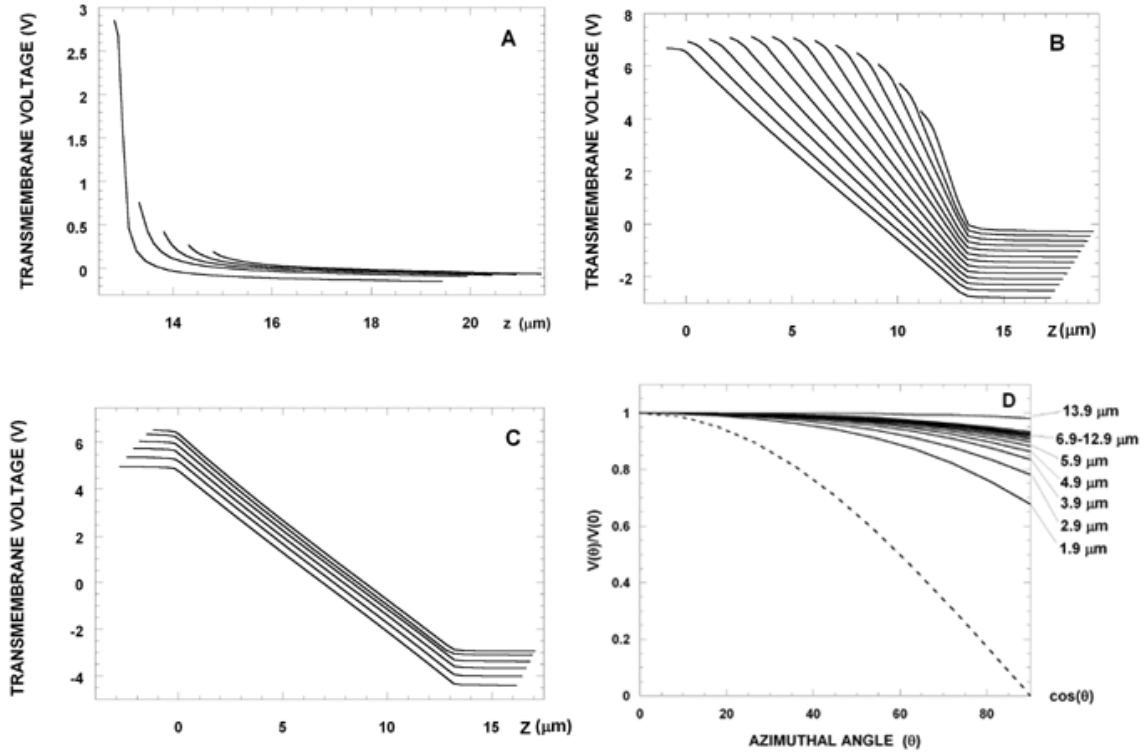


Figure 6. Calculated transmembrane voltage at different cell positions. In (A), (B) and (C) the transmembrane voltage is plotted against the z coordinate of the membrane segment. (A) Cell is out of the filter. The 5 different cell positions are listed in Table 1. (B) Cell is partially embedded into the filter pore. The 13 different cell positions are listed in Table 1. (C) Cell is fully embedded into the filter pore. The 6 different cell positions are listed in Table 1. (D) The angular dependence of the relative transmembrane voltage $V(\theta)/V(0)$ in the half-spherical section of the finger of a partially embedded cell. The solid lines from top to the bottom belong to cells of decreasing finger length (see labels). The 13 different cell positions are listed in Table 1. Dashed line: angular dependence of the relative transmembrane voltage in the case of a spherical cell placed into a homogeneous field (see Eq.1). The voltage applied to the capacitor plates of the LVEP chamber is $V_{app} = 25V$.

The transmembrane voltage stops decreasing and becomes constant along the cell membrane protruding at the top of the filter pore. When the cell is partially embedded into the filter pore the transmembrane voltage changes similarly along the tubular and protruding section of the cell. The change of the transmembrane voltage along the half spherical section of the finger is shown in Fig.6d, where the relative transmembrane voltage, $V(\theta)/V(0)$, is plotted against the azimuthal angle, θ (the angle between the z -axis and the vector directed from the center of the hemisphere to the considered

membrane segment. $\theta = 0$ at the bottom of the cell.). Each curve belongs to different cell positions. When the half spherical section of the finger protrudes at the bottom of the filter pore ($z_{min} = -0.9\mu m$) the relative transmembrane voltage is practically independent of the azimuthal angle (top curve in Fig.6d). However, when the half spherical section is within the filter pore the relative transmembrane voltage decreases with increasing azimuthal angle, and the decrease becomes steeper with decreasing finger length. It is important to mention, however, that none of the angular dependences are as steep as the $\cos(\theta)$ function (dashed line in Fig.6d), which is the angular dependence of the relative transmembrane voltage of a spherical cell placed in a homogeneous electric field and in an electrically homogeneous medium (see Eq.1). The above result suggests that the effective membrane area for electroporation increases with increasing finger length and in the case of long fingers, pores can form practically anywhere in the half-spherical section of the finger if $V(0)$ is larger than the critical transmembrane voltage. In the case of 10V applied voltage, i.e. $V_{app} = 25V$ applied to the capacitor plates of the LVEP chamber, the transmembrane voltage at the bottom of the finger is larger than the critical voltage at every finger length (see Figs.6). For comparison, we note that if there is no filter in our electroporator the same applied voltage results in only $V(0) \approx 1.5V_{app}r_2/L = 6.2mV$ (where $r_2 = 3.3\mu m$ is the radius of the cell and $L = 2cm$ is the spacing between the capacitor plates) transmembrane voltage at the poles of the spherical cell, Eq.1. It is the current density amplification (CDA) in the filter pore that produces about a thousandfold increase of the transmembrane voltage relative to the cell suspension electroporation. CDA estimated by the ratio of the surface area of the filter per pore ($254.5\mu m^2$) and the cross sectional area of a narrow passage ($0.083\mu m^2$, see Appendix 2) is about 3000. Note, that the actual CDA is smaller because part of the electric current flows through the cell membrane (Appendix 3).

The finding that a transmembrane voltage change occurs along the finger of a filter embedded cell seems somewhat counter-intuitive, based on the case of a spherical cell in suspension. The cell membrane of the finger, except for the hemisphere at the end of the finger, is parallel to the direction of the electric field. Our initial assessment, based on angular dependence of the transmembrane voltage along the spherical cell, was that the transmembrane voltage change along the finger length should therefore be zero. However, the finding that the transmembrane voltage changes along the finger can be explained by using concepts from spatial amplification²⁴. The differences in boundary conditions between a cell embedded in a pore, compared to a cell in suspension, explains this finding. Spatial amplification is defined as the amplification of the electric field across the cell membrane for a cell in suspension at low frequencies when the cell membrane becomes non-conductive. Essentially in spatial amplification, the electric field, for the conductive path through the cell, integrates along the length of the cell parallel to the field direction. The conduction path through the cell differs from the external conduction pathway due to the presence of cell membranes at each end of the cell. Whereas, the voltage drop along the cell in the external medium is linear, uniform and very small, the voltage drop through the cell is not uniform. Nearly the entire voltage drop in the conduction pathway through the cell, occurs across the cell membranes at the ends of the cell. This is because in comparison, there is a negligible voltage drop in the intracellular solution of high conductivity or low resistance. The voltage drop in the

external medium is very small, so that the potential external to the membrane is essentially constant. The electric field strength across the cell membranes at either end of the cell is amplified by $\approx (1/2) \cdot (\text{cell length}/\text{membrane thickness})$. Thus, the transmembrane voltage change for a suspended cell is maximal at the two opposite cell ends. In comparison, for a cell embedded in a pore, the boundary conditions are reversed with respect to a cell in suspension. In this case, the voltage drop in the extracellular space along the finger in the pore is also linear and uniform, but in contrast to a suspended cell, this voltage drop is significant and not small. The significant external voltage drop results from the high resistance of the narrow passage around the finger in a pore. In this case, at all frequencies, a substantial voltage drop exists in the external conduction pathway. The conduction pathway through the cell is also different compared to the cell suspensions. For an embedded cell, there is a relatively small voltage drop across the membrane of the cell protruding out of the filter pore. This is because the capacitance of the protruding section is about 10 times larger than the capacitance of the hemisphere at the tip of the finger. A very small voltage drop also occurs inside the cell. This means that the situation is different from the situation for a cell suspension, in that the voltage drop through the cell before the tip of the finger is small, while the voltage drop in the external pathway is large. This difference produces a significant transmembrane voltage change along the finger, that would not occur in cell suspensions. The specialized geometry of a cell embedded in an insulating filter, is such that the transmembrane voltage along a cell membrane perpendicular to the filter surface can change in response to an applied electric field.

1.2.4.2 Distribution of Electropores

Electroporation takes place where the absolute transmembrane voltage of the unporated cell, $|V(z,t)|$ is higher than the critical voltage, V_{cr} . After the charging of the membrane the temporal and spatial distribution of the electropores in the cell membrane can be given by the following expression²⁰⁻²²:

$$p(z,t) = \begin{cases} a(t) \frac{|V(z)| - V_{cr}}{V_{appl}} & \text{if } |V(z)| > V_{cr} \\ 0 & \text{otherwise} \end{cases} \quad (7)$$

where $p(z,t)dz$ is the probability of finding porated region in the membrane segment from z to $z+dz$, and the proportionality factor $a(t)$ gradually increases until the supracritical electric field is on. The spatial distribution of the electropores can be characterized by $p(z,t)/a(t)$. By using the transmembrane voltage curves, $V(z)$, in Figs.6a,b and c the spatial distribution of the electropores has been calculated for three different cell geometries (Fig.7). The electropore density is constant along the protruding sections of the cell membrane and linearly decreases toward the inside of the filter pore (see dashed and dotted lines in Fig.7). The bottom of the non-embedded cell is electroporated but then the electropore density sharply drops to zero (solid line in Fig.7). By using Fig.6d one can also calculate the azimuthal dependence of the pore density in the half spherical section of the cell finger. The pore density is almost constant in the case of long cell fingers,

while for shorter cell fingers the electropore density decreases with increasing azimuthal angle, and the decrease becomes steeper with decreasing finger length.

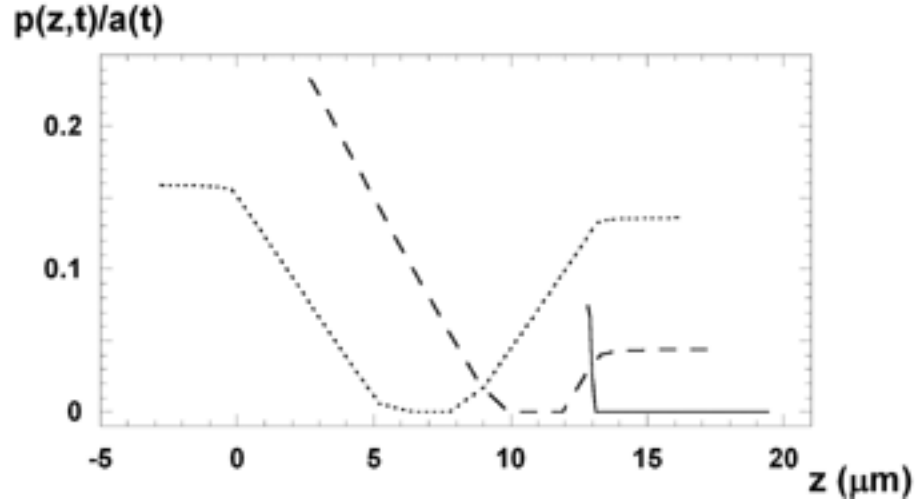


Figure 7. *Distribution of electropores along the cell membrane.* Spatial distribution of electropores, $p(z,t)/a(t)$, is calculated by Eq.7 for three different cell geometries. Solid line: cell is out of the filter pore, $z_{min} = 12.8\mu m$; dashed line: cell is partially embedded into the filter pore, $z_{min} = 2.1\mu m$; dotted line: cell is fully embedded into the filter pore, $z_{min} = -2.79\mu m$. The voltage applied to the capacitor plates of the LVEP chamber is $V_{app} = 25V$. The critical voltage is $V_{cr} = 1V$.

1.2.4.3 Electric Field and Potential

The transmembrane potential and consequently the electric field strength is highest at the bottom of the cell finger. In the case of 25V, applied to the capacitor plates of the chamber, at the bottom of the finger the through membrane electric field strength changes from 4.5 to $7 \cdot 10^5$ V/cm, while the finger length increases from 2 to $10\mu m$. The more embedded the cell is into the filter pore, the lower the potential within the cell. The potential is constant within the protruding section(s) of the cell, while it slightly changes within the finger of the cell (Fig.8).

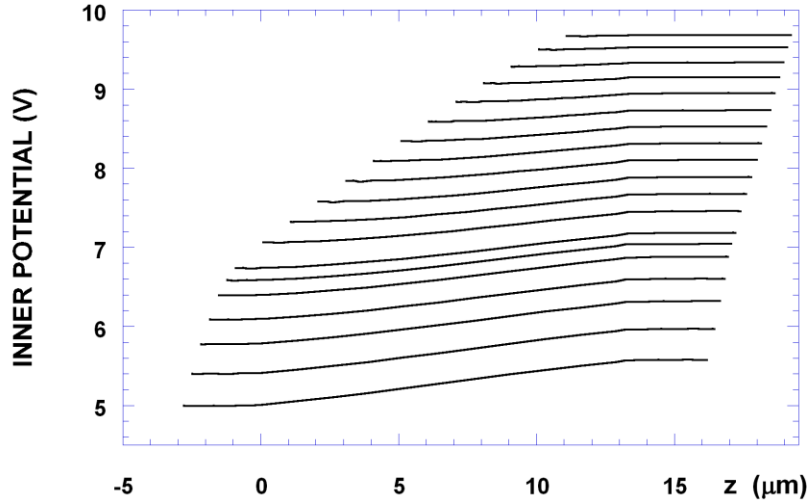


Figure 8. The potential at the inner surface of the membrane is plotted against the z coordinate of the membrane segment. The curves belong to 6 fully and 13 partially embedded cell positions listed in Table 1. The z coordinate of the leftmost point of each curve is z_{min} , characterizing the cell position. The voltage applied to the capacitor plates of the LVEP chamber is $V_{app} = 25V$.

Thus the field strength is negligible in the protruding section(s) and it is less than $460e_z[V/cm]$ in the finger. Because of the CDA the strongest current density of the LVEP can be found in the narrow passage of the filter pore¹⁶, and similarly in the extracellular space the field strength is strongest in the narrow passage because the current density is directly proportional to the field strength (Ohm's law). The field strength in the narrow passage, close to the membrane surface can be estimated by means of the steepest slope of the transmembrane voltage curves in Figs.6b and c (Appendix 3). When the cell is fully embedded into the filter pore the field strength in the narrow passage, at the membrane surface is $7230e_z[V/cm]$. In the case of partially embedded cells the electric field in the narrow passage, at the membrane surface increases with decreasing finger length from $7230e_z[V/cm]$ to $23100e_z[V/cm]$. When the geometry of the LVEP unit approaches the real geometry of LVEP, i.e. the thickness of the membrane and narrow passage are simultaneously decreased, the relative increase of the electric field strength is significant only inside the cell finger (see Appendix 3). The current density is proportional to the field strength (Ohm's Law) and the Joule heating is proportional to the square of the current density. Thus the Joule heating during the pulse is highest at the narrow passage, and negligible in the bulk regions. According to the calculations (Appendix 1) after three pulses each of amplitude 10V and duration 30ms, the Joule heat accumulated in the narrow passage, dissipates fast, within 0.3ms, toward the bulk regions without causing permanent cell damage. Our experimental results show that after applying the above characterized three pulses less than 2% of the cells die. For comparison we mention that in SEP during electroporation the Joule heating takes place everywhere in the extracellular space and thus the heat dissipation after the pulse is very

slow. The heat transfer through the slowly resealing electropores warms up the intracellular space causing eventually permanent cell damage. This explains that in LVEP cells survive even 20 kV/cm local electric field strength, while in SEP 3000V/cm, with pulse duration in the millisecond range, is the upper limit of cell survival⁷.

1.2.4.4 Minimal Applied Voltage

Since the transmembrane voltage is directly proportional to the applied voltage, one can calculate (from the data in Figs.6) the applied voltage needed to get 0.5-1V transmembrane voltage at the bottom of the cell. This is the minimal applied voltage needed to electroporate the cell at least at the bottom of the cell. Fig.9 shows the minimal voltage, applied on the capacitor plates of the LVEP chamber, as a function of the cell position, z_{min} . Open circle and open square marks minimal applied voltage calculated at 0.5V and 1V critical voltage, respectively. The observed minimal applied voltage for human erythrocyte, marked by X in Fig.9, is within the range of the calculated values. In Fig.9 cell positions between the two vertical dash-dotted lines refer to cells partially embedded into the filter pore. The calculated minimal applied voltage increases steeply with increasing cell-to-filter distance. This theoretical result is similar to the experimental data of Yang et al.⁹. They reported a procedure for in situ electroporation of cells grown on microporous membranes of polyethylene terephthalate or polyester (but not pushed into the filter pores) and induced electroporation from as low as 70V applied voltage. It is important to note that if there is no filter in our LVEP the minimal applied voltage is 4030V !

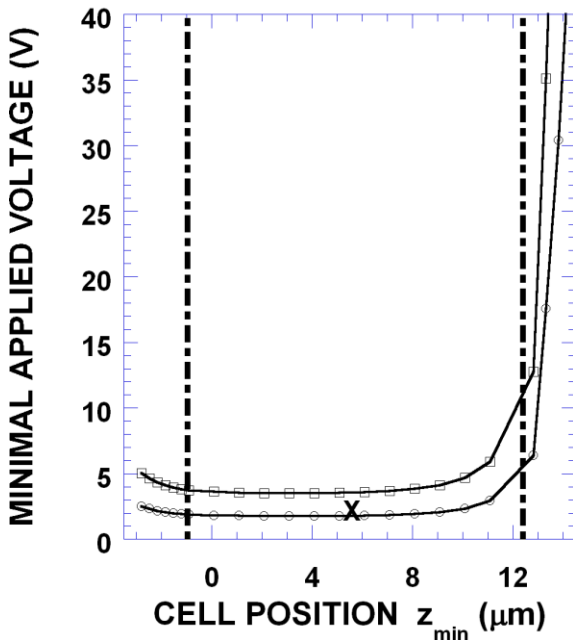


Figure 9. Minimal applied voltage of electroporation. Solid line: calculated minimal applied voltage vs. cell position. z_{min} values between the vertical dash-dotted lines refer to positions of the cell embedded partially into the filter pore. Open circle and open square marks minimal applied voltage calculated at 0.5V and 1V critical voltage of electroporation, respectively. The minimal applied voltage observed in LVEP for human erythrocyte is marked by X.

1.2.4.5. Efficiency of Electroporation

Finally, we point out that the efficiency of electroporation is much higher for fully and partially embedded cells than for cells out of the filter. The efficiency of the electroporation can be characterized by the proportion of the surface of the cell membrane where the transmembrane voltage exceeds the critical value, V_{cr} . By using Figs.6 one can get the z coordinates of the membrane segments (for a given cell position), where the transmembrane voltage is above the critical voltage. Then one can calculate the surface area of the cell membrane belonging to these z coordinates. The efficiency of the electroporation is this area to the total surface area of the cell. In Fig.10 the calculated efficiency of the electroporation is plotted against the cell position. The curves are calculated at different applied voltages. The efficiency of the electroporation is high, 70–98%, when the transmembrane voltage is above the critical value at both the bottom and the top of the cell. With decreasing finger length (i.e. with increasing z_{min}) the transmembrane voltage decreases at the top of the cell, and when it becomes less than the critical voltage the efficiency of the electroporation drops considerably. Then the efficiency decreases linearly with decreasing finger length until zero efficiency is attained. At a given cell position, the higher the applied voltage the higher the efficiency, and at higher applied voltage the drop of the efficiency takes place at shorter finger length.

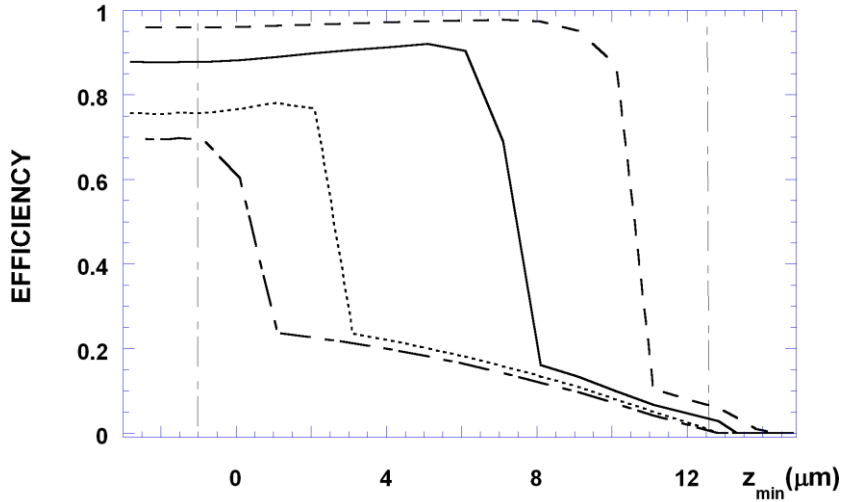


Figure 10. *The efficiency of electroporation.* The efficiency of the electroporation (i.e. the proportion of the membrane surface area where the critical transmembrane voltage, $V_{cr} = 1V$, is exceeded) is plotted against z_{min} . The curves belong to the following voltages applied to the capacitor plates of the LVEP chamber: 10V (dash-dotted line), 12.5V (dotted line), 25V (solid line), 75V (dashed line). z_{min} values between the vertical dash-dotted lines refer to positions of the cell embedded partially into the filter pore. The total surface area of the erythrocyte cell is $137.3\mu m^2$.

1.2.5. Conclusions

In a LVEP, cells are embedded into the pores of a micropore filter. The narrow conductive passages in the filter pores result in a highly inhomogeneous electric field in the electroporator. At as low as 2V applied voltage the field strength becomes 1000–4000V/cm in each micropore and the transmembrane voltage exceeds the critical voltage of cell electroporation at the tip of the finger, i.e. at the bottom of the cell penetrating into the filter pore. The LVEP is ideal for cell transfection with foreign genes. The Joule heat accumulated mainly in the filter pores fast dissipates toward the bulk solutions of the LVEP chamber before the interior of the embedded cells would warm up. Thus the cell survival rate is very high, above 98%. At 25V, applied to the capacitor plates of the LVEP chamber, the transmembrane voltage is higher than the critical value at 87–90% of the cell surface if the cell penetrates further than half length of the filter pore. Since a large percentage of the cell surface can be electroporated the observed transfection efficiency for the embedded cells is higher than 90%.

1.2.6. Appendix 1

Joule Heating in LVEP

Local Joule heating is directly proportional to the square of the electric current density. Joule heating in the LVEP chamber, overall or localized in the filter pores, is minimal. One of the major differences between SEP and LVEP is that the suspension chamber is a one compartment system while the LVEP chamber is a three compartment system. In a suspension the entire volume is heated since most of the current flows through the bulk solution. Comparatively, in LVEP the overall heating is small. However, in the cell embedded filter pore the current density is so high it may cause considerable local heating.

The three compartments in the LVEP chamber are: (1) the bulk solution above the filter, (2) the filter with embedded cells, and (3) the bulk solution below the filter. The temperature increase resulted in by a 90 ms (= 3x 30 ms), 10 V pulse in the bulk compartments can be easily estimated. While calculating the upper limit for the temperature change in compartments 1+3 it is assumed that the total electric power (P_C) flowing into the LVEP chamber is entirely dissipated into compartments 1 and 3:

$$P_C = I^2 R_C = 0.2365[\text{watt}] \quad (8)$$

where,

$$I = 10[\text{V}] / 365[\Omega] = 0.0274[\text{A}] \quad (9)$$

R_C , the resistance of the chamber when the cell membranes are fully charged, is:

$$R_C = 365 - 50 = 315[\Omega] \quad (10)$$

where the total load on the generator is 365[Ω] with the output impedance of the generator of 50[Ω]. Compartments 1 and 3 have a resistance of 85[Ω] each and the cell embedded filter has a resistance of 149[Ω], adding up to 315[Ω] total chamber resistance. The upper limit of the heat, Q , transmitted to the LVEP chamber by the three 10[V] pulses of 90[ms] total duration is:

$$Q = 0.2365[\text{watt}] \cdot 0.09[\text{s}] = 0.0213[\text{J}] \cdot 0.239[\text{cal} / \text{J}] = 0.0051[\text{cal}] \quad (11)$$

The total volume of compartments 1 and 3 is 1.57 [cm³], and the upper limit of the temperature increase of compartments 1+3 is:

$$\Delta T = \frac{Q}{mc} = \frac{0.0051[\text{cal}]}{1.57[\text{g}] \cdot 1 \frac{[\text{cal}]}{[\text{g}][^\circ\text{C}]}} = 0.0032[^\circ\text{C}] \quad (12)$$

where m is the mass and c is the specific heat capacity of the bulk compartments. Thus the temperature change in compartments 1 and 3 is extremely small and they can be considered heat sinks, where temperature remains constant.

If the heat dissipation time for the fluid volume in the filter pore is fast relative to the pulse time, the heat can be dissipated as quickly as it is generated in the pore, thereby preventing any significant local temperature rise or heating in the pore. If all the heat generated in the pore is concentrated in the center of the pore length, a worse case analysis, then the maximum distance to the heat sink on each side of the filter is 6.5 μm. The maximum dissipation time of the heat generated in the filter pore can be calculated by assuming, in the worse case, that all the heat flows in only one direction. From the Onsager equation, the one dimensional heat flux in the center of the filter pore is:

$$c\rho_w \frac{dT(t)}{dt} = -\frac{\kappa}{(\Delta x)^2} [T(t) - T_f] \quad (13)$$

where κ is the thermal conductivity of water, ρ_w is the density of water, c is the specific heat capacity of water, Δx is the distance to the heat sink and T_f is the temperature of the heat sink. This equation also assumes no radial heat loss through the filter, i.e., the filter is a perfect thermal insulator.

The solution of Eq. 13, i.e.: the time dependence of the temperature in the center of the filter pore, is:

$$T(t) = T(0) + [T_f - T(0)][1 - \exp(-\frac{\kappa}{\rho_w c (\Delta x)^2} t)] \quad (14)$$

and thus the time constant of the cooling process is:

$$\tau = \rho_w c (\Delta x)^2 / \kappa = (\Delta x)^2 / \chi \quad (15)$$

where χ is the thermal diffusivity of water. Therefore, the time constant, τ , of the cooling process is:

$$\tau = \frac{(6.5 \cdot 10^{-4})^2 [cm^2]}{1.43 \cdot 10^{-3} [cm^2 / s]} = 0.3 [ms] \quad (16)$$

which is 0.01 times smaller than the single pulse width of 30[ms], so the thermal dissipation rate is 100 times faster than the rate of heat production by a single 30[ms] pulse.

The assumptions made for this calculation are as follows: i) The presence of the embedded cell is ignored. ii) All the heat dissipation is calculated in one direction. iii) The polycarbonate filter is assumed to be a perfect thermal insulator. However, the thermal conductivity of most plastics is $4 - 8 \times 10^{-4} [cal/(s^\circ C cm)]^{25}$ which is 29 - 57 % of the thermal conductivity of water of $14 \times 10^{-4} [cal/(s^\circ C cm)]^{26}$. Thus a considerable amount of heat can flow through the filter. The cross-sectional area of the filter in contact with the heat sinks above and below the filter is about a hundred times greater than the total cross sectional area of all the filter pores. Therefore, given all the simplifying assumptions that were made in calculating the thermal dissipation rate for this system, it is at least two orders of magnitude faster than the dissipation rate predicted by the above calculation.

1.2.7. Appendix 2

Estimation of the thickness of the narrow passage

The total measured resistance of the electrically parallel narrow passages of the filter pores, i.e. the leak resistance R_L is 200[Ω] and the number of micropores in the filter of radius 0.5cm is $N_p = 3.3 \cdot 10^5$ (Ref.17). Thus the average resistance of one narrow passage is: $R_p = R_L \cdot N_p = 6.6 \cdot 10^7 [\Omega]$. The average cross sectional area of a narrow passage is: $A_p = \rho_f L_p / R_p = 0.0753 [\mu m^2]$, where the resistivity of the physiologic solution (0.15MNaCl) is $\rho_f = 7.1 \cdot 10^5 [\Omega \mu m]$ and the average length of a narrow passage is $L_p = 7 [\mu m]$. The thickness of the narrow passage is expected to be: $t_p = r_o - r_i = r_o - \sqrt{r_o^2 - A_p / \pi} = 0.012 [\mu m]$, where r_o ($= 1 [\mu m]$) and r_i are the outer and inner radius of the narrow passage, respectively.

1.2.8. Appendix 3

On the deviations of the model's geometry from the electroporator's geometry

In our model both the membrane and the narrow passage thickness are 10 times larger than the observed values. In order to investigate the effects of these geometrical parameters on the calculated transmembrane voltages we simultaneously decreased the thickness of the membrane and the narrow passage first by 25% and then by 50%. The obtained transmembrane voltage curves, in Fig.11a, do not show significant deviations from the result obtained in the case of the original model geometry (see solid line in Fig.11a).

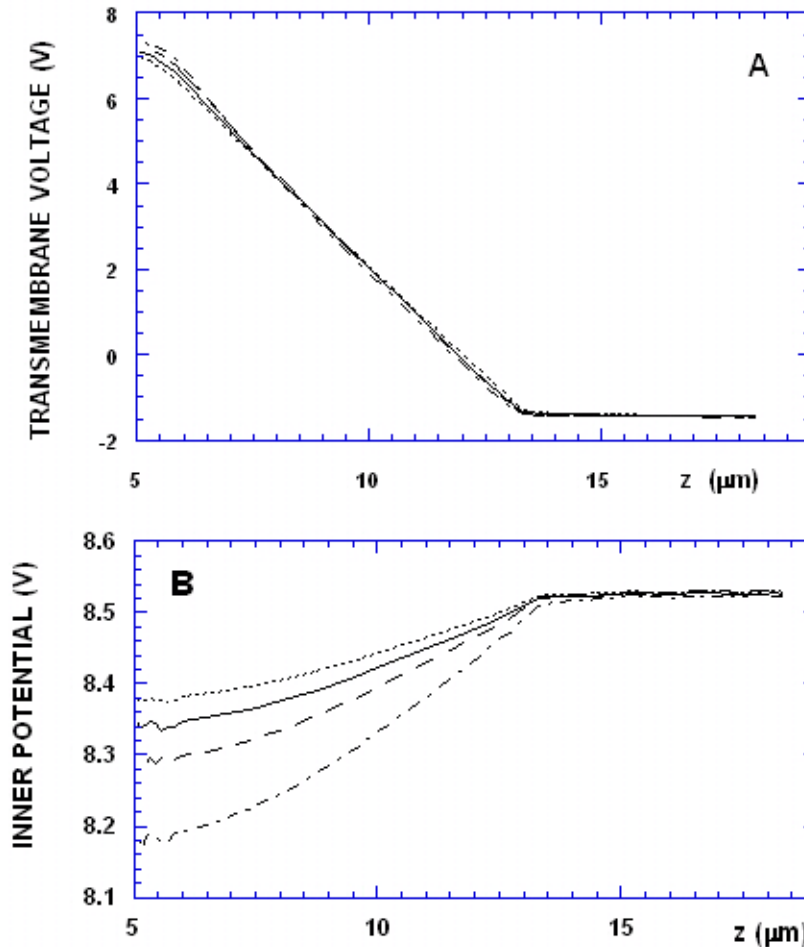


Figure 11. Calculated transmembrane voltage and potential along the membrane at different membrane and narrow passage thicknesses. Narrow passage thicknesses are: $0.125\mu\text{m}$ (dotted line), $0.1\mu\text{m}$ (solid line), $0.075\mu\text{m}$ (dashed line), $0.05\mu\text{m}$ (dash-dotted line). At every calculation the membrane thickness is taken equal with the thickness of the narrow passage. $z_{min} = 5.1\mu\text{m}$. a) Transmembrane voltage and b) the potential at the inner membrane surface is plotted against the z coordinate of the membrane segment. The voltage applied to the capacitor plates of the LVEP chamber is $V_{app} = 25V$.

This is the case because the simultaneous decrease of these two geometrical parameters similarly increases the electric field strength on both side of the membrane. On one hand by narrowing the passage the current density and the field strength increase in the passage. On the other hand by decreasing the membrane thickness the membrane resistivity decreases and more current flows into the cell finger, i.e. the field strength increases in the finger. In Table 2. the calculated field strengths are listed at different thicknesses of the narrow passage and cell membrane. The field strength inside the finger E_f is calculated from the steepest slope of the inner potential curve in Fig.11b. The field strength in the narrow passage E_p is calculated from the following relationship: $E_p = -dV/dz + E_n$, where dV/dz is the steepest slope of the transmembrane voltage curve in Fig.11a. Note that in the narrow passage the electric field strength increases only by 2% when the thickness of the narrow passage and cell membrane are simultaneously reduced by 50% .

Table 2. Electric Field in the Narrow Passage and in the Cell Finger

membrane thickness	narrow passage thickness	E_f	E_p
(μm)	(μm)	(V/cm)	(V/cm)
0.125	0.125	220.4	11584
0.1	0.1	278.3	11641
0.075	0.075	361.1	11725
0.05	0.05	531.9	11896

2. Effect of temperature and composition on the structure of two-component lipid membranes

2.1. Introduction

Important functions of cell membranes such as permeability of small water soluble molecules and signaling through in-plane chemical reactions¹ are strongly related to and affected by the lateral organization of the multi-component lipid matrix (Ref.2 and references therein). The functional significance of membranes' lateral heterogeneity is emphasized by recent discoveries in membrane cell biology. For example, the ability of glycosphingolipids to organize compositional clusters in biological membranes is postulated to be a key feature, not only in their own intracellular sorting and trafficking, but also in the sorting and trafficking of proteins with covalent glycosylphosphatidylinositol anchors. Glycosphingolipid clusters also called DIG's (detergent-resistant, glycosphingolipid-enriched complexes) or 'glycolipid rafts' may serve as target sites for the fusion/budding of envelope viruses with eukaryotic cells. Most of what is currently postulated about glycosphingolipid organization in cell membranes originates from studies of model membrane systems³⁻⁵.

Computer simulations of lipid bilayers makes it possible to study the relationships between the microscopic level membrane configurations and the phenomenological level membrane functions. For example it was proposed and demonstrated by computer simulations for one-component lipid membranes that there is a linear relationship between the bilayer permeability for small molecules and the length of the gel-fluid interface⁶⁻⁸.

There exist a broad range of models of phospholipid bilayers from the most detailed all-atom models⁹⁻¹¹ to Pink's 10-state model¹². From 1980 the 10-state model has been used frequently to simulate phenomena related to phospholipid mono- and bilayers¹³ such as permeability, protein-lipid interaction, effects of sterols, effects of drug binding, e.t.c. However, from 1994 we have seen from a growing number of examples that simple two-state models are able to simulate heat capacity curves and FRAP threshold temperatures of phospholipid bilayers in quantitative agreement with the observed DSC and FRAP data¹⁴⁻¹⁸. The simplicity of these models is exemplified by the gel-fluid transition of one-component lipid bilayers where it is assumed that each hydrocarbon chain exists in either a gel or fluid state, and only nearest neighbor interactions between the chains needs to be considered. These models are so called minimal models, making assumptions which are physically plausible and absolutely necessary for the correct simulation of the observed excess heat capacity curves. As a consequence the number of model parameters is minimal and the parameters have explicit physical meaning. The unique feature of this approach is that experimental data are used to estimate the values of the parameters.

In the first part of this chapter we describe a two-state, two-component minimal model of DMPC/DSPC mixtures developed by Sugar et al.,¹⁸. After the estimation of the model parameters we demonstrate that the model describes correctly the observed calorimetric data. In the second part the properties of the bilayer configurations, such as cluster size distribution, cluster number and percolation frequency of gel and fluid clusters at different mole fractions and temperatures, are calculated. We make a comparison between the calculated average size of gel clusters and the average linear size of the gel clusters observed by atomic force microscopy. We then point out the correlation between the calculated percolation temperature of gel clusters and the threshold temperature observed by FRAP at different DMPC/DSPC mole fractions. Finally, based on our simulation results we make a comparison between the predictions of the two existing theories of excess membrane permeability for small molecules.

2.2. Lattice Model of DMPC/DSPC Bilayers

Two-component lipid bilayers are the simplest model systems to study membrane lateral heterogeneity and its effect on membrane function. Among these model systems DMPC/DSPC mixtures have been studied most extensively experimentally¹⁹⁻³² and theoretically^{18,33-41}.

The minimal model of symmetric DMPC/DSPC bilayers described in this section is a straightforward generalization to two component bilayers of our two-state model for one-component systems^{14,16,17}. Monte Carlo methods are used to drive the model systems toward thermal equilibrium with the surrounding. After attaining equilibrium the actual bilayer configurations, produced by thermal fluctuations and lateral diffusion of the molecules, follow a Boltzmann distribution.

2.2.1. Lattice Geometry, States and Configuration

A monolayer of the DMPC/DSPC bilayer is modeled as a triangular lattice of N lattice points (coordination number $z=6$). Each lattice point is occupied by one acyl chain. The acyl chains of DMPC and DSPC molecules represent component (1) and component (2), respectively. In the lattice model nearest-neighbor pairs of similar acyl chains are interconnected forming either DMPC or DSPC molecules. $N_1/2$ and $N_2/2$ are the number of DMPC and DSPC molecules, respectively. Every lattice point can exist in two states corresponding to the gel (g) and liquid crystalline or fluid state (l).

The actual lattice configuration can be characterized by a square matrix \mathbf{S} and by a connection vector \mathbf{c} each containing N elements. Each matrix element S_{ij} represents a lattice point. In accordance with the triangular lattice geometry of the monolayer the following six matrix elements are the nearest neighbors of the ij -th matrix element S_{ij} : $S_{i-1,j-1}$, $S_{i-1,j}$, $S_{i,j-1}$, $S_{i,j+1}$, $S_{i+1,j}$, and $S_{i+1,j+1}$. The possible values of a matrix element 1, 2, 3 and 4 refer to component 1 in the g -state, component 2 in the g -state, component 1 in the l -state and component 2 in the l -state, respectively. Vector \mathbf{c} lists the lattice positions of the chemically connected pairs of acyl chains, i.e. c_k is the location of the acyl chain connected to the acyl chain in the k -th lattice point. The index ij of the \mathbf{S}

matrix elements and the index k of the \mathbf{c} vector elements are in the following relationship: $k = (j-1)\sqrt{N} + i$.

In modelling the transition of one-component phospholipid bilayers, it is not necessary to take into consideration the connections between the acyl chains of the molecules¹⁶. However, in the case of two-component phospholipid bilayers the connections must be considered in order to calculate correctly the mixing entropy and percolation threshold concentration of the system. Note, that although by using the independent chain model we could calculate the excess heat capacity curve of DMPC/DSPC (60/40) mixture in agreement with the experimental curve, the values of the model parameters were significantly different¹⁸ from those given in Table 1.

Table 1. Model Parameters of The Two-State Two-Component (DMPC/DSPC) Bilayer Model

Parameters	(cal/mol-chain)
ΔE_1	3,028
ΔE_2	5,250
w_{11}^{sl}	323.45
w_{22}^{sl}	352.32
w_{12}^{sg}	135
w_{12}^{ll}	80
w_{12}^{sl}	370
w_{12}^{lg}	410
	(cal/mol-chain/deg)
ΔS_1	10.19378
ΔS_2	16.01689

By analysis of the configuration matrix \mathbf{S} , one can obtain the number of i -th component in m -th state (N_i^m) and the number of certain pairs of nearest neighbor acyl chains (N_{ij}^{mn}), where one of the chains is of component i in state m and the other chain is of component j in state n .

There are simple relationships between the quantities defined above:

$$\begin{aligned}
 N &= N_1 + N_2 \\
 N &= N^s + N^l \\
 N_1 &= N_1^l + N_1^s \\
 N_2 &= N_2^l + N_2^s
 \end{aligned} \tag{1}$$

$$\frac{z}{2} N = N_{11}^{gg} + N_{11}^{gl} + N_{11}^{ll} + N_{12}^{gg} + N_{12}^{gl} + N_{12}^{lg} + N_{12}^{ll} + N_{22}^{gg} + N_{22}^{gl} + N_{22}^{ll}. \quad (2)$$

Periodic boundary conditions are utilized in order to eliminate the effects of the lattice edges⁴². These boundary conditions result in four additional relationships:

$$\begin{aligned} zN_1^g &= 2N_{11}^{gg} + N_{11}^{gl} + N_{12}^{gg} + N_{12}^{gl} \\ zN_1^l &= 2N_{11}^{ll} + N_{11}^{gl} + N_{12}^{ll} + N_{21}^{gl} \\ zN_2^g &= 2N_{22}^{gg} + N_{12}^{gg} + N_{22}^{gl} + N_{21}^{gl} \\ zN_2^l &= 2N_{22}^{ll} + N_{12}^{gl} + N_{22}^{ll} + N_{22}^{gl}. \end{aligned} \quad (3)$$

2.2.2. Configurational Energy and Degeneracy

Let E_i^m be the intrachain energy of an acyl chain of component (i) in state (m). In this model E_i^m is assumed to be constant and independent of the location and orientation of the rotational isomers in the acyl chain. It follows then that the energy levels E_1^l and E_2^l are highly degenerate. The degeneracy of the energy level of component (i) in state (m) is f_i^m .

E_{ij}^{mn} is the interchain interaction energy between component (i) in state (m) and component (j) in state (n). Only nearest neighbor interactions between the lattice points are considered, because Van der Waals interactions between the acyl chains are short-range¹. Since the interaction energies are assumed to be unaffected by the location and orientation of the rotational isomers in the interacting chains, the interaction energies are also degenerate; the degeneracy of interaction energy E_{ij}^{mn} is f_{ij}^{mn} .

The energy of one layer of the bilayer in configuration **S** is

$$\begin{aligned} E(S) &= E_1^g N_1^g + E_1^l N_1^l + E_2^g N_2^g + E_2^l N_2^l + E_{11}^{gg} N_{11}^{gg} + E_{11}^{gl} N_{11}^{gl} + E_{11}^{ll} N_{11}^{ll} + \\ &E_{12}^{gg} N_{12}^{gg} + E_{12}^{gl} N_{12}^{gl} + E_{21}^{gl} N_{21}^{gl} + E_{12}^{ll} N_{12}^{ll} + E_{22}^{gg} N_{22}^{gg} + E_{22}^{gl} N_{22}^{gl} + E_{22}^{ll} N_{22}^{ll}. \end{aligned} \quad (4)$$

The degeneracy of configuration **S** is calculated from the degeneracies of intrachain energies and the interchain energies

$$\begin{aligned} f(S) &= (f_1^g)^{N_1^g} (f_2^g)^{N_2^g} (f_1^l)^{N_1^l} (f_2^l)^{N_2^l} (f_{11}^{gg})^{N_{11}^{gg}} (f_{11}^{gl})^{N_{11}^{gl}} (f_{11}^{ll})^{N_{11}^{ll}} \\ &(f_{12}^{gg})^{N_{12}^{gg}} (f_{12}^{gl})^{N_{12}^{gl}} (f_{21}^{gl})^{N_{21}^{gl}} (f_{12}^{ll})^{N_{12}^{ll}} (f_{22}^{gg})^{N_{22}^{gg}} (f_{22}^{gl})^{N_{22}^{gl}} (f_{22}^{ll})^{N_{22}^{ll}} \end{aligned} \quad (5)$$

¹Long-range dipole-dipole interactions between the head groups of the molecules were originally incorporated into our model. However, in the case of DMPC/DSPC mixtures the effect of the dipole-dipole interaction on the calculated excess heat capacity curves was negligibly small.

2.2.3. Configurational Probability

The probability of configuration \mathbf{S} in the thermodynamic equilibrium is

$$p(S) = \frac{f(S)e^{-E(S)/kT}}{Q(N,T,V)} = \frac{e^{-\chi(S)/kT}}{Q(N,T,V)} \quad (6)$$

where $Q(N,T,V)$ is the partition function of the canonical ensemble of the lattice model, T is the absolute temperature, k is the Boltzmann constant, and V is the volume of the monolayer*. The function $\chi(S)$ is defined by

$$\chi(S) = E(S) - kT \ln f(S). \quad (7)$$

The configuration-dependent part of this function plays a central role in the Monte Carlo simulation. In order to reduce the number of model parameters we substitute Eqs.1-5 into Eq.7 and obtain $\bar{\chi}$, the configuration dependent part of $\chi(S)$

$$\bar{\chi}(S) = N_1^l (\Delta E_1 - T\Delta S_1) + N_2^l (\Delta E_2 - T\Delta S_2) + w_{11}^{gl} N_{11}^{gl} + w_{22}^{gl} N_{22}^{gl} + w_{12}^{gg} N_{12}^{gg} + w_{12}^{ll} N_{12}^{ll} + w_{12}^{gl} N_{12}^{gl} + w_{21}^{gl} N_{21}^{gl}. \quad (8)$$

where

$$\Delta E_i = [E_i^l + (z/2)E_{ii}^{ll}] - [E_i^g + (z/2)E_{ii}^{gg}] \quad (9)$$

$$\Delta S_i = k \ln f_i^l - k \ln f_i^g \quad (10)$$

$$w_{ij}^{mn} = [E_{ij}^{mn} - (E_{ii}^{mn} + E_{jj}^{nn})/2] - kT \ln \left[\frac{f_{ij}^{mn}}{\sqrt{f_{ii}^{mn} f_{jj}^{nn}}} \right] \quad (11)$$

2.2.4. Steps in the Monte Carlo Simulations

Each simulation can start from either the all-gel or all-fluid state or any state in between. Initially component (1) is assigned to the first N_1 lattice points, while component (2) is assigned to the remaining N_2 lattice points. Initially the molecules are similarly oriented, i.e.: the acyl chains on the first and second lattice points represent a phospholipid molecule, and in general the acyl chains on the $2k-1$ th and $2k$ th lattice points are connected, i.e.: $c_{2k-1} = 2k$. This "standard configuration", introduced first by Kasteleyn⁴⁴, can be easily generated. Note that Jerala, et al.¹⁶ started simulations from random orientations of the molecules. However, the generation of these initial random orientations was complicated because it was necessary to eliminate vacancies appearing in these configurations.

* In our model the volume change and the respective change in the volume energy associated with the gel to liquid crystalline phase transition are neglected⁴³.

2.2.5. Generation of Trial Configurations

During the Monte Carlo simulation, trial configurations of the two-component phospholipid bilayers are generated by means of three different elementary steps.

2.2.5.1. Local State Alteration. In this step the trial configuration is generated by changing the state of a randomly selected acyl chain from gel to fluid or from fluid to gel. This trial configuration generation, the Glauber method⁴⁵, is essential for the simulation of gel-to-fluid transitions of lipid bilayers.

2.2.5.2. Exchanging Different Molecules. In this step two randomly selected molecules, of different lipid components are exchanged. Although this elementary, non-physical step is different from the Kawasaki method⁴⁶, in which nearest neighbor molecules are exchanged, the rate of attainment of equilibrium of the lateral distribution of the bilayer components is improved⁴⁷.

2.2.5.3. Reorientation of a Pair of Nearest-Neighbor Molecules. In this step a pair of nearest neighbor molecules are randomly selected. If the positions of the selected acyl chains define the nodes of a rhombus then one of the chains and the chain on the opposite node are exchanged¹⁶. This exchange involves a rotation of the respective molecules by ± 60 degrees. A series of these elementary reorientations leads to the equilibrium distribution of the orientation of the molecules. Note that like the *exchange of different molecules*, the *reorientation step* results in the lateral movement of the molecules. Thus a series of *reorientation steps* is able to drive the system to the equilibrium of the lateral distribution of the molecules. However, as mentioned above, the non-physical steps of *exchanging different molecules* are also used to substantially accelerate convergence to the equilibrium distribution⁴⁷.

2.2.6. Decision Making

A trial configuration, S_{trial} , once generated, is acceptable when the following inequality holds:

$$RAN \leq \exp[-\{\bar{\chi}(S_{trial}) - \bar{\chi}(S_{orig})\}/kT]. \quad (12)$$

If it is not, the original configuration S_{orig} is retained. In Eq.12 RAN is a pseudo-random number, distributed uniformly in the interval (0,1). This method of decision making drives the system toward thermodynamic equilibrium, the Boltzmann distribution over all the possible configurations, independently of the choice of the initial configuration and the choice of the actual path toward equilibrium⁴⁷.

2.2.7. Defining the Monte Carlo Cycle

In a Monte Carlo simulation a certain chain of elementary steps, generating trial configurations, are repeated. During this chain of elementary steps, the Monte Carlo cycle, the system has the opportunity of realizing all of its configurations one time. N elementary steps of *local state alteration* give the opportunity of realizing any of the 2^N acyl chain states of the lattice.

By exchanging different molecules $(N/2)!/[(N_1/2)!(N_2/2)!]$ different arrangements of the molecules can be created. Any one of these arrangements can be realized by repeating the elementary steps of *exchange of different molecules* $N_1/2$ times (or $N_2/2$ times if $N_2 > N_1$).

An acyl chain at the i -th lattice point is connected with one of the six nearest neighbor acyl chains. Assuming independent orientations of the molecules, $3^{N/2}$ is the total number of different orientations in the lattice. In reality the orientations of the molecules are coupled and thus the number of possible orientations in the bilayer is much smaller. The probability that any selected lipid molecule has a neighbor that can participate in a reorientation step is 0.75 on a lattice with randomly oriented molecules¹⁶. After $N/2/0.75$ *reorientation steps* about 50% of the molecules has an opportunity to change orientation by $+60^\circ$, while the other half of the molecules can change orientation by -60° . Each orientation is accessible for each molecule at least once after performing $2([N/2]/0.75) = 4N/3$ *reorientation steps*.

2.2.8. Global State Alteration

In principle the equilibrium distribution of the system is attainable after many Monte Carlo cycles. In practice, however, the system could be trapped during the time of the simulation in one of the local free energy minima dependent on the initial configuration.

Accelerated convergence to the equilibrium distribution can be obtained by incorporating non-physical, shuffling operations into the algorithm⁴⁷. We incorporate a shuffling operation at the end of each Monte Carlo cycle. In this step the trial configuration is generated by altering the state of every acyl chain from gel to fluid and from fluid to gel.

The number of Monte Carlo cycles needed to attain the equilibrium depends on the lattice size, the actual values of the model parameters, temperature, mole fraction and the types of the steps generating trial configurations. To monitor convergence the membrane energy is calculated at the end of each Monte Carlo cycle. Starting the simulation from an all-gel state the membrane energy drifts toward larger values as the simulation progresses and after a certain number of Monte Carlo cycles it begins to fluctuate around a stationary value. This point signifies the attainment of equilibrium. In our Monte Carlo simulations, at every temperature and mole fraction, the equilibrium is attained at less than 6000 Monte Carlo cycles. After attaining the equilibrium another 6000 cycles are performed, and the snapshots are analysed after each cycle to extract quantities

characterising the membrane configuration such as lattice energy, cluster number, cluster size. From the distribution of these quantities thermodynamic averages are calculated. In order to calculate the excess heat capacity, a thermodynamic average which is directly measurable by scanning calorimetry, two different methods are utilized. After determining the average lattice energy at fifty different temperatures, the excess heat capacity curve is obtained from the numerical derivative of the calculated energy curve. In an alternative method the variance of the energy at different temperatures is calculated in order to obtain directly the excess heat capacity curve¹⁷. This method is more time consuming, however, because of convergence to the equilibrium value of the energy variance is an order of magnitude slower than convergence to the energy average⁴⁸. Note that in the case of our simulation protocol the above two methods resulted in practically the same excess heat capacity values.

2.2.9. Determination of The Model Parameters

The $\bar{\chi}(S)$ function, Eq.8, contains 10 unknown model parameters: ΔE_1 , ΔE_2 , ΔS_1 , ΔS_2 , w_{11}^{gl} , w_{22}^{gl} , w_{12}^{gg} , w_{12}^{ll} , w_{12}^{gl} , w_{21}^{gl} . The model parameters have been determined by the following strategy. ΔE_1 and ΔE_2 are estimated by means of the integral of the measured excess heat capacity curves of single component DMPC and DSPC MLV's, respectively.

In order to obtain the maxima of the calculated excess heat capacity curves of the one-component systems at the respective measured temperatures of the heat capacity maxima, T_{m1} and T_{m2} , the model parameters should satisfy the following two constraints:

$$\Delta S_1 \approx \Delta E_1 / T_{m1} \quad (13)$$

$$\Delta S_2 \approx \Delta E_2 / T_{m2} \quad (14)$$

These approximate relationships can be derived when the parameters w_{11}^{gl}, w_{22}^{gl} are equal to zero and $2kT_{mi} = \Delta E_i$ (Ref.18). In the case of a DSPC bilayer the above approximation results in an error of about 3% in the value of ΔS_2 .

The remaining two parameters of the one-component systems, w_{11}^{gl} and w_{22}^{gl} , were estimated by comparing the experimental excess heat capacity at T_{mi} of each one-component system with a series of excess heat capacities calculated at different values of the respective w_{ii}^{gl} parameter. The parameters resulting in a good fit are listed in Table 1.

In Table 1 the parameters, $w_{11}^{lg} = 323.45$ cal/mol'chain and $w_{22}^{lg} = 352.32$ cal/mol'chain, are of the same magnitude as the value of the parameter obtained from the similar analysis of the excess heat capacity curve of DPPC SUV^{14,16,17}. The somewhat larger value obtained here is the result of higher cooperativity associated with the gel-fluid transition of MLV as described by the narrower excess heat capacity function.

The positions of the high- and low-temperature peaks in the excess heat capacity curves for the binary mixtures are strongly related to the values of the parameters w_{12}^{gg} and w_{12}^{ll} . In the case of a 60/40 mixing ratio, the calculated low- and high-temperature peaks in the excess heat capacity curves were obtained in agreement with the observed peak positions by assuming $w_{12}^{gg} = 135 \text{ cal/mol-chain}$ and $w_{12}^{ll} = 80 \text{ cal/mol-chain}$. This result shows that the pure fluid phase is closer to an ideal mixture than the pure gel phase, as expected.

The values of the remaining two parameters, w_{12}^{lg} and w_{12}^{gl} were estimated simultaneously, by comparing the calculated excess heat capacity curve, obtained at different pairs of the parameter values, with the experimental excess heat capacity curve at a mixing ratio of 60/40. The parameters obtained from the parameter estimation are listed in Table 1. These set of parameters were used in all the subsequent simulations. In estimating these parameters, it was assumed that the w_{ij}^{kl} parameters are independent of temperature. We note that the method suggested by Ferrenberg and Swendsen⁴⁹ of accelerating multiparameter fitting is not practical in our Monte Carlo simulations because the tabulation of the distribution function of $N_1^l, N_2^l, N_{11}^{gl}, N_{22}^{gl}, N_{12}^{gg}, N_{12}^{ll}, N_{12}^{lg}, N_{12}^{gl}$ in an 8 dimensional matrix requires a prohibitively large memory.

2.3. Results and Discussion

2.3.1. System Size and Type of The Transition

All calorimetric scans were performed on a home-made high sensitivity calorimeter⁵⁰ at scan rates from 0.1 to 5 °C/h and lipid concentrations of 20-22mM. The obtained excess heat capacity curves were scan rate independent at these slow scanning rates. The excess heat capacity curves of one-component DMPC and DSPC bilayers showed a very sharp, symmetric peak with a heat capacity maximum of

$$C_p(T_{m1} = 297.044K) = 40,000 \text{ cal/mol} \cdot \text{chain/deg} \text{ and}$$

$$C_p(T_{m2} = 327.779K) = 24,000 \text{ cal/mol} \cdot \text{chain/deg} ,$$

respectively. By using the parameters, listed in Table 1, the simulated excess heat capacity maxima agree with the respective experimental data if the lattice size is large enough. Fig.1a shows that the calculated excess heat capacity maxima become independent from the system size at a threshold linear system size of 100 and 250 for DSPC and DMPC, respectively. In Fig.1b the threshold linear lattice sizes are shown at different DMPC/DSPC mole fractions. In order to eliminate finite size effects one has to perform simulations for lattice sizes which are larger than these threshold values. In the present simulations the following lattice sizes are utilized: 350x350 for DMPC; 300x300 for DSPC; 100x100 for DMPC/DSPC mixtures of mixing ratios 10/90, 20/80, 90/10, 80/20; and 40x40 for DMPC/DSPC mixtures of mixing ratios 30/70, 40/60, 50/50, 60/40, 70/30.

It is important to mention that by varying the system size not only quantitative but also qualitative changes take place in the transition properties of the simulated bilayer, i.e.:

change in the type of the transition. In general the type of the transition can be characterized by the distribution of the fluctuating extensive parameters of the system taken at the midpoint of the transition. If the distribution is unimodal the transition is continuous (or 2nd order transition), otherwise it is a phase transition (or 1st order transition). In our model, membrane energy is the only fluctuating extensive parameter of the system (canonical ensemble). At the midpoint of the gel-fluid transition the calculated energy distribution is bimodal or unimodal if the system size is below or above the threshold size. In Figs.1c and d the energy distributions, calculated above and below the threshold size, are shown at 70/30 and 0/100 DMPC/DSPC mole fractions, respectively. Thus with increasing lattice size the gel-fluid transition changes at a threshold size from 1st order to 2nd order transition, i.e.: at the thermodynamic limit the transition is continuous (2nd order transition) at every mole fraction.

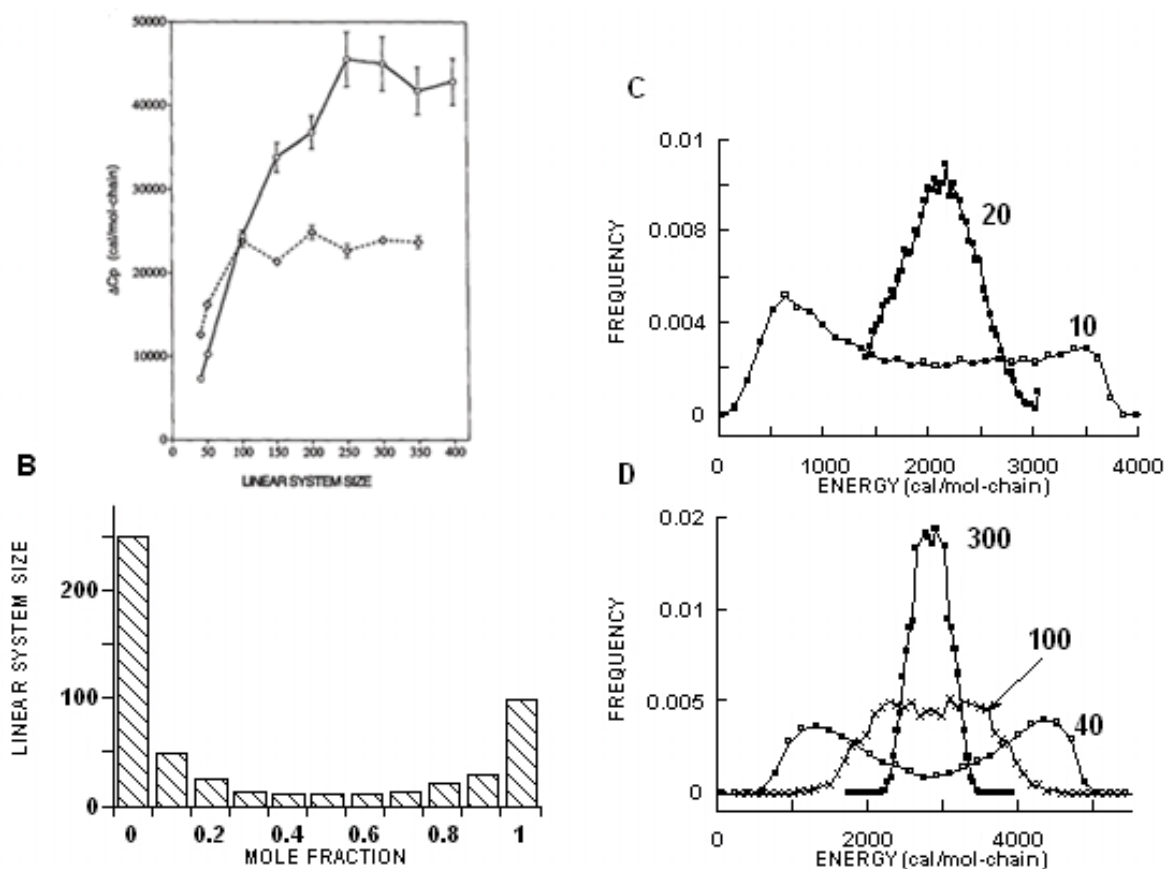


Figure 1. *Finite Size Effects.* a) Excess heat capacity maxima, calculated by using Eq.20 at different linear system sizes. Solid line: DMPC, $T=297.044\text{K}$, dashed line: DSPC, $T=327.779\text{K}$. The error bars were calculated from the result of eight computer experiments started with different seed numbers for random number generation. In each computer experiment the number of Monte Carlo cycles was 10^5 , and the system was equilibrated during the first 6000 cycles. b) Threshold linear system sizes at different mole fractions of DMPC/DSPC mixtures. c) and d) Energy distributions calculated at 70/30 and 0/100 DMPC/DSPC mole fractions, respectively. Each distribution is labelled by the respective linear system size.

2.3.2. Excess Heat Capacity Curves and Melting Curves

In Fig.2 the experimental and calculated excess heat capacity curves are shown at different DMPC/DSPC mixing ratios. The excess heat capacity was calculated from the energy fluctuation according to Eq.20. Each simulation was performed using the model parameters listed in Table 1. There is an excellent agreement between the calculated and experimental excess heat capacity curves for DMPC/DSPC mole fractions of 60/40, 50/50, 40/60, 30/70, 20/80 and 10/90 while for the other mole fractions, though the location of the calculated peaks is correct, the heights of the low-temperature peaks are significantly smaller than the experimental ones.

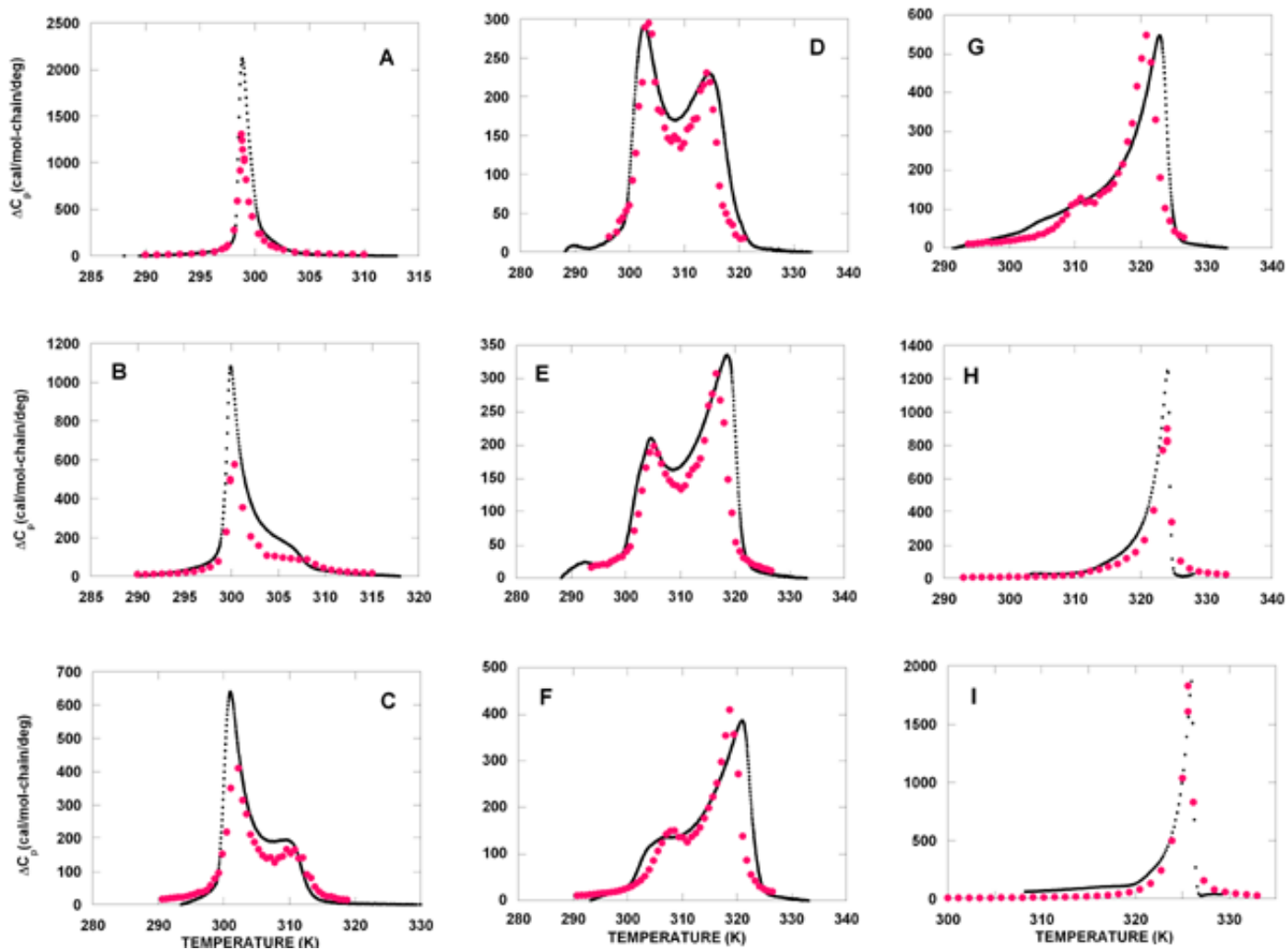


Figure 2. *Excess Heat Capacity Curves.* Excess heat capacity curves. Solid line: Experimental excess heat capacity curves; red dots: excess heat capacity curves calculated by means of Eq.20. DSPC mole fractions are: a) 0.1, b) 0.2, c) 0.3, d) 0.4, e) 0.5, f) 0.6, g) 0.7, h) 0.8, i) 0.9.

These deviations may be related to the fact that the experimental DMPC gel-to-fluid transition enthalpy, 3,028 cal/mol·chain, underestimates the true transition enthalpy. In our experiment, to ensure equilibrium-transition of DMPC, a particularly slow scanning rate, $0.1C^{\circ}/h$, was utilized within a temperature range of only $0.6C^{\circ}$ and the transition enthalpy was determined by integrating the excess heat capacity curve over this short temperature range. The existence of large "wings" on the high and low temperature side of the heat capacity curves of one component phospholipid bilayers, noted first by Mouritsen¹³, however, would require integration over a longer temperature range for the better estimation of the transition enthalpy. In the case of DSPC a three times larger temperature range was scanned and thus the integration over this temperature range gives a better estimate of the true transition enthalpy.

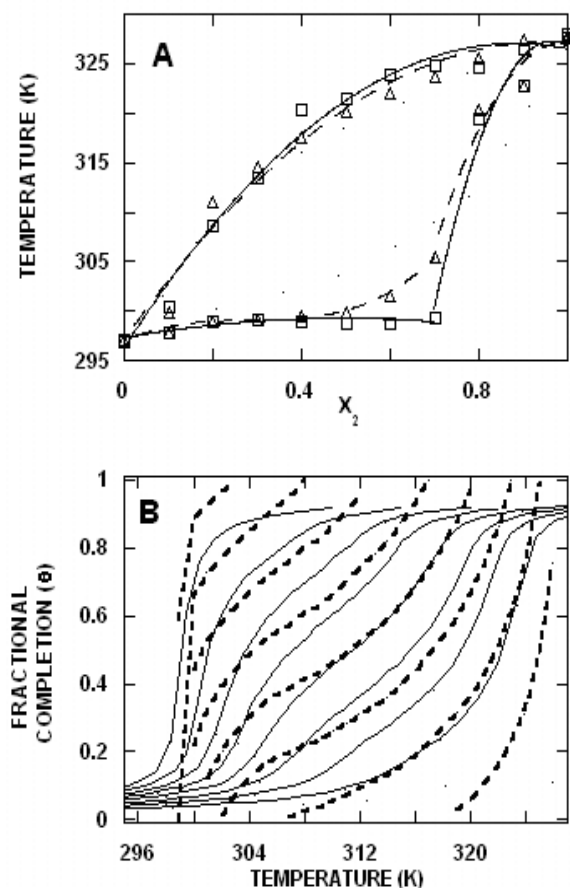


Figure 3. 'Phase Diagrams' and Melting Curves. a) 'Phase diagrams' constructed from the excess heat capacity curves in Fig.2. The open triangles and open squares, representing respectively the calculated and experimental onset and completion temperatures of the gel-to-fluid transition at different DSPC mole fractions, were used to construct the solidus and liquidus lines of the 'phase diagrams'. b) Comparison of the melting curves calculated directly from the simulations (see Eq.16) (solid lines) and by using the 'phase diagram' in Fig.3a and the lever rule (see Eq.15) (dashed lines). The curves from left to right belong to the following DSPC mole fractions: 0.1, 0.2, 0.3, 0.4, 0.5, 0.6, 0.7, 0.8.

The experimental excess heat capacity curves are commonly used to construct so called 'phase diagrams' of the two-component lipid bilayers. The solidus and liquidus curves of the diagram are created by plotting the onset and completion temperatures, respectively,

against the mole fraction⁺ Fig.3a shows two 'phase diagrams' constructed from the experimental and calculated excess heat capacity curves.

It is important to emphasize, however, that these are not phase diagrams in a strict thermodynamic sense because the gel-fluid transition of DMPC/DSPC mixtures is not a first order phase transition. At a given temperature, T, the solidus and liquidus curve of a real phase diagram define the compositions in the coexisting solid (X^s) and liquid (X^l) phase regions, respectively, and these compositions remain constant when the total mole fraction (X) is changed. These properties of the first order phase transitions and real phase diagrams result in the lever rule:

$$\theta(T) = [X - X^s(T)]/[X^l(T) - X^s(T)] \quad (15)$$

where $\theta(T)$ is the fractional completion of the transition at temperature, T. Since the gel-fluid transition in DMPC/DSPC mixtures is not a first order phase transition the diagrams in Fig.3a are not real phase diagrams and the lever rule is not applicable to get the fractional completion of the transition. It is shown in Fig.3b that a mechanical application of the lever rule to the 'phase diagrams' in Fig.3a results in serious errors in the estimation of the fractional completion of the gel-fluid transition (see dashed lines). Solid lines show the correct fractional completion curves calculated from the simulated data as follows:

$$\theta(T) = [\langle N_1^l(T) \rangle + \langle N_2^l(T) \rangle]/N \quad (16)$$

⁺ A straight line is fitted to the inflexion point of the excess heat capacity curve close to the completion of the transition and its intercept with the baseline defines the completion temperature. A similar procedure close to the onset of the transition defines the onset temperature.

2.3.3. Domain Structure of The Membranes

The good agreement between the observed and calculated excess heat capacity curves increases our confidence in the simple two-state bilayer model and thus we perform computer experiments to study the thermodynamic averages which are characteristic to the configuration of two-component bilayers. A membrane domain or cluster is a group of lipids in lateral proximity sharing a certain property. For example a compositional cluster is a cluster of similar lipid molecules existing in either gel or fluid state. On the other hand a gel cluster is formed by gel-state lipid molecules of any lipid components.

The reason of cluster formation lies in the lateral heterogeneity of the membranes. The number, size and shape distribution of the clusters are related to the physical conditions such as temperature, pressure, mole fraction and also to the interactions between the components of the membrane. In the case of one-component bilayers the effects of the three different interchain interactions (g-g, g-l and l-l) on the cluster formation can be characterized by a single parameter, w_{11}^{gl} , which is a combination of the interchain interaction energies and degeneracies (see Eq. 11).

When $w_{11}^{gl}/kT \approx 0$ gel- and fluid-state molecules are randomly distributed; the average number of gel-state molecules in the proximity of a gel-state molecule is solely determined by chance (by the concentration of gel-state molecules). The cluster shapes are irregular ensuring high entropy which minimizes the free energy of the system. With increasing values of w_{11}^{gl}/kT the average size of the gel and fluid clusters increases, while their average number decreases, and complete phase separation takes place when $w_{gl}/kT \gg 1$. With increasing value of w_{11}^{gl}/kT the cluster shapes become less irregular and when $w_{gl}/kT \gg 1$ the shape of the remaining single cluster becomes close to circular. In this case the free energy minimum of the system is associated with the minimal system energy maintained by minimal cluster periphery to cluster size ratio.

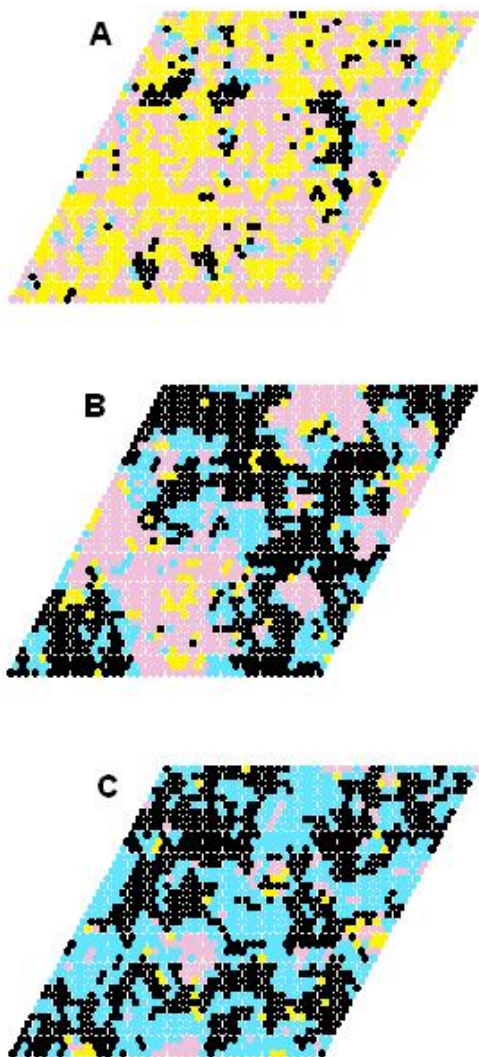


Figure 4 Snapshots from an Equimolar Mixture of DMPC/DSPC. a) $T=321\text{K}$, b) $T=307\text{K}$, c) 302K . Black dot: DSPC chain in gel state; yellow dot: DSPC chain in fluid state; blue dot: DMPC chain in gel state; pink dot: DMPC chain in fluid state.

In the case of DMPC/DSPC mixtures the effect of ten different interchain interactions (1g-1g, 1g-2g, 2g-2g, 1l-1l, 1l-2l, 2l-2l, 1g-1l, 1g-2l, 2g-1l and 2g-2l) on the cluster formation can be characterized by six w_{ij}^{kl} parameters (see Eq.11). At room temperature $0 < w_{ij}^{kl}/kT < 1$ (see Table 1) and thus one can expect small, irregular shape clusters of the minor phase. Small, irregular shape gel and fluid clusters are shown in the snapshots in Fig.4a and Fig.4c, respectively. These snapshots of equimolar DMPC/DSPC mixtures were simulated by using our simple two-state model. The average characteristics of these small clusters can be determined by means of cluster statistics.

2.3.4. Cluster Statistics

The snapshots were analysed after every Monte Carlo cycle using a cluster counting algorithm^{17,52} to obtain the cluster size distributions, cluster numbers and percolation

frequencies. The cluster counting algorithm labels each cluster in a snapshot with different number and then the labelled clusters are analysed and sorted according to certain properties such as size, number and shape.

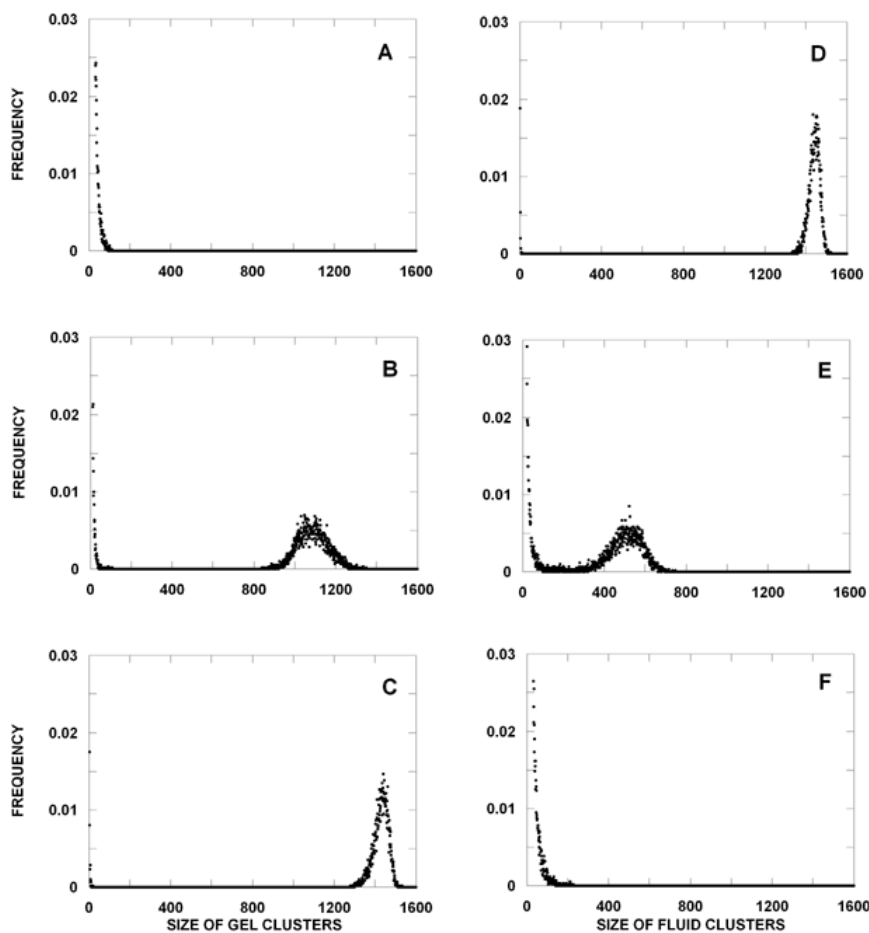


Figure 5. *Cluster Size Distributions in an Equimolar Mixture of DMPC/DSPC* a-c) Gel clusters; d-f) fluid clusters. Temperatures: a,d) 321K; b,e) 307K; c,f) 302K.

Figs.5a-c show the size distributions of gel clusters at three different temperatures for the equimolar mixture of DMPC/DSPC. The size distribution of the gel clusters is unimodal above a certain threshold temperature and the bilayer contains only 'small' gel clusters. These so called *percolation thresholds temperatures of the gel clusters*, T_{perc}^g are listed in Table 2 at different mole fractions. 'Large' gel clusters appear in the bilayer below the percolation threshold temperature and the cluster size distribution is bimodal. In this case the position of the minimum between the two peaks of the bimodal distribution separates the 'small' clusters from the 'large' ones.

Table 2. Calculated and Experimental Percolation Threshold Temperatures of The Gel to Fluid Transitions^a

X_2	0.3	0.4	0.5	0.6	0.7
T_{peak1}	302.3	303.8	304.9	307.8	310.4sh
T_{peak2}	310.4	314.4	316.9	318.9	321.3
T_{perc}^l	300.8	302.2	303.9	308.5	313.1
T_{perc}^g	309.1	313.8	317.5	320.6	323.0
$T_{perc0.36}^g$	307.1	311.9	315.9	318.9	321.5
T_{FRAP}	306.6	312	316	319	321.5

^a In DMPC/DSPC Lipid Bilayers at Different DSPC mole fractions, X_2 . *sh* marks the temperatures at shoulders of the excess heat capacity curves; T_{peak1} : calculated temperature at the low-temperature peak of the excess heat capacity curve; T_{peak2} : calculated temperature at the high-temperature peak of the excess heat capacity curve;

T_{perc}^l : calculated percolation threshold temperature of fluid clusters; T_{perc}^g : calculated percolation threshold temperature of gel clusters; $T_{perc0.36}^g$: temperature where the percolation frequency of gel clusters is 0.36; T_{FRAP} : threshold temperature from the FRAP experiment²⁸. The determination of the percolation threshold temperature is similar to that of the completion temperature of the transition. A straight line is fitted to the inflexion point of the percolation frequency curve (Figs.7a,b) and its intercept with the zero frequency line defines the percolation threshold temperature.

The situation is just the opposite for the size distribution of fluid phase clusters (see Figs.5d-f). Below the *percolation threshold temperature of fluid clusters*, T_{perc}^l (Table 2) the size distribution is unimodal with a peak at small cluster size. Above the percolation temperature, however, an additional peak appears at large cluster sizes, i.e. the cluster size distribution becomes bimodal.

2.3.5. Cluster Number

The integral of the size distribution provides the average number of clusters in the lattice. In Fig.6 the average number of gel and fluid clusters are plotted against the temperature. With decreasing temperature the number of gel phase clusters increases up to a maximum, at 322K. Below this temperature the number of gel clusters starts to decrease because the clusters coalesce forming eventually a 'large' gel cluster. With increasing temperature the number of fluid phase clusters increases up to a maximum, at 302K. Above this temperature the coalescence of fluid phase clusters dominate over the cluster formation and thus the number of clusters starts to decrease. It should be noted that at a temperature at which it is generally assumed that the system exists in a single structural phase (e.g. 280 K for the gel and 350 K for the fluid phase) the average number of clusters of the minor phase is still significant. This is indicative of lateral density heterogeneities existing far from the transition range^{2,51}.

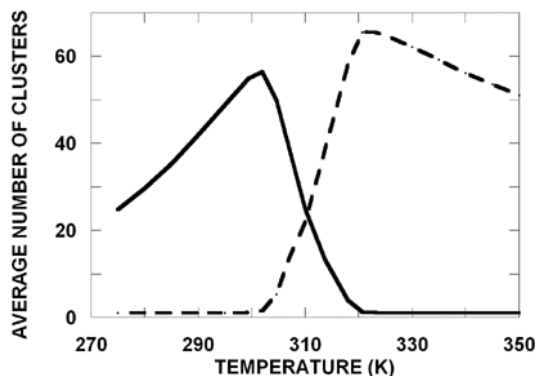


Figure 6. Average Cluster Numbers in an Equimolar Mixture of DMPC/DSPC. Solid line: fluid clusters; dashed line: gel clusters.

2.3.6. Cluster Percolation

When the cluster size distribution is bimodal on the average there is only one 'large' cluster in the lattice. A 'large' cluster is percolated if it spans the lattice either from the top to the bottom or from the left to the right edge⁵². The frequency of the appearance of a percolated cluster at the end of each Monte Carlo cycle is the percolation frequency. In Fig.7a and b the percolation frequencies of fluid and gel clusters are plotted against the temperature at different mixing ratios. The percolation threshold temperatures of the fluid and gel clusters, T_{perc}^f and T_{perc}^g listed in Table 2, are in good agreement with the peak positions of the excess heat capacity curve T_{peak1} and T_{peak2} , respectively.

Direct observation of cluster percolation is not available. Fluorescent recovery after photobleaching (FRAP) provides indirect information on the connectedness of clusters. Recovery takes place when fluorescent molecules diffuse from the unbleached area of the membrane to the photobleached area. Practically there is no recovery in pure gel phase since the lateral diffusion of the fluorescent labelled lipid molecules is thousand times slower in gel phase than in fluid phase²⁸. In a gel-fluid mixed phase the recovery suddenly increases from a threshold temperature, T_{FRAP} . FRAP threshold temperatures were measured by Vaz et al.²⁸ at different mole fractions of DMPC/DSPC mixtures. It is assumed that the FRAP threshold is related to the percolation threshold temperature of either the gel or the fluid clusters. The long range lateral diffusion of the fluorescent probe becomes blocked when the percolation of gel clusters takes place or the long range lateral diffusion of the probe becomes possible at the percolation of fluid clusters⁺⁺. The

⁺⁺ It is important to note that percolation of gel and fluid clusters is not mutually exclusive. It is possible for example that a gel cluster spans horizontally the upper part of the lattice while the lower part of the lattice is spanned horizontally by a fluid cluster. Thus there is a temperature range where both gel and fluid clusters can be percolated. For example according to the calculated cluster size distributions at 307K there are both 'large' gel and 'large' fluid clusters (see Figs.5b and e). The percolation frequency of these 'large' clusters is 1.0 and 0.46 for gel and fluid clusters, respectively.

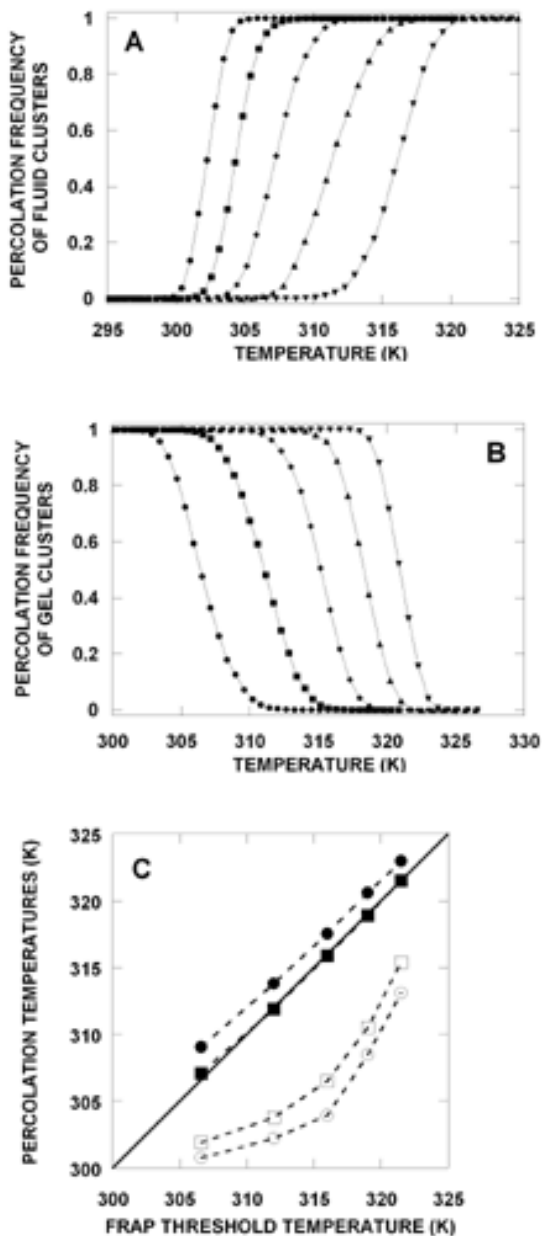


Figure 7. Percolation frequency of gel and fluid clusters in DMPC/DSPC mixtures. a) Calculated percolation frequency of fluid clusters vs. temperature. b) Calculated percolation frequency of gel clusters vs. temperature. DSPC mole fractions are (from left-to-right): 0.3 (dot), 0.4 (square), 0.5 (diamond), 0.6 (triangle), 0.7 (upside down triangle). c) Four characteristic temperatures of the percolation curves are plotted against the FRAP threshold temperatures measured at different DMPC/DSPC mole fractions. Closed circles: percolation threshold temperatures of gel clusters; open circles: percolation threshold temperatures of fluid clusters; open squares: temperatures at 0.36 percolation frequency of fluid clusters; closed squares: temperatures at 0.36 percolation frequency of gel clusters (The slope of the regression line is 1.00 ± 0.02 , while the linear correlation coefficient is: $r=0.9994$).

correct interpretation of the FRAP data can be made by using the results of our simulations. In Fig.7c the calculated percolation threshold temperatures of gel and fluid clusters are plotted against the measured FRAP threshold temperatures. The correlation is weak for fluid clusters but there is a strong positive correlation between the threshold temperatures for gel clusters with a constant difference of 1.8°C between the calculated and measured threshold temperatures. However if we plot the temperatures, $T_{perc0.36}^g$, where the percolation frequency of the gel clusters is 0.36 against the FRAP threshold temperatures the two sets of temperatures is completely identical. In conclusion, at the FRAP threshold temperature the percolation probability of the gel clusters is 0.36, and below this percolation frequency gel clusters cease to block efficiently the long-range diffusion of the fluorescence probe molecules.

2.3.7. 'Small' Clusters

Because the 'small' clusters are so small their direct detection is very difficult^{25,31}. In 1998 Gliss et al.³² obtained estimates of the average linear size of gel clusters by using neutron scattering and atomic force microscopy. The neutron diffraction measurements on equimolar DMPC/DSPC mixture at 38 and 41 °C resulted in an average center to center distance between adjacent gel domains of 5–10nm. Atomic force microscopy studies supported the above estimate for the average size of gel domains and showed rather irregular cluster shapes.

What is the average size of the 'small' gel clusters in our simulations? By using the cluster size distribution one can calculate the weighted average of the size of the 'small' clusters as follows:

$$\langle s \rangle = \frac{\sum_{i=1}^{i_{th}} i^2 P(i)}{\sum_{i=1}^{i_{th}} i P(i)} \quad (17)$$

where $P(i)$ is the probability of finding a cluster of size i (i.e. the number of i -size clusters to the total number of clusters); i_{th} is the threshold cluster size separating the 'small' clusters from the 'large' ones. The threshold cluster size is defined by the local minimum between the two maxima of the bimodal cluster size distribution. In the case of unimodal cluster size distribution $i_{th} = N$, where N is the number of hydrocarbon chains in a layer of the bilayer.

What is the meaning of the above defined weighted average? Let us pick hydrocarbon chains randomly from the lipid layer. Every time when the hydrocarbon chain is an element of a 'small' cluster the respective cluster is selected. The average size of the selected clusters is the weighted average of the 'small' clusters. This definition involves that larger clusters are selected more frequently than smaller ones, i.e.: the average is weighted by the cluster size. We introduced this weighted average because the observed average linear size of the clusters is a similarly weighted average³². In Figs.8 the weighted average size of the clusters is plotted against the temperature at different mole fractions of DMPC/DSPC. Each curve has a sharp maximum superimposing to a broad hump. In Fig.8a the average size of the 'small' gel clusters approaches one at low temperature. At this temperature the membrane is close to all-gel state, and only very small fluid clusters can be present. Within a small fluid cluster of size ≥ 7 chains a 'small' gel cluster of size $i \approx 1$ chain can form, while the probability of finding gel clusters of size $i=2$ or 3 is much smaller. Thus at low temperature the size distribution function of 'small' gel clusters is: $P(1) \approx 1$ and $P(i) \approx 0$ for $i > 1$, which results in $\langle s \rangle \approx 1$ for the weighted average size of the 'small' gel clusters (see Eq.17).

Approaching the equimolar mixing the broad hump disappears because the two peaks overlap each other. The height and the half width of the sharp peaks is 110 ± 20 chains

and $2^\circ C$, respectively. The height and the half width of the broad hump: 25 ± 5 chain and $15^\circ C$, respectively can be estimated from those curves where the broad hump is separated from the sharp peak. The average linear size of the irregular shape, 'small' clusters $\langle l \rangle$ is estimated by using the average cluster size $\langle s \rangle$ as follows:

$$\sqrt{4\langle s \rangle A_o / \pi} < \langle l \rangle < \langle s \rangle \sqrt{4A_o / \pi} \quad (18)$$

where the cross sectional area of a chain is $A_o = 20\text{\AA}^2$ in gel phase and $A_o = 31\text{\AA}^2$ (Ref. 63) in fluid phase. In Eq.18 the lower and upper limit assumes circular and linear shape clusters, respectively. By using Eq.18 the linear size of the clusters at the sharp peaks in Figs.8 is $5nm < \langle l \rangle < 50nm$ for 'small' gel clusters and $6nm < \langle l \rangle < 62nm$ for small fluid clusters. The linear cluster size at the broad hump in Figs.8 is $2.5nm < \langle l \rangle < 13nm$ for gel clusters and $3nm < \langle l \rangle < 15nm$ for fluid clusters.

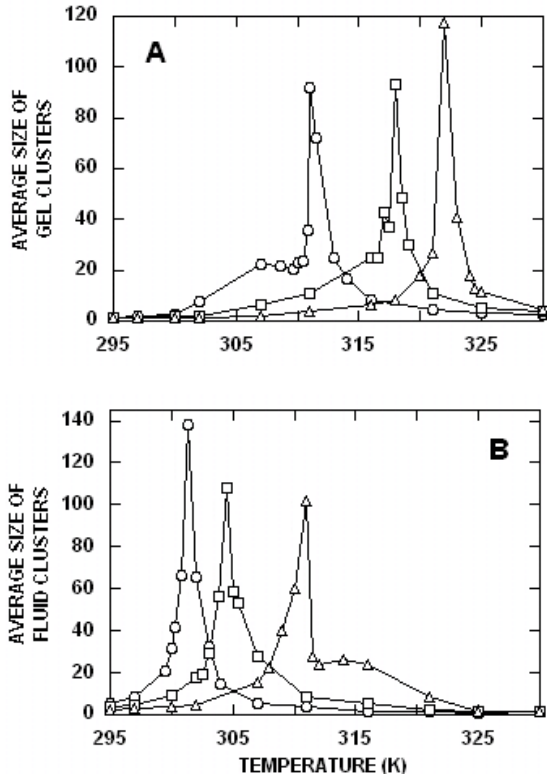


Figure 8. Average Cluster Size of 'Small' Clusters. Temperature dependence of the weighted average cluster size calculated by using Eq.17. a) Gel clusters; b) fluid clusters. DSPC mole fractions: 0.3 (open circle), 0.5 (open square), 0.7 (open triangle).

The average linear size of the gel clusters observed directly for an equimolar mixture of DMPC/DSPC at three different temperatures 38 , 41 and $55^\circ C$ are $5-10nm$, $5-10nm$ and $0nm$ (Ref. 32). These linear cluster sizes are in agreement with the calculated cluster size values. From Fig.8a the average size of gel clusters for equimolar mixture at 38 , 41 and $55^\circ C$ are 11 , 18 and $0chain$, and by using Eq.18 the respective average linear size of the gel clusters are: $1-6nm$, $2-9nm$ and $0nm$.

It is interesting to follow the formation of fluid clusters in the DMPC/DSPC (30/70) mixture. At 300K 'small', DMPC-rich, fluid clusters are present. With increasing temperature the number and size of the fluid clusters increases. At 311K as a result of the coalescence of many 'small' fluid clusters a few larger clusters form each containing about 25 hydrocarbon chains. Some of these larger clusters are close to each other, and they can easily connect with each other to form an even larger fluid cluster containing about 100 hydrocarbon chains. A slight further increase in the temperature leads to the permanent presence of one 'large' cluster which very rarely spans the whole length of the membrane layer. At 311K the percolation frequency of the fluid clusters is almost zero (Fig.7a). The permanent appearance of this 'large' cluster transforms the unimodal cluster size distribution into bimodal distribution. Once a cluster becomes permanently 'large' it does not count in calculating the average size of the 'small' clusters. Thus the average size of the 'small' clusters drops to about 25 chains. This is the size of the larger clusters among the 'small' clusters. These clusters are so much separated from each other that they cannot immediately coalesce with each other. When the temperature increases smaller clusters attach to the larger ones increasing slightly the average size of the small clusters. From about 314K, however the increasing larger clusters get near to the similarly increasing 'large' cluster. When the larger ones among the 'small' clusters start to coalesce with the 'large' cluster the average size of the 'small' clusters starts to decrease.

2.3.8. Membrane Permeability

The permeability of one- and two-component phospholipid bilayers to small water-soluble molecules may be larger at temperatures when gel and fluid phases coexist than when the bilayers are in either all-gel or all-fluid phase^{6,53-59}. Similar to the construction of the excess heat capacity curve from the heat capacity curve one can create the excess permeability curve from the permeability curve. In the cases of one-component phospholipid bilayers and close to ideal mixtures of DMPC/DPPC⁵⁹ the excess permeability curve possesses one maximum at the midpoint temperature of the gel-to-fluid transition. There are no data available for the excess permeability of non-ideal binary mixtures, such as DMPC/DSPC.

Two-dimensional membrane models attributed the excess permeability to the increased fluctuations of the membrane area close to the gel-fluid transition^{43,60}. Three-dimensional membrane models emphasize the role of free-volume in membrane permeability and thus one may explain the excess permeability by the increased fluctuations of the membrane volume close to the gel-fluid transition.

According to an other idea the acyl chain packing mismatch at the interfacial region between gel and fluid domains is the main reason of the excess permeability⁶⁻⁸. In this chapter we refer to these models of membrane permeability as the 'area/volume fluctuation' model and 'phase mismatch' model, respectively. Excess permeability curves observed for one-component membranes and for the ideal mixtures of DMPC/DPPC are in agreement with the predictions of both of these models^{6,8,43-60}.

In this section by using our simulated data we point out that in the case of the non-ideal mixture of DMPC/DSPC there is a discrepancy between the excess permeability curves predicted by these two models.

According to the 'phase mismatch' model the excess permeability is proportional to the average length of gel-fluid interface $\langle L \rangle$. A normalized average length of gel-fluid interface can be calculated from our simulated thermodynamic averages as follows:

$$\langle L \rangle / L_o = [\langle N_{11}^{gl} \rangle + \langle N_{12}^{gl} \rangle + \langle N_{21}^{gl} \rangle + \langle N_{22}^{gl} \rangle] / 3N \quad (19)$$

where L_o is the sum of the nearest neighbor interchain distances and $3N$ is the number of nearest neighbor chain-chain interactions. The normalized average length of the gel-fluid interface is calculated from our Monte Carlo simulations and plotted in Fig.9 against the temperature at different DMPC/DSPC mixing ratios. According to the 'phase mismatch' model these curves should be similar to the excess permeability curves measured at the respective mixing ratios.

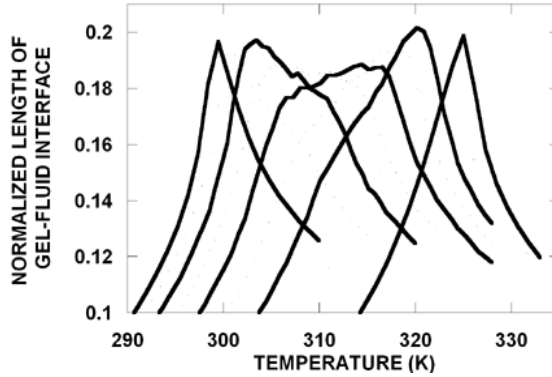


Figure 9. Average Length of The Gel-Fluid Interface. The average normalized length of gel-fluid interface (calculated by Eq.19) is plotted against the temperature. The curves from left to right belong to the following mole fractions: 0.1, 0.3, 0.5, 0.7, 0.9.

What kind of excess permeability curves are predicted by the 'area fluctuation' model? It was found experimentally that excess heat and excess volume are proportional functions in the temperature range of chain melting transition of one and two-component lipid membranes^{61,62}. As a consequence of this proportionality Heimburg [62] pointed out that the fluctuation of the excess heat and the fluctuation of the excess volume are proportional functions too, and postulated a similar proportionality between the fluctuation of the excess heat and the fluctuation of the excess membrane surface area. Thus according to the 'area fluctuation' model the excess permeability, ΔP should be a proportional function of $\Delta C_p RT^2$:

$$\Delta P : \langle (\Delta A - \langle \Delta A \rangle)^2 \rangle : \langle (\Delta V - \langle \Delta V \rangle)^2 \rangle : \langle (\Delta H - \langle \Delta H \rangle)^2 \rangle = \Delta C_p RT^2 \quad (20)$$

The 'phase mismatch' model and the 'area fluctuation' model of excess membrane permeability predict qualitatively different excess permeability curves for certain DMPC/DSPC mixtures. For example in the case of equimolar mixture of DMPC/DSPC the predicted excess permeability curve possesses one and two local maxima according to the 'phase mismatch' and the 'area fluctuation' model, respectively. Which model is

incorrect? An experimental determination of the excess permeability curve of equimolar DMPC/DSPC membrane would answer this question.

2.4. Conclusions

Lateral membrane heterogeneity is related to and affects important membrane functions. In the present chapter a simple two-state model of two-component lipid bilayers (DMPC/DSPC) was utilized to study and demonstrate these structure-function relationships. By using Monte Carlo methods the model simulated the excess heat capacity curves at different DMPC/DSPC mixing ratios in quantitative agreement with the DSC data. The analysis of the calculated membrane energy distribution functions reveals that the gel-fluid transitions of DMPC/DSPC MLV's are continuous transitions and thus in a strict thermodynamic sense one cannot generate a phase diagram of DMPC/DSPC mixture. The 'phase diagram' commonly constructed from the analyses of the excess heat capacity curves cannot be used to estimate the fractional completion of the transition, θ . We demonstrated that the mechanical application of the lever rule for this 'phase diagram' leads to serious errors in the estimation of θ .

The onset of chemical signaling in membranes can be measured by fluorescence recovery after photobleaching (FRAP). Analysing the relationship between the FRAP threshold temperatures and the average membrane configurations at different DMPC/DSPC mixing ratios we found a strong positive correlation between the percolation threshold temperatures of gel clusters and the FRAP threshold temperatures, while the respective correlation was very weak for the percolation threshold temperatures of fluid clusters. At the FRAP threshold temperature the probability of percolation for gel clusters was found to be 0.36 at every mixing ratio.

Formation of lipid microdomains, clusters or 'rafts' in cell membranes have been linked to important cell biological processes such as the trafficking and lateral segregation of proteins involved in cellular signal transduction. Simulating the configurations of DMPC/DSPC bilayers the average size of the gel and fluid microdomains have been determined at different temperatures and mole fractions. Depending on the temperature and mole fraction the average size of the microdomains varies from 1 to 60 lipid molecules. The calculated average cluster sizes are in agreement with neutron diffraction and atomic force microscopy data.

The 'minimal' model of two-component bilayers was used to test the predictions of the existing ideas for excess membrane permeability. The excess membrane permeability for small water soluble molecules in the gel-fluid coexistence region is explained either by the enhanced membrane area fluctuations or by the mismatch at the interface between the gel and fluid regions. By using our simulations we calculated the excess membrane permeability curves predicted by the above mentioned two theories. At certain mole fractions the two theories predicted qualitatively different excess permeability curves.

3. Lipid monolayer structure controls protein adsorption.

Model of Peripheral Protein Adsorption to the Water/Lipid Interface

Two models have been developed to describe the adsorption of a model peripheral protein, colipase, to phospholipid/diacylglycerol (PL/DG) monolayers. One model is applicable at monolayer collapse pressure and at any composition that exceeds the DG mole fraction of PL/DG lateral complexes (Sugár, I. P., N. K. Mizuno, M. M. Momsen, and H. L. Brockman. 2001. Lipid lateral organization in fluid interfaces controls the rate of colipase association. *Biophys. J.* 81:3387–3397.). The other model is applicable at any lateral pressure but only below the mole fraction of DG in the complex (Sugár, I.P., N. K. Mizuno, and H. L. Brockman. 2005. Peripheral protein adsorption to lipid-water interfaces: The free area theory. *Biophys. J.* 89:3997–4005.). Both models assume that initiation of colipase adsorption to the water/lipid interface requires an area of water-exposed hydrophobic surface that exceeds a critical value. In the first model accessible surface is provided by the head groups of the uncomplexed DG molecules. This surface area follows a binomial distribution. In the second model accessible area is created by hydrocarbon chains becoming exposed at the water/lipid interface as total lipid packing density of monolayers of PL and/or PL/DG complexes is decreased. This surface area follows a Poisson distribution. The model described in this chapter is a unification, extension and improvement of these models that is applicable at any lateral pressure and any PL/DG mole fraction. Calculated normalized initial colipase adsorption rates are compared with the available experimental values and predictions of the adsorption rates are made for currently unmeasured compositions and lateral pressure regimes.

3.1. Introduction

Lipid-mediated signaling in cells is part of the chain of events through which chemical information from outside a cell regulates gene expression in the nucleus. An important site along such signaling pathways is the bilayer plasma membrane. The interaction of a soluble ligand with a transmembrane receptor on its exofacial leaflet can cause the metabolism of phospholipids on the cytofacial leaflet to generate lipid second messengers, like diacylglycerols and inositol phosphates¹. These, in turn, trigger the recruitment to the cytofacial leaflet of peripheral proteins, like protein kinases, thereby initiating signaling cascades that ultimately terminate in the nucleus.

Mechanistically, peripheral protein adsorption to a membrane can be mediated by its interaction with specific motifs of membrane-resident proteins² and by electrostatic interactions with the exposed charges of anionic membrane lipids³. Another contributing mechanism, suggested by a growing body of in vitro evidence⁴, is that small clusters of two or more adjacent DG or other non-phospholipid molecules in the membrane can act as an initiation site for the interaction of hydrophobic amino acid side chains of an amphipathic peripheral protein with the interface.

Statistically, in an ideally-mixed PL/DG interface a significant fraction of DG molecules should be clustered, even at a few mole percent of DG. However, physical studies of PL-DG mixing in liquid-expanded monolayers have shown that members of these lipid classes form lateral complexes. Originally described as “compound formation” in fluid monolayers⁵, the term lateral complex better describes the notion of a preferred lateral packing arrangement as opposed to a distinct entity. A similar definition has been used for complexes of phospholipids and cholesterol in more condensed phases⁶. This definition implies that complexes are dynamic, reflecting the average configuration of a surface with essentially unrestricted lateral diffusion. Complex composition is determined from the dependence of mixed monolayer phase transition pressure on lipid composition⁵. Complexes of PL and DG are miscible with excess PL and DG and have DG mole fractions ranging from ~0.1 to 0.4, depending on lipid chain unsaturation of both PL and DG and on PL phosphoryl-X head group (M.M. Momsen and H.L. Brockman, unpublished and Ref. 7.). The observed variation of complex composition within a PL class implies that complex formation does *not* arise from a stoichiometric interaction between the hydroxyl group of glycerol and a given phospholipid head group. Areas of the complexes, expressed per PL molecule, are greater than the collapse area of PL alone and less than the sum of the collapse areas of the PL and its complexed DG.

Initial rates of colipase adsorption to PL/DG monolayers measured at high lipid packing density were negligible if the DG mole fraction was below that of the complex, indicating that a surface comprised of tightly-packed complexes and PL alone prevents colipase adsorption. At higher DG mole fractions the dependence of the initial rate of adsorption on diacylglycerol composition could be described by a statistical model⁷ in which 1) each PL/DG complex is assumed to behave as an excluded area that prevents colipase adsorption, 2) PL/DG complexes mix ideally with binomially-distributed uncomplexed DG and 3) the initiation of colipase adsorption requires a cluster of uncomplexed DG molecules that exceed a critical number. Importantly, analysis of colipase adsorption rate data as a function of lipid composition showed that the excluded complex area determined from the statistical analysis of colipase adsorption kinetics equaled the area of the corresponding PL/DG complex determined from the monolayer physical studies performed in the absence of any protein.

In the studies⁷ on which the above model is based, all measurements of colipase adsorption rates to mixed-lipid monolayers were made in the liquid-expanded (fluid) monolayer state at high lipid packing densities, i.e., close to monolayer collapse. Moreover, the composition-dependence of the surface pressure of monolayers at collapse, as interpreted in light of the two-dimensional phase rule⁸, is the basis for demonstrating the existence of complexes in the absence of colipase. This raised the question of whether PL/DG complexes are a limiting state determined by the mutual fit of differently shaped, weakly interacting molecules confined to a small area or whether they persist at lower lipid densities. To address this we analyzed colipase adsorption rates as a function of lipid packing density in mixed monolayers containing DG at mole fractions less than that found in the complex⁹. We assumed that “free area” was created as lipid packing was

decreased and that if a region of free area exceeded a critical area it could initiate colipase adsorption in the same manner as uncomplexed DG. The difference in the models was that the free area between PL and PL/DG complexes was described by a Poisson distribution rather than the binomial distribution that describes the distribution of uncomplexed DG molecules. Application of this model to colipase adsorption rates to PL and PL/DG monolayers below the DG composition in the complex showed 1) that PL/DG complexes were stable at lipid packing densities below monolayer collapse and 2) that the complex area and critical area yielded by the model agreed, within error, to those obtained at higher DG compositions and high packing density with the binomial model.

Considered together, the results of the previous studies indicate that the common requirement to initiate colipase adsorption is a relatively hydrophobic area of interface that exceeds a critical size, whether it arises from uncomplexed DG or increased spacing of excluding species. In the present chapter a unification and improvement of our previous two models of peripheral protein adsorption on water/lipid interfaces are described. The model is applicable at any lateral pressures and phospholipid-diacylglycerol mixing ratios. After the model description, the calculated normalized initial adsorption rates are compared with the available experimental values and predictions of the adsorption rates are made for currently unmeasured mixing ratio and lateral pressure regimes.

3.2. The Model

3.2.1. Structure of PL/DG monolayers

PL and DG molecules are able to form dynamic complexes⁹, and, thus, each membrane lipid is either part of a PL/DG complex or is uncomplexed. Below X_{cplx} , the DG mole fraction at the complex composition, every DG molecule is part of a PL/DG complex, with uncomplexed PL molecules also present. Above X_{cplx} , however, every PL molecule is part of a PL/DG complex, while additional DG molecules are uncomplexed. As a result of thermal fluctuations a small fraction of uncomplexed PL and DG molecules will be present slightly above and below the complex composition X_{cplx} , respectively. These uncomplexed molecules are neglected in the present model. A list of these and other commonly used symbols can be found in Sec. 3.5. (Appendix 1).

In general one cannot exclude the possibility that more than one type of dynamic complex may form, with complex compositions: $X_{cplx}^1 < X_{cplx}^2 < \dots < X_{cplx}$. In this case if the DG mole fraction, X is $X_{cplx}^j < X < X_{cplx}^{j+1}$ then every DG molecule is part of a PL/DG complex with a complex composition of either X_{cplx}^j or X_{cplx}^{j+1} , i.e. these two types of complexes coexist. If $X < X_{cplx}^1$, uncomplexed PL molecules and complexes with complex composition of X_{cplx}^1 coexist. If $X_{cplx} < X$, uncomplexed DG molecules and complexes with complex composition of X_{cplx} coexist. At the monolayer collapse

pressure, the average molecular area of a complex forming molecule is A_{cplx}^j if the complex composition is X_{cplx}^j .

3.2.2. Free Area and Discrete Molecular Area

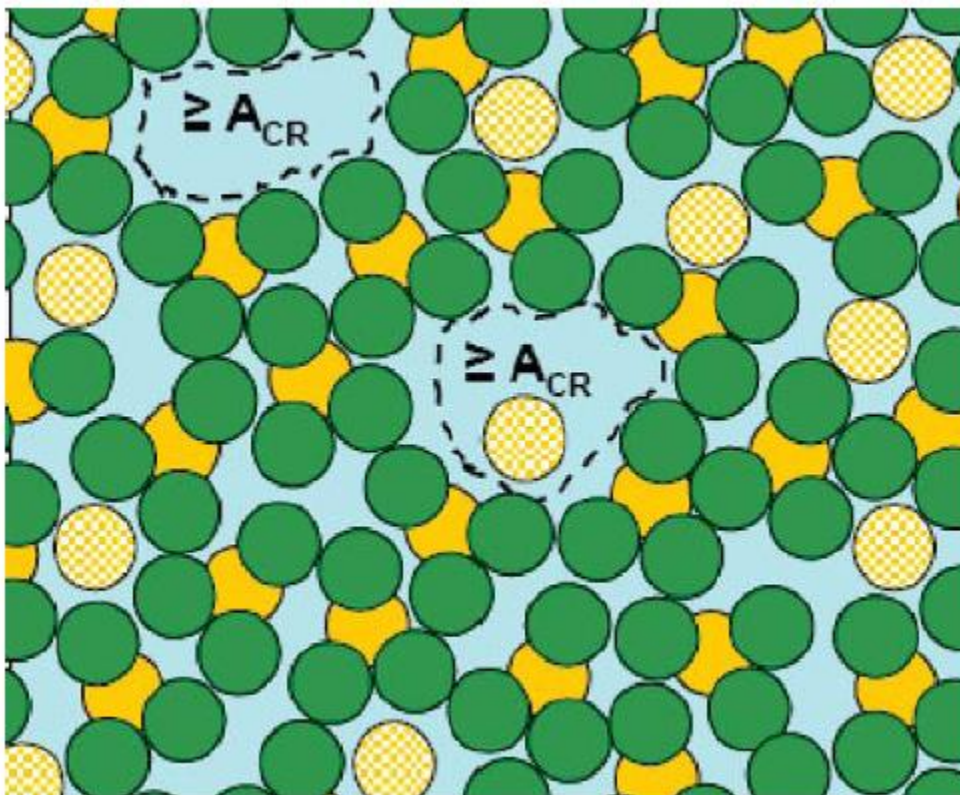


Figure 1. Schematic snapshot of a fluid phospholipid-diacylglycerol monolayer at $X > X_{cplx}$ and surface below collapse, as seen by a protein diffusively approaching from the aqueous phase. The discrete areas of lipid molecules are depicted as colored circles with the continuous blue background between them depicting free area. Complexed phospholipid and diacylglycerol (3:1) are shown in green and orange, respectively, and uncomplexed diacylglycerol is orange-white hatch. Protein adsorption can be initiated at sites in which the sum of blue and orange-white hatched areas exceeds a protein-dependent critical area, A_{CR} . Two such sites are indicated by dashed lines.

Both complexed and uncomplexed lipid molecules are assumed to possess a “discrete molecular area” which is independent of the monolayer surface pressure. The average discrete molecular area of a molecule in a complex is A_{cplx} , whereas the discrete molecular areas of uncomplexed PL and DG are A_{PL} and A_{DG} , respectively. If the area of a monolayer is greater than the sum of the discrete areas of its components, that additional area is termed “free area.” Free area is continually changing and fluctuating

around its average value which decreases with increasing lateral pressure and approaches zero close to the collapse pressure of a lipid monolayer. Free area can be conceptualized as the high energy area between the discrete lipid areas, where lipid hydrocarbon chains are exposed to the water-lipid interface. Both the free area of an interface and the discrete area of DG are potentially able to initiate the productive interaction of a peripheral protein with the interface. Together they constitute the *accessible area* of the interface. In contrast, the discrete areas of PL and PL/DG complexes can not initiate protein adsorption. For adsorption of a protein molecule of cross sectional area A_p to occur, it must diffusively encounter a region of accessible area equal to or larger than a critical area^{4,7,9}, $A_{CR}(\leq A_p)$ (see Fig. 1.)

3.2.3. Characterization of Monolayer Configuration

First, let us assume that only one type of dynamic complex may form, i.e. $X_{cplx}^1 = X_{cplx}$. The actual configuration of the water-lipid interface under a peripheral protein can be characterized by the following two independent variables: f (the total free area) and u (the sum of the discrete areas of the uncomplexed lipid molecules) while the sum of the discrete areas of the complexed lipid molecules, $A_p - f - u$, can be expressed as a function of the independent variables. The possible configurations of the water-lipid interface at $X < X_{cplx}$ and $X > X_{cplx}$ are plotted on Fig. 2a and b, respectively. Thus, in Fig.2a u refers to the discrete area of the uncomplexed phospholipid molecules, while in Fig. 2b u refers to the discrete area of the uncomplexed DG molecules. In both figures the configuration space is constrained by the following inequalities:

$$f + u \leq A_p, u \geq 0 \text{ and } f \geq 0.$$

These constraints define a triangular region in the configuration space that is shaded (either fully or vertically) in Fig. 2a and b. Each point, or its coordinates (u, f) , within this triangle represents a possible monolayer configuration under a peripheral protein. In the case of $X \leq X_{cplx}$ there are no discrete DG areas in the monolayer and protein binding may take place only when $f \geq A_{CR}$. The configurations satisfying this constraint belong to the vertically shaded area in Fig. 2a, while the fully-shaded area belongs to configurations where protein binding cannot take place. In the case of $X > X_{cplx}$ the uncomplexed DG molecules also provide discrete accessible area and allow protein binding provided that $f + u \geq A_{CR}$. The configurations satisfying this constraint belong to the vertically shaded area in Fig. 2b, while the fully-shaded area belongs to configurations where protein binding cannot take place. In the general case when more than one type of dynamic complex may form Figs. 2a and b remain the same but in Fig.2a u is defined differently: it is the sum of the discrete areas of type j complexes if $X_{cplx}^j < X < X_{cplx}^{j+1}$.

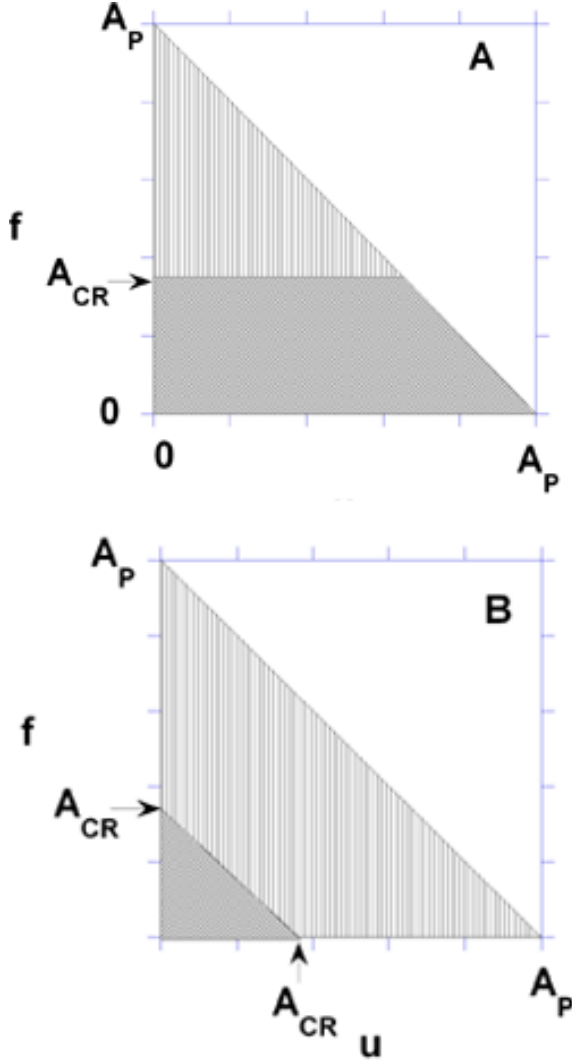


Figure 2. Configuration space of water-lipid interface under a peripheral protein. The configuration of the water-lipid interface under a peripheral protein is characterized by f (the total free area), and u (the total discrete area of the uncomplexed lipid molecules). The configuration space is constrained by the following inequalities: $f + u \leq A_p$, $u \geq 0$ and $f \geq 0$ defining a triangular region in the configuration space that is shaded in Fig. 2a and b. The points within this triangle represent the possible configurations. Vertically shaded and fully-shaded areas represent configurations where protein adsorption can and cannot take place, respectively.

a) $X \leq X_{cplx}$ and b) $X > X_{cplx}$.

3.2.4. The Normalized Initial Adsorption Rate

The measured normalized colipase initial adsorption rate is equal to the adsorption probability, P_{ads} . P_{ads} is the conditional probability that the accessible area under a protein molecule approaching the surface is larger than the critical area, A_{CR} , with the condition that the sum of the free area, f , and the discrete area of the uncomplexed molecules situated under the protein, u , is between 0 and A_p .

$$P_{ads} = \frac{\iint_{all-shaded} p(f, u) df du - \iint_{fully-shaded} p(f, u) df du}{\iint_{all-shaded} p(f, u) df du} \quad (1)$$

where $p(f,u)dfdu$ is the probability that the configuration parameters f and u fall in the intervals $(f,f+df)$ and $(u,u+du)$, respectively. In Eq.1 the numerator is the probability that the configuration parameters, f and u fall into the vertically shaded areas of Figs.2a and b. The denominator is the probability that the configuration parameters fall into the overall shaded areas of Figs.2a and b. Since f and u are statistically independent, the probability density, $p(f,u)$ can be factorized to

$$p(f,u) = p_f \cdot p_u \quad (2)$$

where p_f is the probability density that the free area under the protein is f , and p_u is the probability density that the surface area of uncomplexed molecules under the protein is u .

3.2.5. Probability Density of Free Area Under a Colipase - p_f

The free area at a lipid molecule is fluctuating around a thermodynamic average. According to the thoroughly tested theory of lipid lateral diffusion in one-component lipid bilayers¹⁰⁻¹² and monolayers¹³ the free area per lipid molecule follows a Poisson distribution. Thus, the probability that the free area around a lipid molecule is $(a,a+da)$

$$p_c(a,1)da = [e^{-a/\langle a \rangle} / \langle a \rangle] da \quad (3)$$

where $\langle a \rangle$ is the average free area per molecule.

The probability density that the total free area of n lipid molecules is f (see Appendix 2) is:

$$p_c(f,n) = \frac{1}{\langle a \rangle (n-1)!} \left(\frac{f}{\langle a \rangle} \right)^{n-1} e^{-f/\langle a \rangle} \quad (4)$$

If n is the number of lipid molecules under the protein approaching the monolayer, then it is the following function of f and u

$$n(f,u) = g + h = \frac{u}{A_u} + \frac{A_p - f - u}{A_{cplx}} \quad (5)$$

where the first and second terms are the number of uncomplexed (g) and complexed molecules (h), respectively, and A_u is the discrete area of an uncomplexed molecule. By using Eqs.4, 5 the probability density of finding a free area of f under the protein is

$$p_f = \frac{1}{\langle a \rangle \Gamma[n(f,u)]} \left(\frac{f}{\langle a \rangle} \right)^{n(f,u)-1} e^{-f/\langle a \rangle} \quad (6)$$

where Γ , the continuous version of the factorial function, is utilized because the number of molecules under the protein, $n(f,u)$ is a real number, i.e., there are partially covered lipid molecules under the protein.

In Eq.6 the term $\langle a \rangle$ can be obtained from the measured area per molecule, A_{exp} , because $\langle a \rangle = A_{\text{exp}} - A_{CP}$, where A_{CP} is the average close packed, i.e. discrete, area per molecule (see Appendix 3):

$$A_{CP} = \begin{cases} [A_{PL}(X_{cplx} - X) + A_{cplx}X] / X_{cplx} & X \leq X_{cplx} \\ [A_{DG}(X - X_{cplx}) + A_{cplx}(1 - X)] / (1 - X_{cplx}) & X > X_{cplx} \end{cases} \quad (7)$$

3.2.6. Probability Density of Discrete Area of Uncomplexed Molecules under a Colipase - p_u

Let us assume that under the protein the total number of lipid molecules, n , and the number of uncomplexed lipid molecules, g , are both integer numbers. According to the binomial distribution the probability of this event is

$$\binom{n}{g} [q]^g [1 - q]^{n-g} \quad (8)$$

where q is the probability that a randomly picked molecule of the monolayer is uncomplexed (see Appendix 3):

$$q = \begin{cases} \{1 + [A_{cplx}X] / [A_{PL}(X_{cplx} - X)]\}^{-1} & X \leq X_{cplx} \\ \{1 + [A_{cplx}(1 - X)] / [A_{DG}(X - X_{cplx})]\}^{-1} & X > X_{cplx} \end{cases} \quad (9)$$

However when n and g are real numbers we have to use the continuous version of the cumulative binomial distribution, the so-called *incomplete beta function*, $I_q(x, y)$. This special function is defined and discussed in Appendix 4. Thus, the probability density that g out of the n molecules under the protein are uncomplexed is:

$$p_u(f, u) = \left[\frac{\partial I_q}{\partial y} \Big|_{y=n(f,u)-g(u)+1} - \frac{\partial I_q}{\partial x} \Big|_{x=g(u)} \right] \frac{1}{A_u} \quad (10)$$

3.2.7. Numerical integration

The double integrals defined in Eq.1 are calculated numerically by using the repeated one-dimensional integration approach. Along each dimension we use the method of Gaussian Quadrature¹⁴.

3.3. Results and Discussion

3.3.1. Protein Adsorption to POPC Monolayers

In Fig. 3 squares mark the normalized initial adsorption rates of colipase measured at different specific areas for one component 1-palmitoyl-2-oleoyl-*sn*-glycero-3-phosphocholine (POPC) monolayers⁹. Normalization was accomplished by dividing the measured rates by the highest value measured. The data are qualitatively of sigmoid shape. The initial adsorption rates can be calculated by means of our above described model. With pure POPC $X = 0 < X_{cplx}$, $q = 1$ and $p_u = \delta(A_p - f - u)$ (see Eq.38 in Appendix 4). Thus Eq.1 can be simplified as follows:

$$P_{ads} = \frac{\int_0^{A_p} \int_0^{A_p-f} p_f \cdot \delta(A_p - f - u) du df - \int_0^{A_{CR}} \int_0^{A_p-f} p_f \cdot \delta(A_p - f - u) du df}{\int_0^{A_p} \int_0^{A_p-f} p_f \cdot \delta(A_p - f - u) du df} = \frac{\int_0^{A_p} p_f(f, A_p - f) df}{\int_0^{A_{CR}} p_f(f, A_p - f) df} \quad (11)$$

where $p_f(f, A_p - f)$ is given by Eq. 6 with $u = A_p - f$ and the monolayer surface area occupied by a fully adsorbed colipase molecule¹⁵ is $A_p = 500 \text{ \AA}^2$. Calculated values were obtained by fitting Eq.11 to the experimental points and these are connected by solid line segments in Fig. 3. Because Eq. 11 is equivalent to Eq. 6 of Ref. 9 and the same data were analyzed, Fig. 3 is reprinted from the reference. There is a good agreement between the measured and calculated values. The values of the model parameters, A_{PL} and A_{CR} , obtained from the fitting procedure are $A_{PL} = 58.3 \text{ \AA}^2$ and $A_{CR} = 84.8 \text{ \AA}^2$, respectively, and the sum of the squares of the deviations between measured and calculated rates is 0.066.

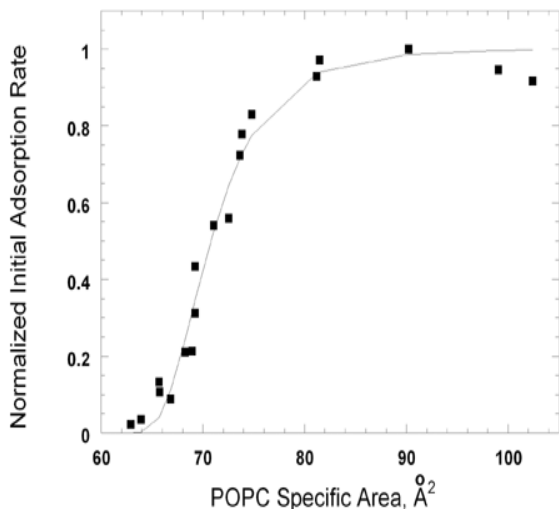


Figure 3. Colipase adsorption to one-component phospholipid (POPC) monolayers. The normalized initial adsorption rate of colipase is plotted against the specific area of POPC molecules forming a monolayer at the water/air interface. (Solid squares show experimental data⁹; line segments join fitted values determined by using Eq.11 and $A_{PL} = 58.3 \text{ \AA}^2$, $A_{CR} = 84.8 \text{ \AA}^2$). Reprinted from Ref. 9.

3.3.2. Protein Adsorption to DO/POPC Monolayers

Colipase adsorption to lipid monolayers was also analyzed using data⁹ obtained using two-component DO/POPC monolayers, where DO is 1,2-dioleoyl-*sn*-glycerol. In Fig. 4a, the measured normalized initial adsorption rates are plotted against the DO mole fraction, X . Adsorption rates obtained at different lateral pressures are marked by different symbols. The figure shows that the adsorption rate tends to increase with increasing DO mole fraction and/or decreasing lateral pressure. The area per lipid molecule corresponding to each point shown in Fig. 4a is known from the experimental surface pressure–area isotherms measured independently for each lipid composition (see Fig.4 in Ref. 9). Also, for any composition at an experimental surface pressure, the molecular area can be calculated by polynomial interpolation as previously described (see Table 1 in Ref. 9).

When fitting Eq.1 to the data in Fig. 4a, we take $A_{CR} = 84.8 \text{ \AA}^2$, the value obtained for one-component POPC monolayers. In so doing we assume that A_{CR} is independent of the DO mole fraction. This assumption is based on our observation that the maximal adsorption rate to the accessible area of a phospholipid monolayer equals the adsorption rate to a tightly-packed pure DO monolayer (see Fig. 2 in Ref. 7). The DO mole fraction of the complex is $X_{cplx}^1 = 0.3$, as determined⁷ from the partial phase diagram constructed from surface pressure–area isotherms for DO/POPC. Thus in the range from 0 to 0.3 DO mole fraction, the only unknown model parameter is A_{cplx}^1 , the molecular area of the complex close to the collapse pressure. By assuming the same complex structure at every experimental lateral pressure, i.e, assuming a surface pressure independent value of A_{cplx}^1 , the global fit of our model to every experimental data resulted in $A_{cplx}^1 = 49.5 \text{ \AA}^2$. This assumption is supported by our previous results (see Fig. 5 in Ref. 9). Thus according to Eq.7 the average close packed area per molecule, A_{CP} , linearly decreases from $A_{PL} = 58.3 \text{ \AA}^2$ to $A_{cplx}^1 = 49.5 \text{ \AA}^2$ while the DO mole fraction increases from 0 to 0.3. In

Fig. 4a from 0 to 0.3 DO mole fractions the calculated results are represented by continuous lines, and there is a good agreement between the experimental and calculated values.

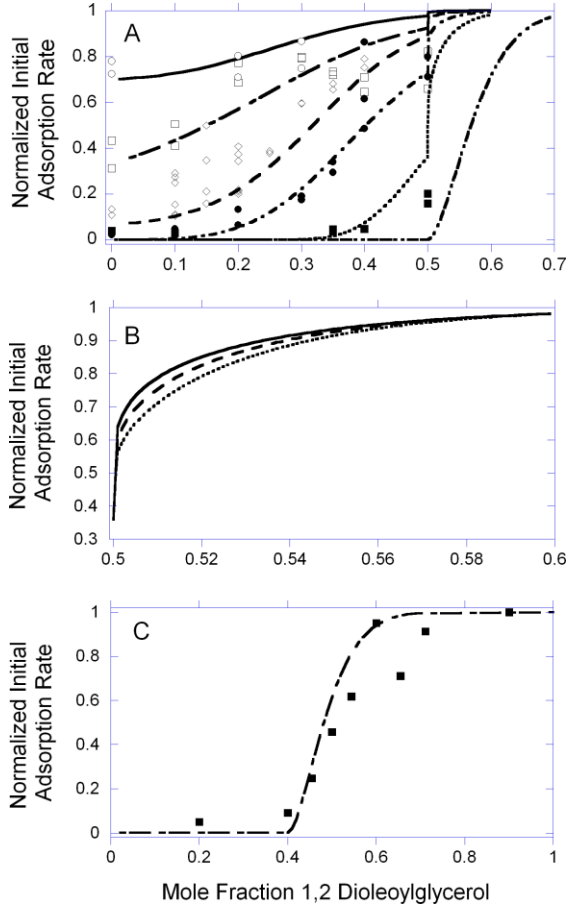


Figure 4. Colipase adsorption to two-component phospholipid (POPC/DO) monolayers. a) The normalized initial adsorption rates of colipase obtained at initial surface pressures of 15 (open circle), 20 (open square), 25 (open diamond), 30 (solid circle), and 40 (solid square) mN/m

The DO mole fraction in the complex, $X_{cplx}^1 = 0.3$, should be less than X_{cplx} , because we do not measure a sudden increase in the protein adsorption until X reaches 0.5. A sudden increase is expected at X_{cplx} because uncomplexed DG areas begin to appear at this mole fraction. Mathematically the discontinuity at X_{cplx} is the consequence of the sudden decrease in the fully-shaded area of integration in Eq.1^{**}. In order to calculate the

are plotted against the DO mole fraction. The experimental data were taken from Ref. 9. Continuous fit lines through data obtained at 15 (solid), 20 (long-short dashed), 25 (dashed), 30 (dash-dotted), and 40 (dotted) mN/m were calculated by using Eq.1 and model parameter values of $A_{PL} = 58.3 \text{ \AA}^2$, $A_{CR} = 84.8 \text{ \AA}^2$, $A_{DO} = 45 \text{ \AA}^2$, $A_{cplx}^1 = 49.5 \text{ \AA}^2$ at $0 \leq X < X_{cplx}^1 = 0.3$, and $A_{cplx} = 45 \text{ \AA}^2$ at $X_{cplx}^1 \leq X < X_{cplx} = 0.5$. The doubly dash-dotted line was calculated for the case of collapse pressure by using Eq.14 and the same model parameter values. b) Normalized initial adsorption rate curves calculated by using Eq.1 at the same lateral pressure, 40mN/m, and above the complex composition, $X > X_{cplx}$. The calculations were performed at three different A_{DO} values: 55 \AA^2 (solid), 45 \AA^2 (dashed), 35 \AA^2 (dotted), while the other model parameters are given in the legend to Fig. 4a. c) Colipase adsorption to SOPC/DO monolayers at collapse pressure. Solid squares show experimental data⁷. Long-short dashed line represents data calculated by using Eq.14. Model parameters are given in the legend to Fig.4a, except $X_{cplx} = 0.4$

^{**} Chemically, the discontinuity appears at X_{cplx} because the reaction of complex formation is assumed to go to 100% completion.

adsorption rates in the range of DO mole fractions from 0.3 to 0.5, we assume that A_{CP} keeps decreasing in this range at a similar rate and we also assume that $X_{cplx} = 0.5$. With these assumptions we get $A_{cplx} = 45 \text{ \AA}^2$ at $X_{cplx} = 0.5$. The respective calculated curves in Fig. 4a show satisfactory agreement with the rather limited experimental data in this compositional range.

In the range of 0.5 - 1.0 DO mole fraction no experimental initial adsorption rate data are available. However, the specific area was measured at different lateral pressures for the pure DO monolayer. Since the specific area at $X = X_{cplx}$ and at surface pressures below collapse is roughly equal to the corresponding specific area of pure DO⁹ we assume that $A_{cplx} = A_{DO} (= 45 \text{ \AA}^2)$. Interestingly, this area of DO compares well with the reported hard cylinder area of DO = 44.7 \AA^2 , determined by mathematical extrapolation of its surface pressure-molecular area isotherm to infinite surface pressure, where it is maximally dehydrated¹⁶. This suggests that when the average molecular area is most condensed in monolayers at finite pressures, relative to the sum of constituent lipid areas, DO is highly shielded from water. Using 45 \AA^2 for A_{DO} , we calculated the initial adsorption rates from $X = 0.5$ to 1. The calculated initial adsorption rates sharply increase at $X = X_{cplx}$ because uncomplexed DO molecules are present above this mole fraction. The increase at $X = X_{cplx}$ becomes sharper with increasing values of A_{DO} (see Fig. 4b).

3.3.3. Protein Adsorption to DO/POPC Monolayers at Collapse Pressure

Close to the collapse pressure the free area in the monolayer is close to zero, i.e., $\langle a \rangle / A_{CP} \approx 0$. Thus the protein adsorption rate is non-zero only above X_{cplx} , i.e., when uncomplexed DG areas are present. Calculating the normalized adsorption rates at $X > X_{cplx}$, $p_f = \delta(f)$ (see Eq.22 in Appendix 2) is substituted into Eq.1 and we get

$$P_{ads} = \frac{\int_0^{A_p} \int_0^{A_p-u} p_u(f, u) \delta(f) df du - \int_0^{A_{CR}} \int_0^{A_{CR}-u} p_u(f, u) \delta(f) df du}{\int_0^{A_p} \int_0^{A_p-u} p_u(f, u) \delta(f) df du} = \frac{\int_0^{A_p} p_u(0, u) du}{\int_0^{A_{CR}} p_u(0, u) du} \quad (12)$$

where $p_u(0, u)$ is given by Eq.10. Eq.12 is even simpler when $A_{cplx} = A_{DO}$. In this case the number of molecules under the colipase, n is independent of u , and from Eq.34 (Appendix 4)

$$p_u(0, u) du = p_u(0, g) dg = -dl_q(g, n - g + 1). \quad (13)$$

Thus the adsorption rate can be calculated by the following equation

$$P_{abs} = \frac{\int_0^{n+1} dI_q(g, n-g+1)}{\int_0^{n+1} dI_q(g, n-g+1)} = \frac{I_q(A_{CR}/A_{DO}, n - A_{CR}/A_{DO} + 1) - I_q(n+1, 0)}{I_q(0, n+1) - I_q(n+1, 0)} = I_q(A_{CR}/A_{DO}, n - A_{CR}/A_{DO} + 1) \quad (14)$$

where $I_q(0, n+1) = 1$ and $I_q(n+1, 0) = 0$ (see Eqs.40,41 in Appendix 4) and when n and A_{CR}/A_{DO} are integers we get

$$P_{abs} = I_q(A_{CR}/A_{DO}, n - A_{CR}/A_{DO} + 1) = \sum_{i=A_{CR}/A_{DO}}^n \binom{n}{i} q^i (1-q)^{n-i}.$$

This last equation is equivalent to Eq.1 in Ref. 7. By using Eq.14 and the same model parameter values as in Fig. 4a, we calculated the initial adsorption rate near the collapse pressure (see doubly dash-dotted line in Fig. 4a). There are no experimental adsorption rate data for DO/POPC monolayer at collapse, but data are available for DO/SOPC (see squares in Fig. 4c) where SOPC differs from POPC only in having 2 additional carbons in the $sn-1$ acyl chain. In Fig. 4c the solid line was calculated by using Eq.14 and the same model parameter values as in Fig. 4a except $X_{cplx} = 0.4$ was chosen.

One can characterize the generality of the different models – the models previously described^{7,9} and the present model – by comparing the range of the configuration space (u, f) involved. In the case of the model at collapse pressure⁷ the integration takes place only along the horizontal side of the triangle in Fig. 2b. In the case of the model at any lateral pressure but below the complex composition⁹ the integration takes place only along the hypotenuse of the triangle in Fig. 2a. In the case of the unified model we integrate on the entire triangular shaded area in Figs.2a and b.

The experimental data used to test the unified model was obtained using lipid monolayers in which the area fraction of both free area and discrete DG area could be experimentally controlled. Both types of adsorption-promoting interface are found in biological surfaces. Despite the average close packing of phospholipids in cell membranes, free area appears when the bilayer structure of the matrix lipid is forced to change. Examples of this are cell-cell fusion and cell transfection by foreign genes. In these cases pores and/or cracks form in the membrane and free area appears at the highly curved pore and/or crack edges¹⁷. Secondly, even planar bilayers, such as DPPC large unilamellar vesicles, go through sharp, pressure or temperature-induced, gel-to-fluid transitions. During the transition there are large lateral density fluctuations in the lipid bilayer, resulting in the appearance of free area and increased ion permeability¹⁸ and phospholipase activity¹⁹. The model should be also applicable for understanding peripheral protein adsorption to emulsion particles, e.g. lipoproteins, where free area, as

indicated by effective surface pressure²⁰, is more abundant than in planar bilayer membranes. Lipoproteins and dietary lipid emulsions with cores of triacylglycerol are also sites of lipolysis which generates large quantities of DG, monoacylglycerols and fatty acids, all of which form complexes with phospholipids⁷. Interestingly, the initiation of emulsion lipolysis is typically a lag-burst phenomenon²¹ which now can be understood as a shift from a lipase adsorption rate being limited by the availability of free area to adsorption rate becoming (un)regulated by the presence of uncomplexed lipolysis products like DG.

3.4. Conclusions

A statistical physical model is developed and used to describe the rate determining step of protein adsorption from the aqueous phase to lipid interfaces. The model assumes that the amphipathic peripheral protein, colipase, adsorbs to water/lipid interface where the accessible surface area is larger than a critical value. Accessible surface is provided either by the discrete areas of uncomplexed DG molecules or by the free area between lipid molecules. The model described in this chapter is a unification and extension of two previously developed models – describing adsorption to monolayers a) at collapse and at any PL/DG mole fraction and b) below the complex composition and at any lateral pressure – and is applicable at any lateral pressure and PL/DG mole fraction. In addition, it incorporates an expression for the continuous binomial distribution to describe discrete DG area rather than requiring integer steps in calculating the number of DG molecules in a cluster. Calculated normalized initial adsorption rates are compared with the available experimental values, and predictions of the adsorption rates are made for currently unmeasured mixing ratio and lateral pressure regimes. The testing of the model is currently limited by the compositional range and scatter of the experimental data available. However, recent advances in the instrumentation for more accurately and conveniently measuring initial adsorption rates of colipase²² should allow more rigorous testing. In particular, it will be of interest to better determine the extent to which complexes may form at DG mole fractions above that which is indicated by monolayer physical studies.

3.5. Appendix 1

Definitions of frequently used symbols

X , DG mole fraction

X_{cplx} , DG mole fraction in a DG/PL complex

A_{cplx} , average discrete molecular area of molecules in a complex

X_{cplx}^j , DG mole fraction in a type j complex

A_{cplx}^j , discrete average molecular area of molecules in a type j complex

A_{PL} , discrete molecular area of an un-complexed PL molecule

- A_{DG} , discrete molecular area of an un-complexed DG molecule
 A_u , discrete molecular area of an un-complexed molecule
 A_p , cross sectional area of a peripheral protein
 A_{CP} , average discrete area per molecule
 A_{CR} , the minimum accessible area required to initiate protein adsorption
 A_{exp} , the experimental average area per molecule (or specific area)
 u , total discrete area of uncomplexed lipid molecules under a peripheral protein
 f , total continuous free area under a peripheral protein
 a , continuous free area of lipid molecule
 n , number of lipid molecules under a peripheral protein
 g , number of uncomplexed lipid molecules under a peripheral protein
 h , number of complexed lipid molecules under a peripheral protein
 P_{ads} , adsorption probability of peripheral protein to a monolayer

3.6. Appendix 2

The probability density that the free area of n lipid molecules is f .

Let us consider n lipid molecules of the monolayer. The free area of the n molecules fall into the following intervals: $(a_1, a_1 + da_1)$, $(a_2, a_2 + da_2)$, ..., $(a_n, a_n + da_n)$.

The probability that the free area of the i -th molecule falls into the interval $(a_i, a_i + da_i)$ is:

$$p_c(a_i, 1) da_i = [e^{-a_i / \langle a \rangle} / \langle a \rangle] da_i \quad (15)$$

The probability density that the total free area of the considered n molecules is

$f(= \sum_{i=1}^n a_i)$ can be obtained from the following multiple convolution²³:

$$p_c(f, n) = p_c(a_1, 1) * p_c(a_2, 1) * \dots * p_c(a_n, 1) \quad (16)$$

In order to calculate the multiple convolution one has to multiply the generating functions of the individual distributions:

$$L_p(s, n) = [L_p(s, 1)]^n \quad (17)$$

where

$$L_p(s, 1) = \int_0^{\infty} e^{-sa} p_c(a, 1) da = \int_0^{\infty} e^{-sa} [v e^{-av}] da = \frac{v}{s + v} \quad (18)$$

where $v = \frac{1}{\langle a \rangle}$.

The inverse of the generating function $L_p(s, n)$ results in the probability density that the total free area of the considered n molecules is f :

$$p_c(f, n) = e^{-vf} v \frac{(vf)^{n-1}}{(n-1)!} = e^{-f/\langle a \rangle} \frac{(f/\langle a \rangle)^{n-1}}{\langle a \rangle (n-1)!} \quad (19)$$

Let us calculate the probability density, $p_c(f, n)$ when $\langle a \rangle \rightarrow 0$. In this limiting case the generating function of an individual distribution $p_c(a, 1)$ is:

$$L_p(s, 1) |_{v \rightarrow \infty} = \left[\frac{v}{s+v} \right]_{v \rightarrow \infty} = 1 \quad (20)$$

and

$$L_p(s, n) |_{v \rightarrow \infty} = \left[\frac{v}{s+v} \right]_{v \rightarrow \infty}^n = 1^n = 1 \quad (21)$$

The inverse of the generating function $L_p(s, n) |_{v \rightarrow \infty}$ results in

$$p_c(f, n) |_{\langle a \rangle \rightarrow 0} = \delta(f) \quad (22)$$

where $\delta(f)$ is the delta function.

3.7. Appendix 3

Calculation of A_{CP} and q

Let us assume that the DG mole fraction, X , is above the complex mole fraction, X_{cplx} .

The total number of molecules in the monolayer, N is the sum of the DG and PL molecules:

$$N = N_{DG} + N_{PL} = N_{DG}^u + N_{DG}^c + N_{PL} \quad (23)$$

where N_{DG}^u and N_{DG}^c is the number of uncomplexed and complexed DG molecules, respectively. The complex mole fraction is:

$$X_{cplx} = \frac{N_{DG}^c}{N_{DG}^c + N_{PL}} \quad (24)$$

After substituting N_{PL} from Eq.24 into Eq.23 we get

$$N_{DG} + N_{PL} = N_{DG}^u + N_{DG}^c / X_{cplx} = N_{DG} - N_{DG}^c + N_{DG}^c / X_{cplx}. \quad (25)$$

After eliminating N_{DG} we get

$$\frac{N_{PL}}{N} = 1 - X = \frac{N_{DG}^c}{NX_{cplx}} (1 - X_{cplx}) \quad (26)$$

and thus the fraction of molecules that are part of a complex is

$$\frac{N_{DG}^c + N_{PL}}{N} = \frac{N_{DG}^c}{NX_{cplx}} = \frac{1 - X}{1 - X_{cplx}}. \quad (27)$$

The surface area per molecule at the discrete area is

$$A_{CP} = \frac{N_{DG}^u A_{DG} + (N_{DG}^c + N_{PL}) A_{cplx}}{N} = \left(\frac{X - X_{cplx}}{1 - X_{cplx}} \right) A_{DG} + \left(\frac{1 - X}{1 - X_{cplx}} \right) A_{cplx} \quad (28)$$

and if the free area is disregarded, the probability of picking an uncomplexed DG from the N lipid molecules is

$$q = \frac{N_{DG}^u A_{DG}}{NA_{CP}} = \left(1 + \frac{(1 - X) A_{cplx}}{(X - X_{cplx}) A_{DG}} \right)^{-1}. \quad (29)$$

In the case of $X \leq X_{cplx}$, as a result of a similar derivation, we get

$$A_{CP} = \frac{N_{PL}^u A_{PL} + (N_{PL}^c + N_{DG}) A_{cplx}}{N} = \left(\frac{X_{cplx} - X}{X_{cplx}} \right) A_{PL} + \left(\frac{X}{X_{cplx}} \right) A_{cplx} \quad (30)$$

$$q = \frac{N_{PL}^u A_{PL}}{NA_{CP}} = \left(1 + \frac{XA_{cplx}}{(X_{cplx} - X) A_{PL}} \right)^{-1} \quad (31)$$

3.8. Appendix 4

3.8.1. Incomplete beta function and the binomial distribution

The incomplete beta function is defined by the following integral²⁴:

$$I_q(x, y) = \frac{\int_0^q t^{x-1} (1-t)^{y-1} dt}{\int_0^1 t^{x-1} (1-t)^{y-1} dt} \quad \text{where } (x, y > 0) \quad (32)$$

This special function provides a continuous version of the binomial distribution. It can be shown²⁴ that in the case of integer g and n (where $g \leq n$)

$$I_q(g, n-g+1) = \sum_{i=g}^n \binom{n}{i} \cdot [q]^i \cdot [1-q]^{n-i} = 1 - \sum_{i=0}^{g-1} \binom{n}{i} \cdot [q]^i \cdot [1-q]^{n-i} \quad (33)$$

i.e., at integer values of the independent variables the incomplete beta function is equal with 1 minus the cumulative binomial distribution. Since $I_q(g, n-g+1)$ is a continuous function of the variables, n and g it can be considered as a continuous version of 1 minus the cumulative binomial distribution.

The incomplete beta function describes the binomial distribution as follows

$$\binom{n}{g} \cdot [q]^g \cdot [1-q]^{n-g} = I_q(g, n-g+1) - I_q(g+1, n-g) = \int_g^{g+1} \left[-\frac{dI_q}{dg} \right] dg' \quad (34)$$

where the integrand can be considered as the probability density of the binomial distribution. Thus, the probability of finding $(g, g+dg)$ uncomplexed molecules (of surface area $u (= g \cdot A_u)$) out of n molecules situating under the protein is

$$p_u(n, g) dg = -\frac{dI_q}{dg} dg = -\left[\frac{\partial I_q(x, y)}{\partial x} \Big|_{x=g} \cdot \frac{dx}{dg} + \frac{\partial I_q(x, y)}{\partial y} \Big|_{y=n-g+1} \cdot \frac{dy}{dg} \right] dg = \left[\frac{\partial I_q}{\partial y} \Big|_{y=n-g+1} - \frac{\partial I_q}{\partial x} \Big|_{x=g} \right] dg \quad (35)$$

or

$$p_u(f, u) du = -\frac{dI_q}{dg} \frac{du}{A_u} = -\left[\frac{\partial I_q(x, y)}{\partial x} \Big|_{x=g(u)} \cdot \frac{dx}{dg} + \frac{\partial I_q(x, y)}{\partial y} \Big|_{y=n(f, u)-g(u)+1} \cdot \frac{dy}{dg} \right] dg = \left[\frac{\partial I_q}{\partial y} \Big|_{y=n(f, u)-g(u)+1} - \frac{\partial I_q}{\partial x} \Big|_{x=g(u)} \right] \frac{du}{A_u} \quad (36)$$

The partial derivatives of the incomplete beta function $\frac{\partial I_q(x, y)}{\partial x}$ and $\frac{\partial I_q(x, y)}{\partial y}$ are calculated by a FORTRAN program kindly provided by Dr. Boik²⁵.

3.8.2. Extensions of the incomplete beta function

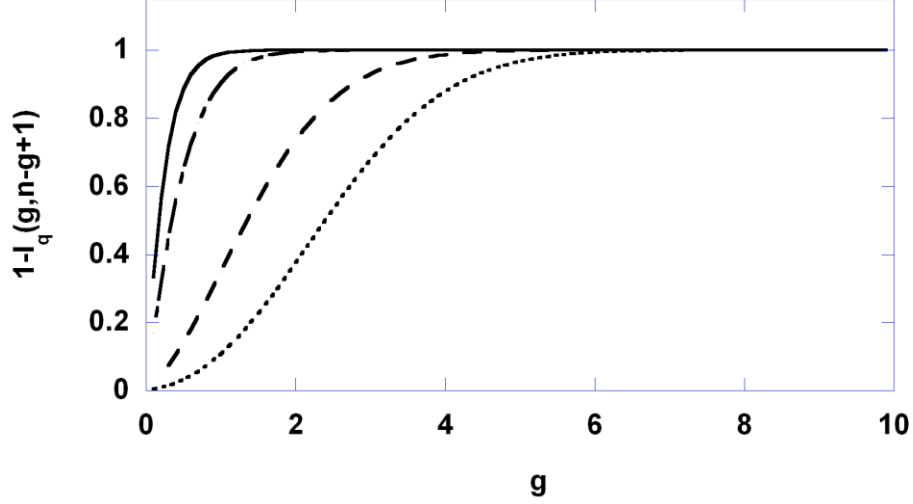


Figure 5. *Incomplete beta function*

The incomplete beta function, $1 - I_q(g, n - g + 1)$, is plotted against g at $n=10$ and at the following values of q : 0.001 (solid), 0.01 (short-long dashed), 0.1 (dashed), 0.2 (dotted).

Fig.5 shows $1 - I_q(g, n - g + 1)$ as a function of g at different values of q . When q approaches zero the initial slope of the function increases, and the initial slope becomes infinite at $q=0$, i.e., $1 - I_0(g, n - g + 1)$ approaches the unit step function. Thus the derivative of the incomplete beta function at $q=0$ can be approximated by a negative delta function:

$$\frac{dI_0(g, n - g + 1)}{dg} \approx -\delta(g). \quad (37)$$

However, when q approaches 1, $1 - I_1(g, n - g + 1)$ becomes close to zero everywhere except close to $g=n+1$ it sharply increases to 1, i.e., $1 - I_1(g, n - g + 1)$ approaches the unit step function. Thus the derivative of the incomplete beta function at $q=1$ can be approximated by a negative delta function:

$$\frac{dI_1(g, n - g + 1)}{dg} \approx -\delta(n + 1 - g). \quad (38)$$

One can extend the validity of the incomplete beta function to $g=0$. As we mentioned before in the case of integer g and n

$$I_q(g, n-g+1) = \sum_{i=g}^n \binom{n}{i} \cdot [q]^i \cdot [1-q]^{n-i} \quad (39)$$

if $g=0$ then the right hand side of the above equation will be

$$\sum_{i=0}^n \binom{n}{i} \cdot [q]^i \cdot [1-q]^{n-i} = (1-q+q)^n = 1 \equiv I_q(0, n+1) \quad (40)$$

This extension is valid for any value of q and n . By using Eq.40 and the symmetry relation of the incomplete beta function²⁴

$$1 \equiv I_q(0, n+1) = 1 - I_{1-q}(n+1, 0) ,$$

we get for any value of q and n

$$I_{1-q}(n+1, 0) = 0 . \quad (41)$$

4. Membrane geometry regulates intercellular communication.

Model of Autocrine/Paracrine Signaling in Epithelial Layer.

An autocrine/paracrine signaling model in epithelial layers is described. The axially symmetric model of the epithelial layer explicitly considers the microvilli of the epithelial cells and the gaps between nearest neighbor microvilli. Trapping site distribution functions and probability of autocrine signaling are calculated for different epithelial geometries and ligand sources by solving numerically the inhomogeneous stationary diffusion equation, the *Poisson equation*. In general the global characteristics of the trapping site distribution curves are similar to the ones obtained for a planar epithelial model, while the superimposed small periodical changes of the curves reflect the details of the epithelial geometry. However, when ligands are emitted into a narrow gap between nearest neighbor microvilli the probability of local trapping is particularly high, causing locally a large deviation from the overall behavior of the trapping site distribution curves.

If the microvilli of the cell are closely packed, the probability of paracrine signaling is about 0.2. However, this probability jumps to about 0.5 if the cell is able to slightly loosen the tight packing, e.g. by decreasing the diameter of the microvilli by only 2%. On the basis of our calculations alteration of microvillus geometry represents a mechanism by which epithelial cells can efficiently regulate intercellular signaling.

4.1. Introduction

Autocrine and paracrine signaling are common physiological as well as pathological mechanisms that regulate cellular behavior. By releasing and then adsorbing the same ligand the cell is able to test its own surroundings. Interruption of autocrine ligand binding should reflect the presence of extracellular components that are able to interact with the ligand. Autocrine loops were experimentally studied in cell cultures¹⁻⁵. In these experiments either adherent cells are distributed in two dimensions and secreted ligands are diffusing in the adjacent layer of culture medium^{6,7} or cells are suspended in a three-dimensional medium⁸⁻¹².

In the case of epithelial layers, cells are tightly packed to each other and secreted ligands diffuse in the extracellular space between the epithelium and an adjacent surface. For example, in *Drosophila* egg development, ligands of the epidermal growth factor receptor (EGF receptor) diffuse in a thin gap between the follicular epithelium and the oocyte surface^{13,14}. Ligand receptors are uniformly distributed on the surface of the follicle cells and are absent on the surface of the oocyte.

In 2004 Berezhkovskii et al.¹⁵ developed a stochastic model of receptor mediated ligand trapping in epithelial layers. The epithelial layer was modeled by a flat surface that partially adsorbs ligands. The ligand, emitted at a certain point of the epithelial layer, diffuses within the thin adjacent fluid layer until it is adsorbed by the epithelial layer. Berezhkovskii et al.¹⁵ derived *an analytical expression* for the spatial distribution of the trapping points.

Motivated by the work of Berezhkovskii et al.¹⁵ we have developed a more realistic model that explicitly considers the microvilli of the epithelial layer. It was our initial thought that the detailed geometry and the location of the ligand source significantly affect the trapping site distribution and the probability of autocrine signaling. Microvilli are finger-like projections of cytoplasm that increase surface area of the cell. Microvilli are present on the apical surface of the epithelial layer. The electron microscopy of intestinal, alveolar and gastric parietal cells revealed that the typical height and diameter of a microvillus is 0.5-1.5 μm and 0.1-0.2 μm , respectively¹⁶⁻¹⁸. The number of microvilli per cell depends on the type of the epithelial layer. In the case of alveolar cells about 120-140 microvilli were found per cell¹⁷. However, we should note that the epithelium changes markedly in structure from the main bronchi to the alveolar epithelium¹⁹. Though microvilli are cellular extensions, there are little or no cellular organelles present in them. Each microvillus has a dense bundle of cross-linked actin filaments, which serves as its structural core. For example in the microvillus of intestinal epithelium the plus ends of the actin filaments are located at the tip of the microvillus and are capped, possibly by capZ proteins²⁰, while the minus ends are anchored in the ‘terminal web’ composed of a complicated set of proteins including spectrin and myosin II. The actin filaments are thought to determine the geometry of the microvilli. As a consequence of the tight packing of the epithelial cells ligands secreted from the apical surface should be trapped by receptors on the apical surface, while on the other hand ligands secreted by the basolateral membrane should be trapped by receptors on the basolateral membrane. In this work we focus on ligands secreted and trapped by the apical surface of the epithelium.

In the Model section of this chapter we describe our axially symmetric epithelial model and the numerical integration of the respective diffusion equation utilized. In the Results and Discussion section the calculated trapping site distributions obtained at different epithelial geometries and ligand sources are shown. The similarities and differences between the results of the planar and axially symmetric models are discussed in depth.

4.2. Model

4.2.1. Model Geometry

When developing a more realistic model of the epithelial layer, which takes into account its rough surface due to the presence of microvilli, one is forced to give up finding an analytical solution and instead to numerically solve the respective diffusion equation. Rather than solving the most general case, we consider a situation with axial symmetry, which will be sufficient for highlighting the role of surface roughness in epithelial cell

signaling. We thus model the surface of the epithelial layer by concentric cylinders shown in Fig.1.

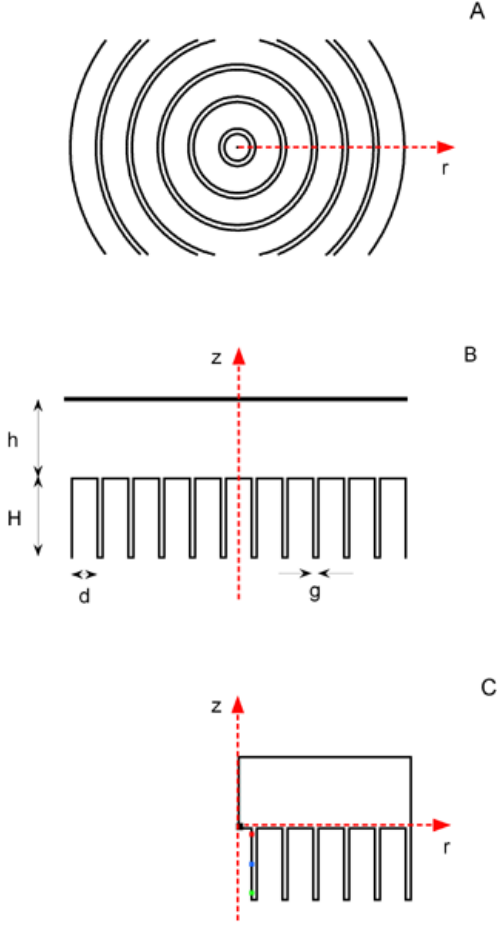


Figure 1. *The model of an epithelial layer.* The microvilli of the epithelial layer are modeled by concentric cylinders. a) top view of the model, b) vertical-cross section across the central microvillus, c) the finite computational domain of the model is enclosed by a solid line. The locations of ligand emission are marked by black square (cylindrical source) on the top of the central microvillus and by red, blue and green squares (ring-like sources) at different heights around the central microvillus.

Coordinate axes, r and z are marked by dashed lines. H and d are the height and diameter of a microvillus, respectively, while g is the gap-width between nearest neighbor rings of microvilli. Above the epithelial cells there is a fluid layer of thickness h . The top of the fluid layer is a reflective boundary. The emitted ligand is diffusing between the rugged, partially absorbing surface of the epithelial cells and the planar, reflective boundary.

The central cylinder represents a microvillus emitting the ligands. This microvillus is surrounded by concentric rings of fused microvilli. The number of microvilli in a ring, \tilde{n} is proportional to the radius of the ring, r and inversely proportional to the diameter of a microvillus, d :

$$\tilde{n}(r) = \frac{\pi[(r + d/2)^2 - (r - d/2)^2]}{\pi(d/2)^2} = 8r/d$$

Within a ring, in order to keep the axial symmetry, the microvilli are not separated from each other. Nearest neighbor rings, however are separated from each other by a narrow gap of gap-size, g . The radius of the central microvillus is $r_o^{out} = d/2$, while the inner and outer radius of the i -th ring is

$$r_i^{in} = (d/2) + g + (i-1)(g+d) \text{ and } r_i^{out} = (d/2) + i(g+d), \quad (1)$$

respectively.

Above the epithelial cells there is a fluid layer of thickness h . In the case of alveolar cells the top of the fluid layer is a fluid/air interface¹⁹. Hydrophilic ligands are able to diffuse in the fluid region but are unable to cross the interface; it is a reflective boundary. The thin gap between the follicular epithelium and the surface of the oocyte is another example. The surface of the oocyte is a reflective boundary for the ligands of the EGF receptor, because there are no EGF receptors on it^{13,14}.

In our model, the height of each microvillus is always $H = 1\mu m$, while the diameter of a microvillus, d and the gap-size, g varies from $0.2 - 1\mu m$ and $0.01 - 1\mu m$, respectively. The height of the fluid layer above the epithelial cells is $h = 1\mu m$ ¹⁵.

4.2.2. Diffusion Equation of the Model

In the case of the model of Berezhkovskii et al.¹⁵ one ligand is emitted at time zero from a point of the planar epithelial layer. The origin of a cylindrical coordinate system is attached to the point of emission and the plane of the epithelial layer is at $z=0$. The trapping site distribution of the emitted ligand is calculated by solving the time dependent, homogeneous diffusion equation, providing the probability density, $p(r, z=0, t)$ of ligand entrapment in the planar epithelial layer at time t after and at a distance r from the ligand emission. Then $p(r, z=0, t)$ is integrated from time zero to infinity to obtain the trapping site distribution of the ligand, $P(r, 0)$.

We follow a different procedure solving directly the stationary inhomogeneous diffusion equation for the ligand concentration $c(r, z)$ (Poisson equation). In this mathematical representation one point of the epithelial layer emits not one ligand but ligands with a certain frequency and, because of the stationary conditions the epithelial layer adsorbs ligands with the same frequency. In Appendix 1 we point out that the trapping site distribution function, $P(r, 0)$, derived by Berezhkovskii et al.¹⁵ is directly proportional to $c(r, z=0)$, the solution of the following Poisson equation:

$$\frac{1}{r} \frac{\partial}{\partial r} \left(Dr \frac{\partial c}{\partial r} \right) + D \frac{\partial^2 c}{\partial z^2} = f \quad (2)$$

Coordinates r and z are parallel and orthogonal, respectively to the epithelial layer (Figs.1) and the origin coincides with the center of the top of the microvillus that emits ligands. f is the source density function. If the ligands are emitted from a point like source into the half space with $z>0$ the source density function is: $f = \nu \frac{2\delta(r)\delta(z)}{\pi r}$ where ν is the emission frequency of the source. In the analytical calculations (Appendix 1) this point-like source is utilized. However, in the case of the numerical calculations the ligands are emitted from a small source of non-zero volume (see Sec. Numerical Solution of the Diffusion Equation). The source density function is positive and constant within that volume and zero outside the volume. The boundary conditions of Eq.2 are:

$$\left. \frac{\partial c(r, z)}{\partial z} \right|_{z=h} = 0, \quad (3)$$

at the reflective interface.

$$\left. \frac{\partial c(r, z)}{\partial z} \right|_{z=0} = \frac{\kappa}{D} c(r, 0), \quad (4)$$

at the top of the partially reflective surfaces of the concentric cylinders, i.e.: $0 \leq r \leq r_o^{out}$ for the central cylinder and for the concentric rings of cylinders $r_i^{in} \leq r \leq r_i^{out}$ where $i \geq 1$.

$$\left. \frac{\partial c(r, z)}{\partial z} \right|_{z=-H} = \frac{\kappa}{D} c(r, -H), \quad (5)$$

at the bottom of the partially reflective gaps between nearest neighbor concentric cylinders, i.e.: $r_{i-1}^{out} < r < r_i^{in}$ where $i \geq 1$.

$$\left. \frac{\partial c(r, z)}{\partial r} \right|_{r=r_i} = \frac{\kappa}{D} c(r_i, z), \quad (6)$$

at the outer and inner sides of the partially reflective concentric cylinders i.e.: at $r_i = r_i^{out}$ and $r_{i+1} = r_{i+1}^{in}$, respectively where $i \geq 0$ and $-H < z < 0$.

In our model, the diffusion constant of the ligand in the fluid layer adjacent to the epithelial cells, the thickness of the fluid layer and the value of the κ parameter (the trapping rate constant) is, $D = 1 \mu m^2 / s$, $h = 1 \mu m$ and $\kappa = 0.01 \mu m / s^{15}$, respectively. Note that both in the planar model and in our more realistic model the trapping rate constant is the same along the surface of the epithelial layer, i.e. the ligand binding receptors are assumed to be homogeneously distributed.

Since in the case of the planar epithelial model we could point out the proportionality between $P(r, z=0)$ and $c(r, z=0)$ for planar epithelial layer we assume similar proportionality for more realistic geometries of the epithelial layer. In the case of our epithelial model shown in Figs.1a,b Eq.2 is solved numerically and the stationary ligand concentration obtained along the rugged epithelial surface is considered to be proportional to the trapping site distribution of the ligands.

4.2.3. Numerical Solution of the Diffusion Equation

The numerical solution of the Poisson equation (see Eq.2 and the respective four boundary conditions) is obtained by using the partial differential equation (PDE) toolbox of the MATLAB program (The Math Works Inc.). This program package is capable of calculating the ligand concentration, c , at every (r, z) coordinate point of our model system, that is, capable of solving 3D Poisson equation when the system possesses axial symmetry. The two-dimensional, finite computational domain, enclosed by a solid line, is shown in Fig.1c. The origin of the coordinate system is located at the middle of the top of the central microvillus. In addition to the boundaries shown in Fig.1a,b this finite domain

has two lateral boundaries as well: the left one, coinciding with the symmetry axis of the model, and the right one. The boundary conditions at the left and right boundaries are:

$$\left. \frac{\partial c(r, z)}{\partial r} \right|_{r=0} = 0 \quad (7)$$

where $0 \leq z \leq h$ and

$$c(\tilde{R}, z) = 0 \quad (8)$$

where $-H \leq z \leq h$ and \tilde{R} is the r coordinate of the right boundary.

Note that the lateral sizes of Berezhkovskii's¹⁵ and our model (Fig.1a,b) are not restricted. We have to select a large enough value for \tilde{R} in order to get similar numerical solutions to the solutions of the laterally unrestricted models. According to the analytical solution of Berezhkovskii's¹⁵ model the probability density of ligand trapping drops to zero at $r = 100\mu m$, when $D = 1\mu m^2/s$, $\kappa = 0.01\mu m/s$ and $h = 1\mu m$ (see Fig.2 in Ref.15). It will be pointed out in the Results and Discussion section that in the case of our more realistic epithelial model the probability density of ligand trapping drops to zero at an even shorter radial distance from the ligand emission. Thus in all our calculations $\tilde{R} = 100\mu m$. This way the boundary condition on the right side of the computational domain, Eq.8 is naturally satisfied, and the solution is not distorted by the lateral finiteness of the computational domain. The illustration of the computational domain in Fig.1c shows only six microvilli, but in our actual calculations, where $\tilde{R} = 100\mu m$, there are about 100-200 microvilli. In each calculation the actual number depends on the gap-size and diameter of the microvilli.

In Eq.2 the ligands are emitted from an infinitesimal volume, i.e. the ligand source is described by a Dirac δ -function. In the numerical calculations the ligands are emitted from one of the following two small volume sources: 1) From a cylinder that is located at the origin of the coordinate system. Its symmetry axis coincides with the z -axis, and its base is at $z=0$. Its radius and height is $r_c = 0.01\mu m$ and $h_c = 0.01\mu m$, respectively. 2) From a ring located around the central microvillus. The inner radius of the ring is $d/2$, the outer radius is $r_s + d/2$ and its height is h_s . In all but one calculation $r_s = r_c$ and $h_s = h_c$. In Fig.1c the vertical cross section of these sources are shown by small colored squares. The two types of ligand sources provide the same number of ligands per unit time if f is inversely proportional to the volume of the source, i.e.:

$$f_c h_c \pi r_c^2 = f_s h_s \pi [(r_s + d/2)^2 - (d/2)^2] \quad (9)$$

where f_c and f_s is the frequency of ligand emission per unit volume in the case of type 1 and type 2 source, respectively.

The program uses the finite element method to solve PDEs. It approximates the two-dimensional, (r, z) , computational domain, shown in Fig.1c, with a union of triangles. The triangles form a mesh. The triangular mesh is automatically generated and can be further refined. Before solving the PDE, to get fine enough meshes in the narrow gaps between the micrivilli we refined the original mesh three times. To solve the Poisson equation, the default parameters of the program are utilized.

4.3. Results and Discussion

4.3.1. Plot Types of Trapping Site Distributions

We calculated the stationary ligand concentration at the surface of the epithelial layer, c_{surf} for different geometries of the epithelial layer and for different positions of the ligand source. In Appendix 1 we point out that $p_h(r, z) / \kappa \propto rc_{surf}(r, z)$, i.e.: the trapping probability density is proportional to the radial distance times the ligand concentration at the surface of the epithelial layer. Probability density, $p_h(r, z)$ refers to ligand trapping anywhere along a circle of radius r . The plane of the circle is defined by coordinate z . In the case of a planar epithelial layer the z coordinate is equal to zero, while in the case of our epithelial model the z coordinate may change along the epithelial surface from $-H$ to zero. In all our calculated trapping site distribution curves rc_{surf} is plotted instead of p_h / κ . The distributions are plotted in two different ways:

- 1) rc_{surf} is plotted against the radial distance, r from the symmetry axis.
- 2) rc_{surf} is plotted against the parametrized distance, s along the surface of the epithelial layer. The parametrized distance is defined and compared with r in Appendix 2.

The type 1 plot shows the trapping probability densities on the horizontal surfaces of the epithelial layer, i.e.: at the top of the concentric cylinders and at the bottom of the gaps between cylinders. However, it does not show rc_{surf} on the sides of the concentric cylinders. Thus type 1 curves are not continuous and the discontinuities are located at $r = r_i^{out}$ and $r = r_{i+1}^{in}$ where $i \geq 0$ (r_i^{out} and r_{i+1}^{in} are defined by Eq.1). By using type 1 plots we can compare the results of our epithelial model with that of the planar model of the epithelial layer¹⁵. The integral of a type 1 curve, I_1 is proportional to the number of ligands adsorbed on the horizontal segments of the epithelial surface per unit time. The integral is largest in the case of the planar model, $I_1(planar)$ since the whole epithelial surface is horizontal. Thus the proportion of ligands that adsorb on the vertical sides of the cylinders is equal to $P_v = 1 - I_1 / I_1(planar)$.

The type 2 plot shows the trapping probability density everywhere along the surface of the epithelial layer (see inset to Fig.6). Thus in contrast to the $rc_{surf}(r)$ function $rc_{surf}(s)$ is continuous. The disadvantage of this plot is that the relationships between s and the

respective (r,z) cylindrical coordinates on the epithelial surface are not simple (see Appendix 2). The integral of a type 2 curve is proportional to the number of ligands adsorbed by the whole epithelial surface per unit time. Because of the stationary conditions this number should be equal to the number of ligands emitted by the epithelial layer per unit time. The number of molecules emitted is independent from the epithelial geometry and consequently the integral of the type 2 curves is independent from the geometry of the epithelial surface as well.

4. 3.2. Ligands Emission from the Top of a Microvillus

In this section trapping site distributions are calculated when the ligands are emitted from the top of the central microvillus. In these calculations the number of ligands emitted per unit time is kept constant: $f_c h_c \pi r_c^2 = 2\pi \cdot 10^{-2} s^{-1}$.

4.3.2.1. Geometrical parameters g and d decrease simultaneously, while $d = g$

First we consider epithelial geometries where the diameter of the microvilli, d , and the gap-size between the nearest neighbor rings of microvilli, g , are similar. In Fig.2a each type 1 trapping site distribution curve belongs to different geometries of the epithelial layer. The overall shape of these curves is similar to the distribution curve obtained by Berezhkovskii et al. for planar epithelial layer (see dotted line in Fig.2a and dash-dotted line in Fig.2 in Ref.15). Each distribution in Fig.2a increases quickly from zero up to a maximum and then decays with a slower rate to zero. However, as d and g simultaneously decrease the distribution shifts to the left and the integral of the curves decreases.

These changes in the distribution curves of our epithelial model can be explained by the increasing number of receptors within a certain radial distance, r , i.e. by the increasing probability of ligand binding. In the case of the planar epithelial model ligand can bind only on the horizontal layer of the membrane, while in the case of our model ligand can bind on both the horizontal and vertical membrane segments. The proportion of ligand binding on the vertical membrane segments, P_v , increases with decreasing $d=g$ values as follows: 0.606, 0.772 and 0.947 at $d = g = 1\mu m$, $0.5\mu m$ and $0.2\mu m$, respectively.

According to the model of Berezhkovskii et al.¹⁵ the number of ligand receptors per unit surface of the flat epithelial membrane is proportional to κ . Within a period of our model (see definition of the period in Appendix 2) the total epithelial surface to the surface of the horizontal sections is: $A = (d + g + 2H)/(d + g)$. Thus within a radial distance of $g+d$ the number of receptors in our model is A times larger than in the case of the planar model, and we expect that the planar model provides similar distribution curves to our model if κ is substituted by the following effective value:

$$\kappa_{eff} = \kappa A = \kappa(d + g + 2H)/(d + g). \quad (10)$$

When deriving Eq.10 in Appendix 3 we assumed that the receptors on the top of the microvilli and at the bottom of the gaps are similarly accessible. The fine structure of the

distribution curves in Fig.2a shows that the assumption is correct: the concentration at the top of a microvillus (descending segments of the curve) is close to the concentration at the nearby gap (ascending segments of the curve).

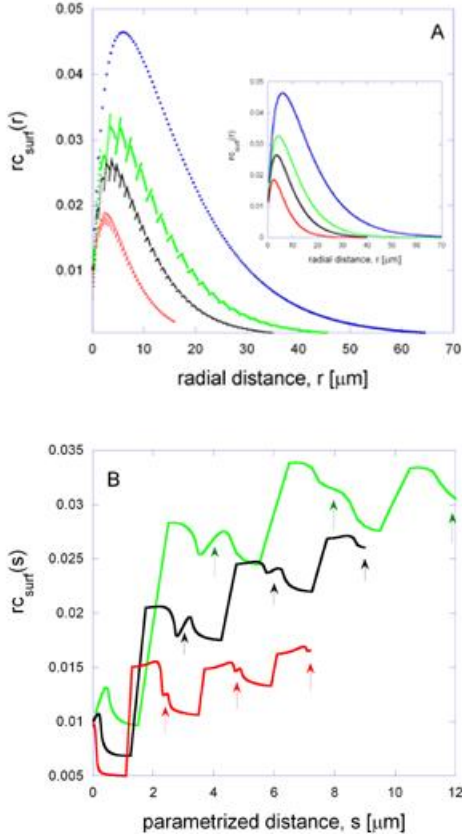


Figure 2. Trapping site distributions when $g = d$ - Ligand emission from the top of the central microvillus.

In the case of these calculations the gap-size, g , and the diameter of the microvillus, d , are equal and decreased gradually: $g = d = 1\mu\text{m}$ (green line); $g = d = 0.5\mu\text{m}$ (black line); $g = d = 0.2\mu\text{m}$ (red line); planar

epithelial layer (blue dots). The ligands are emitted from a small cylinder that is located at the origin of the coordinate system, i.e. at the top of the central microvillus. Its symmetry axis coincides with the z -axis, and its base is at $z=0$. Its radius and height is $r_c = 0.01\mu\text{m}$

and $h_c = 0.01\mu\text{m}$, respectively. The number of ligands produced by the cylindrical source per unit time is $2\pi \cdot 10^{-2} s^{-1}$.

a) Calculated rc_{surf} is plotted against r . Inset: For the planar epithelial model the rc_{surf} vs. r curves are calculated for different effective values of the trapping rate constant, κ_{eff} ; 0.02 (green line), 0.03 (black line), 0.06 (red line) and 0.01 (blue line). These κ_{eff} values were calculated by using Eq.10 and the parameters of the epithelial geometries given in the legend to this figure. b) Calculated rc_{surf} is plotted against s . Only the first three periods of the $rc_{surf}(s)$ functions are shown. The end of each period is marked by an arrow.

The remaining model parameters are: $D = 1\mu\text{m}^2 / s$, $H = 1\mu\text{m}$, $h = 1\mu\text{m}$ and $\kappa = 0.01\mu\text{m} / s$.

In the inset of Fig.2a the distribution curves of the planar epithelial model are calculated at different κ_{eff} values. The κ_{eff} values were calculated from Eq.10 for the epithelial geometries considered in Fig.2a. The overall shapes of the respective curves in Fig.2a and its inset are both in qualitative and quantitative agreement.

While Fig.2a shows the type 1 plots of the trapping site distribution curves, the respective type 2 plots are shown in Fig.2b. Each curve shows only the first three periods. The end of each period is marked by an arrow.

4.3.2.2. Geometrical parameter g decreases gradually, while d remains constant

In Fig.3a type 1 trapping site distribution curves are shown in which g is gradually decreased while d is kept constant ($d = 0.5\mu m$). The overall shape of these curves and the curves in Fig.2a is similar, however at $g < 0.5\mu m$ the ligand concentration at the bottom of each gap is significantly lower than the concentration at the top of the nearby microvillus (see separate dots in Fig.3a). The lower accessibility of the bottom of the gaps can be characterized by means of a single parameter. The so called gap accessibility parameter, a is defined as follows:

$$a = \frac{c_{surf}(r_i^{out} + g/2)}{[c_{surf}(r_i^{out} - \varepsilon) + c_{surf}(r_{i+1}^{in} + \varepsilon)]/2} \quad (11)$$

where the ligand concentration at the bottom of the gap is divided by the average of the concentrations at the upper left and upper right edge of the gap. ε is a short distance, i.e. $0 < \varepsilon/r_i^{out} \approx \varepsilon/r_{i+1}^{in} \ll 1$. By plotting the gap accessibility parameter, a against the radial distance of the gap, $r_i^{out} + g/2$ (not shown) one can realize that a is independent of the gap location and thus a single accessibility parameter is characteristic to any of the gaps in a certain epithelial layer. In Table 1 the gap accessibility parameters obtained at different epithelial layer geometry are listed. The accessibility parameter decreases when the gap-width decreases, while the diameter of the microvilli is kept constant. The accessibility parameter is close to 1 for every epithelial layer geometry, with $d=g$, that is considered in Fig.2a. As we mentioned before this finding is in agreement with our assumption when deriving Eq.10.

When the gap accessibility parameter is significantly smaller than 1 we cannot use Eq.10 to calculate κ_{eff} . In Appendix 3 we derive the following general equation for κ_{eff} :

$$\kappa_{eff} = \kappa \frac{d + ag + 2H(na + 1)/(n + 1)}{d + g} \quad (12)$$

where n is the order of the power function that approximates the ligand concentration along the sides of each gap. When the gap accessibility parameter is not close to zero $n \approx 2$. However, when a approaches zero $n \rightarrow \infty$. Eq.12 results in Eq.10 when the gap is fully accessible, $a=1$. On the other hand, when the gap is too narrow relative to d , $d/(d + g) \approx 1$ and ligands cannot penetrate into the gap, Eq.12 results in $\kappa_{eff} \approx \kappa$, i.e. we get the case of a planar epithelial layer.

We expect that the planar model provides distribution curves similar to the ones in Fig.3a if κ is substituted by the proper κ_{eff} values. The κ_{eff} values are calculated from Eq.12 with $n=2$. The rest of the parameters of Eq.12 were taken for the respective epithelial geometries from Table 1. In the inset of Fig.3a the distribution curves of the planar

epithelial model are shown at different κ_{eff} values. The overall shapes of the respective curves in Fig.3a and in its inset are both in qualitative and quantitative agreement.

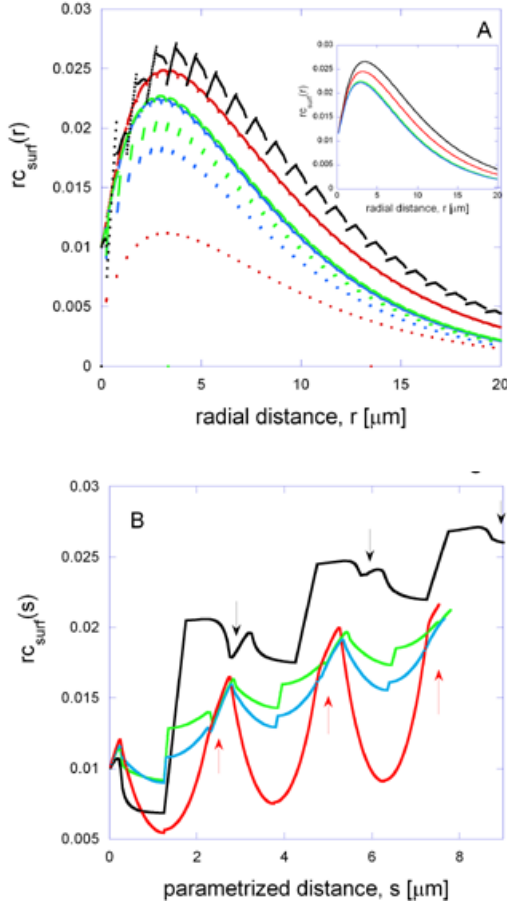


Figure 3. Trapping site distributions when $g \leq d$ - Ligand emission from the top of the central microvillus.

In the case of these calculations the gap-size, g , is gradually decreased, while the diameter of the microvillus, $d = 0.5 \mu m$, is kept constant: $g = 0.5 \mu m$ (black line); $g = 0.1 \mu m$ (green line); $g = 0.05 \mu m$ (blue line); $g = 0.01 \mu m$ (red line). The ligand source is similar to the one described in the legend to Fig.2. a) Calculated rc_{surf} is plotted against r .

Inset: For the planar epithelial model rc_{surf} vs. r curves are calculated for different values of the effective trapping rate constant, κ_{eff} ; 0.03 (black line), 0.0415 (green line), 0.0425 (blue line) and 0.035 (red line). These κ_{eff} values were calculated by using Eq.12 and the gap-accessibility parameters given in Table 1. b) Calculated rc_{surf} is plotted against s . Only the first three periods of the $rc_{surf}(s)$ functions are shown. The end of each period is marked by an arrow.

The remaining model parameters are: $D = 1 \mu m^2 / s$, $H = 1 \mu m$, $h = 1 \mu m$ and $\kappa = 0.01 \mu m / s$.

While Fig.3a shows the type 1 plots of the trapping site distribution curves, the respective type 2 plots are shown in Fig.3b. Each curve shows only the first three periods. The end of each period is marked by an arrow.

4.3.3. Ligand Emission from the Side of a Microvillus

In Fig.4a type 1 trapping site distribution curves are shown. In the case of each curve the geometry of the epithelial layer is characterized by $g=0.01\mu\text{m}$ and $d=0.5\mu\text{m}$, while the ligands are emitted from a narrow ring located around the side of the central microvillus. The inner radius of the ring is $\hat{r} = d/2$ and it has the following three different locations along the central microvillus: $\hat{z} = -0.1H$ (red curve); $\hat{z} = -0.5H$ (blue curve); and $\hat{z} = -0.9H$ (green) curve, where \hat{z} is the z -coordinate at the top of the ring. The number

Table 1. Parameters of the Planar Model Resulting in Distributions Equivalent with the Axially Symmetric Model

$d (\mu\text{m})$	$g (\mu\text{m})$	Source type	a	$\kappa_{\text{eff}} / \kappa$	f_{red} / f
1	1	Cylinder	0.984	1.98	1
0.5	0.5	Cylinder	0.972	2.95	1
0.2	0.2	Cylinder	0.943	5.78	1
0.5	0.1	Cylinder	0.90	4.15	1
0.5	0.05	Cylinder	0.82	4.25	1
0.5	0.01	Cylinder	0.45	3.5	1
0.5	0.5	Ring/top	0.972	2.95	0.99
0.5	0.5	Ring/middle	0.972	2.95	0.98
0.5	0.5	Ring/bottom	0.972	2.95	0.97
0.5	0.1	Ring/top	0.90	4.15	0.972
0.5	0.1	Ring/middle	0.90	4.15	0.918
0.5	0.1	Ring/bottom	0.90	4.15	0.893
0.5	0.05	Ring/top	0.82	4.25	0.953
0.5	0.05	Ring/middle	0.82	4.25	0.856
0.5	0.05	Ring/bottom	0.82	4.25	0.814
0.5	0.01	Ring/top	0.45	3.5	0.87
0.5	0.01	Ring/middle	0.45	3.5	0.59
0.5	0.01	Ring/bottom	0.45	3.5	0.455

κ_{eff} : effective trapping rate constant; f_{red} : reduced source strength; a : gap accessibility is defined for gaps where ring-like source does not located.

of ligands emitted by the ring per unit time is the same as the number of ligands emitted by the cylindrical source at the top of the microvillus. The symmetry axis of the cylindrical source coincides with the z -axis and $z=0$ at the bottom of the cylinder. For comparison Fig.4a also shows the trapping site distribution in the case of this cylindrical source (black line). The distributions in the case of the ring-like sources are proportional everywhere to the distribution belonging to the cylindrical source except in the first period of the epithelial layer (see Fig.4b). Thus a small cylindrical source at the top of the central microvillus produces almost the same trapping site distribution as a ring-like source around the central microvillus if the strength of the cylindrical source is properly reduced. These similarities between the distributions imply the similarity of the gap accessibility parameter values at different source types (see Table 1).

In conclusion the trapping probability density of the planar epithelial model $c_{surf}(r; \kappa, f, g = 0)$ can be used to approximate the distributions generated by our more realistic epithelial model as follows:

$$c_{surf}(r; \kappa, f, g) \approx \begin{cases} \frac{f_{red}}{f} c_{surf}(r; \kappa_{eff}, f, 0) & r_i^{in} \leq r < r_i^{out} \\ \frac{f_{red}}{f} a c_{surf}(r_i^{out} + g/2; \kappa_{eff}, f, 0) & r_i^{out} \leq r < r_{i+1}^{in} \end{cases}$$

where $i > 0$, i.e. the first period is excluded. In Table 1 we summarize the proper parameter values (a , κ_{eff} and f_{red}) of the planar model that result in similar trapping site distributions as our more realistic epithelial geometries.

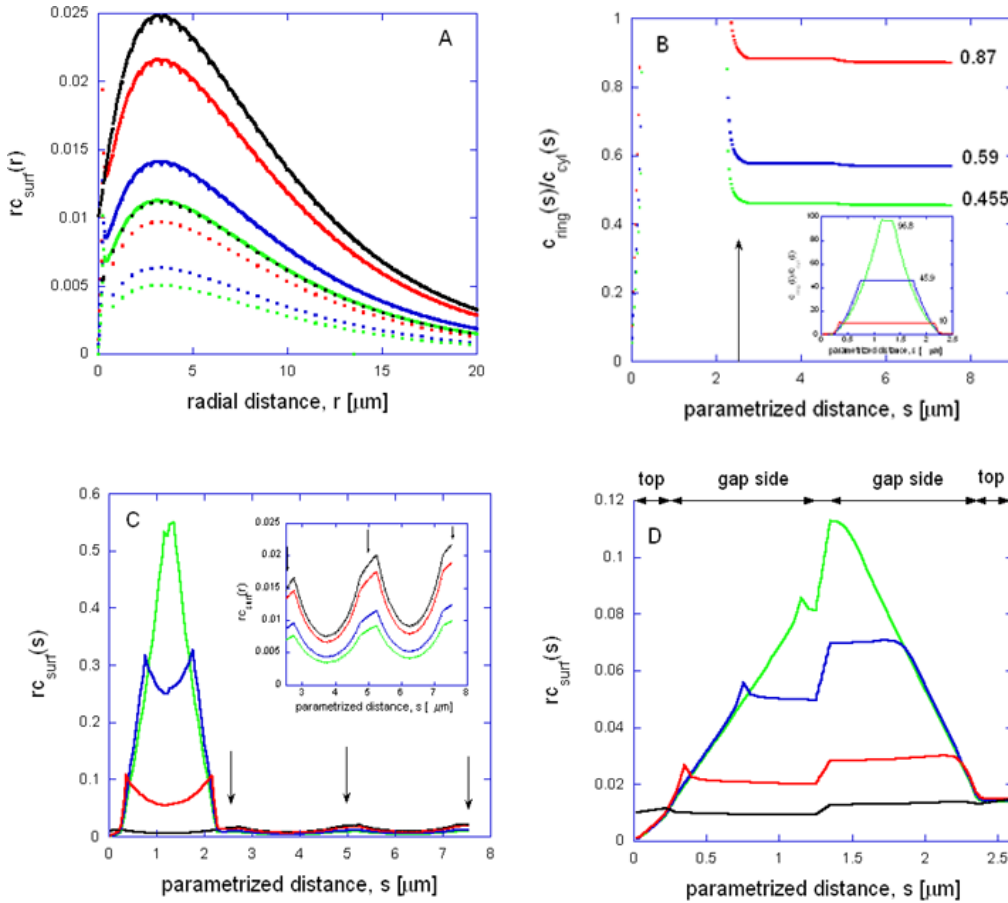


Figure 4. *Trapping site distributions - Ligand emission from the side of the central microvillus.*

In the case of these calculations the ligand source is a narrow ring that is located around the side of the central microvillus. The inner radius of the ring is $\hat{r} = d/2$, the vertical coordinate at the top of the ring is \hat{z} , the radial and vertical width of the ring is r_s and h_s , respectively. The depth of the ligand source along the microvillus is gradually increased: $\hat{z} = -0.1H$ (red line); $\hat{z} = -0.5H$ (blue line); $\hat{z} = -0.9H$ (green line). In the case of the black line the ligand source is cylindrical, similar to the one described in the

dc_11_10

legend to Fig.2. The number of ligands produced by the ring-like ligand source per unit time, $2\pi \cdot 10^{-2} s^{-1}$ is equal with that of the cylindrical source (see Eq.9). a) Calculated rc_{surf} is plotted against r . $h_s = r_s = 0.002\mu m$ and $g = 0.01\mu m$. b) The ratio of the type 2 trapping site distribution at the ring-like source to the distribution at the cylindrical source, $c_{ring}(s)/c_{cyl}(s)$. An arrow marks the end of the first period. The inset shows only the first period of the $c_{ring}(s)/c_{cyl}(s)$ curves. $h_s = r_s = 0.002\mu m$ and $g = 0.01\mu m$. c) Calculated rc_{surf} is plotted against s . The first three periods of the $rc_{surf}(s)$ functions are shown. An arrow marks the end of each period. The inset shows the details of the second and third period. $h_s = r_s = 0.002\mu m$ and $g = 0.01\mu m$. d) Calculated rc_{surf} is plotted against s . Only the first period of the $rc_{surf}(s)$ function is shown. Intervals of s parameter belonging to different parts of the first period are indicated by double arrows. $h_s = r_s = 0.01\mu m$ and $g = 0.1\mu m$.

The remaining model parameters are: $D = 1\mu m^2 / s$, $\kappa = 0.01\mu m / s$, $h = 1\mu m$, $d = 0.5\mu m$ and $H = 1\mu m$.

As we mentioned above at the first period in the case of ring-like sources the trapping site distributions are not proportional to the distribution belonging to a cylindrical source. In Figs4c and Fig.4d the type 2 plots of the *first period* of the distribution curves are shown, where $g = 0.01\mu m$ and $g = 0.1\mu m$, respectively. From these plots one can draw the following conclusions:

- i) Each trapping site distribution has a local maximum at the source. The global maximum of the trapping site distribution can be found on the opposite side of the gap at the level of the source.
- ii) On both sides of the gap, going up from the level of the source the trapping probability density linearly decreases.
- iii) Below the level of the ring-like source the trapping site distribution function is proportional to the trapping site distribution function of the cylindrical source (see inset of Fig.4b). However, the proportionality constant in this region of the distribution function is larger than 1. For example at $g = 0.01\mu m$ the proportionality constant is 96.8, 45.9 and 10 for sources around the bottom, middle and top of the microvillus, respectively.

4.3.4. Probability of Autocrine Signaling

One is frequently interested in the probability that a ligand initiated at the cell surface is recaptured by the same cell. This probability, the probability of autocrine signaling, is denoted by P_{auto} . The fraction of the ligands that bind to the cell's neighbors, the probability of paracrine signaling, is $P_{para} = 1 - P_{auto}$. By using the above determined trapping site distributions, $rc_{surf}(s)$, one can calculate P_{auto} at different epithelial geometries and ligand sources. Let us assume that the radius of the cross section of an epithelial cell is R_{cell} . The distance between the center of the cell's cross section and the center of the microvillus that emits the ligand is b . The probability that the ligand emitted by this microvillus will be recaptured by the parent cell is:

$$\hat{P}_{auto}(b) = \frac{\int_0^{\infty} Frc_{surf}(s)ds}{\int_0^{\infty} rc_{surf}(s)ds} \quad (13)$$

where

$$F = \begin{cases} 1 & \text{if } r \leq R_{cell} - b \\ 1 - \pi^{-1} \arccos\left(\frac{R_{cell}^2 - b^2 - r^2}{2br}\right) & \text{if } R_{cell} - b < r < R_{cell} + b \\ 0 & \text{if } r \geq R_{cell} + b \end{cases} \quad (14)$$

If one draws a circle of radius r around the emitting microvillus F is the fraction of the arc that falls within the cross section of the cell. This fraction becomes zero when $r \geq R_{cell} + b$. The inset of Fig.5 is an illustration of the cell (red circle) and the emitting microvillus (black dot). The distance between the center of the cell (red dot) and the point of emission is denoted in our above calculations by b . The black circles around the point of emission illustrate two sets of trapping sites. The small circle around the black dot (solid line) is completely within the red circle. In this case $F=1$. The large circle around the point of emission (dashed line) is only partially within the red circle. About a quarter of its arc falls into the red circle, i.e. $F \approx 0.25$.

The probability that the ligand emitted by any of the cell's microvilli is recaptured by the parent cell is:

$$P_{auto} = \frac{\sum_{i=1}^{N_m} \hat{P}_{auto}(b_i)}{N_m} \approx \frac{\int_0^{R_{cell}} [\hat{P}_{auto}(b) 2b\pi] db}{R_{cell}^2 \pi} \quad (15)$$

where N_m is the number of microvilli per cell and b_i is the distance of the i -th microvillus from the center of the cell's cross section. The approximation in Eq.15 can be used when $N_m \gg 1$. In Fig.5 P_{auto} is plotted against the gap-width, g . The remaining geometrical parameters, $R_{cell} = 5.5\mu m$, $d = 0.5\mu m$, $h = 1\mu m$ and $H = 1\mu m$ are kept constant. The red, blue and green curves refer to ring-like ligand sources that are around the top, middle and bottom of the microvilli, respectively, while the black curve refers to small cylindrical sources located at the top of the microvilli. At $g > 0.05\mu m$ each curve increases with decreasing gap size. This trend can be explained by the increasing number of accessible receptors (or trapping sites) within a certain radial distance. However, by further decreasing the gap size two trends evolve:

- 1) at ring-like sources P_{auto} quickly increases. This is the case because ligands emitted into a gap frequently remain trapped in that gap when $g < 0.05\mu m$ (see Fig.4c).

- 2) at small cylindrical sources P_{auto} quickly decreases. For ligands emitted to the bulk fluid phase the gap accessibility is significantly reduced when $g < 0.05 \mu m$ (see Table 1). At $g = 0 \mu m$ the gap accessibility is zero, i.e.: we get the planar model, and P_{auto} becomes minimal, $P_{auto} = 0.19$ (see purple circle in Fig.5).

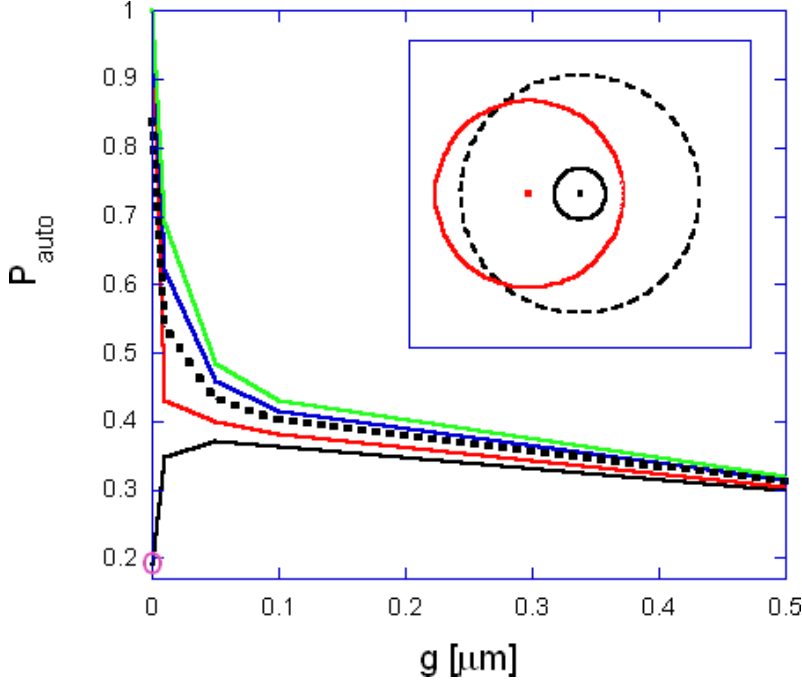


Figure 5. Probability of autocrine signaling

The probability of autocrine signaling, P_{auto} is plotted against the gap size, g , for different ligand sources. P_{auto} is calculated by using Eq.15 and the trapping site distribution curves. Small cylindrical sources at the top of the microvilli (black line). Narrow, ring-like sources located around the microvilli at $\hat{z} = -0.1H$ (red line); $\hat{z} = -0.5H$ (blue line); $\hat{z} = -0.9H$ (green line). The autocrine signaling probability calculated from the planar model (purple circle). The overall probability of autocrine signaling is calculated by using Eq.16 (dotted line).

The detailed characterizations of the cylindrical and ring-like sources are given in the legends to Figs.2 and 4.

The remaining model parameters are: $D = 1 \mu m^2 / s$, $R_{cell} = 5.5 \mu m$, $d = 0.5 \mu m$, $H = 1 \mu m$, $h = 1 \mu m$ and $\kappa = 0.01 \mu m / s$.

The inset is an illustration of the cell (red circle) and the emitting microvillus (black dot). The distance between the center of the cell (red dot) and the point of emission is denoted in Eq.14 by b . The black circles around the point of emission illustrate two sets of trapping sites.

One can calculate the overall probability of autocrine signaling, P_{auto}^{tot} , by averaging the autocrine probabilities obtained for different ligand sources (see black, red, blue, and green solid lines in Fig.5) as follows:

$$P_{auto}^{tot} = \frac{0.5dP_{auto}^{black} + 0.3HP_{auto}^{red} + 0.4HP_{auto}^{blue} + (0.3H + 0.5g)P_{auto}^{green}}{H + 0.5(d + g)} \quad (16)$$

The overall probability of autocrine signaling is plotted in Fig.5 (dotted line). At $g > 0.05\mu m$ it slowly increases with decreasing gap size. However, the increase of P_{auto}^{tot} becomes very steep at $g \approx 0\mu m$, i.e. when the microvilli are closely packed.

On the basis of this result it is conceivable that an epithelial cell is able to efficiently regulate its communication with its neighbors. If the microvilli of the cell are closely packed the probability of paracrine signaling, $P_{para}^{tot} = 1 - P_{auto}^{tot}$ is about 0.2. However, this probability jumps to about 0.5 if the cell is able to slightly loosen the tight packing, e.g. by decreasing the diameter of the microvilli by only 2%. We think that the bundles of actin filaments located in each microvillus are actually able to make this change in the microvilli's geometry.

4.4. Conclusions

In this chapter²² a model of autocrine/paracrine signaling on an epithelial layer is developed. The axially symmetric model of the epithelial layer explicitly considers the microvilli of the epithelial cells and the gaps between nearest neighbor microvilli. Trapping site distribution functions and probability of autocrine signaling are calculated for different epithelial geometries and ligand sources by solving numerically the inhomogeneous stationary diffusion equation, the Poisson equation. The global characteristics of the calculated trapping site distribution curves are similar to the ones obtained for a planar epithelial model, while the superimposed small periodical changes of the curves reflect the details of the epithelial geometry. However, when ligands are emitted into a narrow gap between nearest neighbor microvilli the probability of local trapping is particularly high, causing locally a large deviation from the overall behavior of the trapping site distribution curves. On the basis of our result it is conceivable that an epithelial cell is able to efficiently regulate its communication with its neighbors by slightly changing the geometry of the microvilli.

4.5. Appendix 1

In this appendix we point out that the trapping site distribution of Berezhkovskii's¹⁵ model is proportional to $c(r,0)$, the solution of Eq.2 at the surface of the planar epithelial layer.

In Berezhkovskii's model the probability density of finding the ligand at space coordinates (r,z) and at time t is

$$p(r, z, t) = g(z, t)G_{2d}(r, t), \quad (A1)$$

where G_{2d} , the free propagator in two dimensions, from Eq.1 in Ref.15 is

$$G_{2d}(r, t) = (4\pi Dt)^{-1} \exp(-r^2 / 4Dt) \quad (\text{A2})$$

and g , the propagator in one dimension, from the solution of Eq.A2 in Ref.15 is

$$g(z, t) = \sum_{n=1}^{\infty} A_n Z_n(z) \exp(-Dk_n^2 t). \quad (\text{A3})$$

Eq.A3 satisfies the following initial and boundary conditions (see Eqs.A3 in Ref.15):

$$g(z, 0) = \delta(z), \quad \left. \frac{\partial g}{\partial z} \right|_{z=0} = \frac{\kappa}{D} g(0, t), \quad \text{and} \quad \left. \frac{\partial g}{\partial z} \right|_{z=h} = 0 \quad (\text{A4})$$

In Eq.A3 k_n , A_n and $Z_n(z)$ are defined as follows:

k_n 's are positive roots of the equation $\frac{D}{\kappa} k_n = \cot(k_n h)$, $n = 1, 2, \dots$

$$A_n = \frac{2D\kappa k_n}{D\kappa + h(\kappa^2 + D^2 k_n^2)}. \quad (\text{A5})$$

and

$$Z_n(z) = \sin(k_n z) + \frac{D}{\kappa} k_n \cos(k_n z) \quad (\text{A6})$$

In order to get the trapping site distribution Berezhkovskii et al.¹⁵ took the integral of the probability density $p(r, z, t)$

$$P(r, z) = \int_0^{\infty} p(r, z, t) dt = \sum_{n=1}^{\infty} A_n Z_n(z) R_n(r), \quad (\text{A7})$$

where

$$R_n(r) = \frac{1}{2\pi D} K_o(k_n r) \quad (\text{A8})$$

and $K_o(k_n r)$ is a modified Bessel function of the second kind.

From $P(r, z)$ they calculated the trapping site distribution on the $z=0$ surface of the epithelial layer as follows (see Eq.5 in ref¹⁵):

$$p_h(r) = 2r\pi\kappa P(r, 0) = 2r\kappa D \sum_{n=1}^{\infty} \frac{k_n^2}{D\kappa + h(\kappa^2 + D^2 k_n^2)}. \quad (\text{A9})$$

Now let us point out that the $P(r, z)$ function is the solution of Eq.2, the inhomogeneous, stationary diffusion equation (Poisson equation), with a partially adsorbing boundary at $z=0$

$$\left. \frac{\partial c(r, z)}{\partial z} \right|_{z=0} = \frac{\kappa}{D} c(r, 0) \quad (\text{A10})$$

with a reflective boundary at $z=h$.

$$\left. \frac{\partial c(r, z)}{\partial z} \right|_{z=h} = 0 \quad (\text{A11})$$

and with a point-like source at the origin, i.e. $f = \nu \frac{2\delta(r)\delta(z)}{\pi r}$, where ν is the emission frequency of the source.

First we show that $P(r, z)$ is a solution of Eq.2 at $r > 0$, i.e.:

$$\frac{1}{r} \frac{\partial}{\partial r} \left(D r \frac{\partial P}{\partial r} \right) + D \frac{\partial^2 P}{\partial z^2} = 0 \quad (\text{A12})$$

After substituting Eq.A7 into Eq.A12 we get

$$\begin{aligned} \frac{D}{r} \frac{\partial}{\partial r} \left(r \frac{\partial P}{\partial r} \right) + D \frac{\partial^2 P}{\partial z^2} = \\ D \sum_{n=1}^{\infty} A_n Z_n \left(\frac{d^2 R_n}{dr^2} + \frac{1}{r} \frac{dR_n}{dr} \right) + A_n R_n \frac{d^2 Z_n}{dz^2} = \\ D \sum_{n=1}^{\infty} A_n Z_n \left(\frac{d^2 R_n}{dr^2} + \frac{1}{r} \frac{dR_n}{dr} - k_n^2 R_n \right) \end{aligned} \quad (\text{A13})$$

$R_n(r)$ is proportional to $K_o(k_n r)$ (see Eq.A8) and thus the bracketed part in the second equality in Eq.A13 equals zero. This is the case because $K_o(k_n r)$ is a modified Bessel function of the second kind that solves the modified Bessel differential

equation: $\frac{1}{r} \frac{d}{dr} \left(r \frac{dR_n}{dr} \right) = k_n^2 R_n$ when $r > 0$. Thus Eq.A13 is equal to zero when $r > 0$.

Now let us point out that Eq.A7 solves Eq.2 when $r \rightarrow 0$. When $r \rightarrow 0$ the modified Bessel function of the second kind, $K_o(k_n r)$ does not solve the modified Bessel differential equation. For small r the asymptotic form of the modified Bessel function of the second kind, $K_o(k_n r)$, is $K_o(k_n r) \approx -\ln(k_n r)^{21}$. After substituting this asymptotic form into Eq.A13 we get

$$\begin{aligned} \frac{D}{r} \frac{\partial}{\partial r} \left(r \frac{\partial P}{\partial r} \right) + D \frac{\partial^2 P}{\partial z^2} \approx \\ \frac{D}{2\pi D} \sum_{n=1}^{\infty} A_n Z_n \left(\frac{1}{r^2} - \frac{1}{r^2} + k_n^2 \ln(k_n r) \right) \approx \frac{1}{2\pi} \ln(r) \sum_{n=1}^{\infty} k_n^2 A_n Z_n = \\ -\frac{1}{2\pi} \ln(r) \frac{d^2 \delta(z)}{dz^2} \end{aligned} \quad (\text{A14})$$

where in the second equality the following approximation is taken: $\frac{\ln(r)}{\ln(r) + \ln(k_n)} \approx 1$, and

the last equality is the consequence of the first equation in Eq.A4. In Eq.A14 the second derivative of the Dirac δ -function is:

$$\frac{d^2 \delta(z)}{dz^2} = (-1)^2 2! \delta(z) / z^2 = \frac{2}{z^2} \delta(z) \quad (\text{A15})$$

After substituting Eq.A15 into Eq.A14 we get

$$\frac{D}{r} \frac{\partial}{\partial r} \left(r \frac{\partial P}{\partial r} \right) + D \frac{\partial^2 P}{\partial z^2} \approx -\frac{1}{\pi} \ln(r) \frac{\delta(z)}{z^2} \quad (\text{A16})$$

Thus when $z \rightarrow 0$ and $r \rightarrow 0$ the right hand side of Eq.A16 is approaching $+\infty$, i.e. $P(r,z)$ is the solution of Eq.2 at $z=r=0$. On the other hand when $z \neq 0$ and $r \rightarrow 0$ the right hand side of Eq.A16 is 0, i.e. $P(r,z)$ is again the solution of Eq.2 at $z \neq 0$ and $r=0$. By substituting Eq.A7 into Eqs.A10, A11 we also can show that $P(r,z)$ satisfies the boundary conditions of Eq.2.

4.6. Appendix 2

Let us consider a point on the epithelial surface. Its distance from the origin can be given by either the radial distance, r or by the parametrized distance, s . The inset of Fig.6 illustrates these distances. The relationships between the parametrized distance, s and the respective r and z cylindrical coordinates are listed in Table 2. At a certain epithelia geometry ($d = 1\mu m$, $g = 0.2\mu m$ and $H = 1\mu m$) the $r(s)$ and $z(s)$ relationships (marked by solid and dotted line, respectively) are plotted in Fig.6. Note that $z(s)$ is a periodic function in the case of any geometry of our epithelial model with a period of $d + g + 2H$.

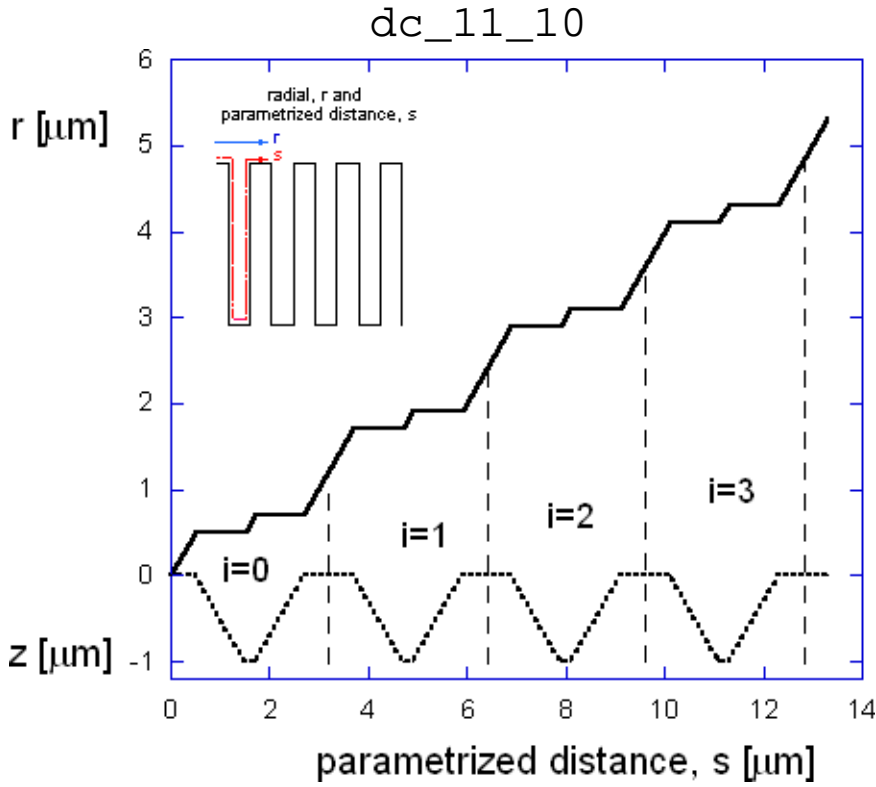


Figure 6. Cylindrical coordinates vs. parametrized distance

Cylindrical coordinates r and z are plotted against the parametrized distance s (solid and dotted line, respectively). The inset is an illustration of the parametrized distance, s . These plots refer to an epithelial geometry that is characterized by the following parameters: the height of each microvillus is $H = 1\mu m$, the diameter of a microvillus is $d = 1\mu m$ and the gap-size between the nearest neighbor cylinders is $g = 0.2\mu m$. The four periods of the $z(s)$ function are divided by vertical dashed lines. In Table 2 the $r(s)$ and $z(s)$ relationships are given for any geometry of the epithelial layer.

Table 2 Relationships between the Parametrized Distance, s and the r, z Coordinates.

r coordinate	z coordinate	range of s parameter
$s - 2iH$	0	$r_i^{out} - \frac{d}{2} + 2iH \leq s < r_i^{out} + 2iH$
r_i^{out}	$r_i^{out} + 2iH - s$	$r_i^{out} + 2iH \leq s < r_i^{out} + (2i + 1)H$
$s - (2i + 1)H$	$-H$	$r_i^{out} + (2i + 1)H \leq s < r_{i+1}^{in} + (2i + 1)H$
r_{i+1}^{in}	$s - [r_{i+1}^{in} + 2(i + 1)H]$	$r_{i+1}^{in} + (2i + 1)H \leq s < r_{i+1}^{in} + 2(i + 1)H$
$s - 2(i + 1)H$	0	$r_{i+1}^{in} + 2(i + 1)H \leq s < r_{i+1}^{out} - \frac{d}{2} + 2(i + 1)H$

Note: Integer $i \geq 0$ while r_i^{out} and r_i^{in} are defined by Eqs.1

4.7. Appendix 3

Calculating the area accessible for ligand absorption

Let us consider a period of our epithelial layer (see definition of a period in Appendix 2) and calculate the area accessible to ligand adsorption. The radial coordinate at the middle of the period, i.e. at the middle of the gap, is R . The top of the microvilli is completely accessible for ligand adsorption, and thus the accessible area is:

$$A_{top} = \pi[(R - g/2)^2 - (R - \{g + d\}/2)^2] + \pi[(R + \{g + d\}/2)^2 - (R + g/2)^2] \quad (A17)$$

The accessible area of the bottom of the gap is:

$$A_{bot} = a\pi[(R + g/2)^2 - (R - g/2)^2] \quad (A18)$$

where a is the accessibility of the bottom of the gap (see Eq.11).

The accessible area of the sides of the gap is:

$$A_{side} = \langle a_{side} \rangle [2(R - g/2)\pi H + 2(R + g/2)\pi H] \quad (A19)$$

where $\langle a_{side} \rangle$ is the average accessibility of the sides of the gap.

The total accessible area of the period is:

$$A_{tot} = A_{top} + A_{bot} + A_{side} = 2R\pi(d + ag) + \langle a_{side} \rangle 4R\pi H \quad (A20)$$

The respective accessible area in the case of the planar model is:

$$A_{plan} = \pi[(R + \{g + d\}/2)^2 - (R - \{g + d\}/2)^2] = 2R(g + d)\pi \quad (A21)$$

The ratio of the accessible areas is:

$$A = A_{tot} / A_{plan} = \frac{d + ag + \langle a_{side} \rangle 2H}{d + g} \quad (A22)$$

If every part of the epithelial surface is completely accessible, $a = a_{side} = 1$ we get Eq.10.

In order to calculate the average accessibility along the sides of a gap, $\langle a_{side} \rangle$ let us consider type 2 plots (in Fig.3b) that show the ligand concentration along the sides of the gaps. When $a \leq 1$ but not close to zero the concentration along the side of the gap can be approximated by a parabolic function. Thus the accessibility of the side of a gap a_{side} should also increase in a parabolic fashion from a to 1 as follows:

$$a_{side} \approx a + \frac{1 - a}{H^2} (s - s_{bot})^2 \quad (A23)$$

where s_{bot} is the parametrized distance at the bottom of the far side of a gap. When a approaches zero higher than second order power functions would approximate the concentration along the side of a gap and thus a_{side} is:

$$a_{side} \approx a + \frac{1 - a}{H^n} (s - s_{bot})^n \quad (A24)$$

where n is the order of the power function.

By using Eq.A24 the average accessibility of the side of a gap is:

$$\langle a_{side} \rangle = \frac{1}{H} \int_{s_{bot}}^{s_{bot} + H} a_{side}(s) ds = \frac{na + 1}{n + 1} \quad (A25)$$

dc_11_10

When $a \rightarrow 0$ the order of the power function increases, i.e. $n \rightarrow \infty$, and thus $\langle a_{side} \rangle \rightarrow 0$. After substituting Eq.A25 into Eq.A22 one can get an expression for the ratio of the accessible areas, A , and also for $\kappa_{eff} = \kappa A$ (see Eq.12).

References

References to Chapter 1.1.

- (1) Neumann, E.; Rosenheck, K. *J. Membrane Biol.* **1972**, *10*, 279-290.
 - (2) Dimitrov, D.S.; Jain, R.K. *Biochim. Biophys. Acta* **1984**, *779*, 437-468.
 - (3) Sugar, I.P.; Neumann, E. *Biophys. Chem.* **1984**, *19*, 211-225.
- Sugar, I.P. Stochastic model for electric field-induced membrane pores. *In*: Electroporation and electrofusion in cell Biology, Eds: N. Neumann, A. Sowers, and C. Jordan, Plenum Publishing Corporation, **1989**, pp. 97-110.
- Sugar, I.P. Exact solutions of a stochastic model of electroporation. *In*: Charge and Field Effects in Biosystems. Ed: M.J. Allen. Birkhäuser, **1992**, pp 273-284.
- (4) Powell, K.T.; Derrick, E.G.; Weaver, J.C. *Bioelectrochem. Bioenerg.* **1986**, *15*, 243-255.
 - (5) Sugar, I.P.; Forster, W.; Neumann, E. *Biophys. Chem.* **1987**, *26*, 321-337.
 - (6) Abidor, I.G.; Arakelyan, V.B.; Chernomordik, L.V.; Chizmadzhev, Y.A.; Pastushenko, V.F.; Tarasevich, M.R. *Bioelectrochem. Bioenerg.* **1979**, *6*, 37-52.
 - (7) Goel, N.S.; Richter-Dyn, N. *Stochastic Models in Biology*; Academic Press: New York, 1974
 - (8) Kashchiev, D.; Exerowa, D. *Biochim. Biophys. Acta* **1983**, *732*, 133-145.
 - (9) Kashchiev, D. *Colloid Polymer Sci.* **1987**, *265*, 436-441.
 - (10) Needham, D.; Hochmuth, R.M. *Biophys. J.* **1989**, *55*, 1001-1009.
 - (11) Jordan, P.C. *Biophys. J.* **1982**, *39*, 157-164.
 - (12) Benz, R.; Beckers, F.; Zimmermann, U. *J. Membr. Biol.* **1979**, *48*, 181-204.
 - (13) Tien, H.T. *Bilayer Lipid Membranes*, Dekker, New York, **1974**
 - (14) Teissie, J.; Tsong, T.Y. *Biochemistry* **1981**, *20*, 1548-1554.
 - (15) Arakelyan, V.B.; Chizmadzhev, Y.A.; Pastushenko, V.F. *Bioelectrochem. Bioenerg.* **1979**, *6*, 81-87.
 - (16) Benz, R.; Zimmermann, U. *Bioelectrochem. Bioenerg.* **1980**, *7*, 723-739.
 - (17) Benz, R.; Zimmermann, U. *Biochim. Biophys. Acta* **1981**, *640*, 169-178.

References to Chapter 1.2.

- (1) Stämpfli, R. *Annals Acad. Brasil. Ciero.* **1958**, *30*, 57-63.
- (2) Sale, A.J.H.; Hamilton, W.A. *Biochim. Biophys. Acta* **1968**, *163*, 37-43.
- (3) Neumann, E.; Rosenheck, K. *J. Membrane Biol.* **1972**, *10*, 279-290.
- (4) Zimmermann, U.; Schulz, J.; Pilwat, G. *Biophys. J.* **1973**, *13*, 1005-1013.
- (5) Neumann, E.; Schaefer-Ridder, M.; Wang, Y.; Hofschneider, P.H. *EMBO J.* **1982**, *1*, 841-845.
- (6) Neumann, E.; Sowers, A.E.; Jordan, C.A. *Electroporation and Electrofusion in Cell Biology*. E. Neumann, A.E. Sowers and C.A. Jordan editors. Plenum Press, New York and London, **1989**.
- (7) Friedrich, U.; Stachowicz, N.; Simm, A.; Fuhr, G.; Lucas, K.; Zimmermann, U. *Bioelectrochem. Bioenerg.* **1998**, *47*, 103-111.
- (8) Eidsath, A.; Button, D.; Schmukler, R.E. **1995**, *unpublished*

- (9) Yang, T.A.; Heiser, W.C.; Sedivy, J.M. *Nucleic Acid Research* **1995**, *15*, 2803-2810.
- (10) Schmukler, R.E. **1992**. *Methods of Electroporation and Electrofusion*. U.S. Patent No. 5,173,158, 1992.
- (11) Schmukler, R.E. **1994**. *Apparatus for Electroporation and Electrofusion*. U.S. Patent No. 5,283,194, 1994.
- (12) Schmukler, R.E. *Materials Research Society Proceedings*. **1996**, *411*, 45-56.
- (13) Huang, Y.; Rubinsky, B. *Biomed. Microdev.* **1999**, *2*, 145-150.
- (14) Schmukler, R.E. *Proceedings XI International Conference on Electrical Bio-Impedance*. Oslo, Norway. **2001**, pp:233-236.
- (15) Sugar, I.P.; Schmukler, R.E. *Proceedings XI International Conference on Electrical Bio-Impedance*. Oslo, Norway. **2001**, pp:149-152.
- (16) Sugar, I.P., Lindesay, J., Schmukler, R.E. *J.Phys.Chem.B.* **2003**, *107*, 3862-3870.
- (17) Schmukler, R.E. *A new technique for measurement of isolated cell impedance*. Eng.Sc.D. Thesis, Columbia University. **1981**.
- (18) Cole, K.S. *Membranes, Ions and Impulses*. University of California Press, Berkeley. **1972**.
- (19) Schwan, H.P. *Electroporation and Electrofusion in Cell Biology*. E. Neumann, A.E. Sowers and C.A. Jordan editors. Plenum Press, New York and London. **1989**, pp.3-22.
- (20) Kinoshita, K. Jr.; Ashikawa, I.; Saita, N.; Yoshimura, H.; Itoh, H.; Nagayama, K.; Ikegami, A. *Biophys. J.* **1988**, *53*, 1015-1019.
- (21) Hibino, M.; Shigemori, M.; Itoh, H.; Nagayama, K.; Kinoshita, K. Jr. *Biophys. J.* **1991**, *59*, 209-220.
- (22) Hibino, M.; Itoh, H.; Kinoshita, K. Jr. *Biophys. J.* **1993**, *64*, 1789-1800.
- (23) Bordi, F.; Cametti, C.; Misasi, R.; De Persio, R. *Eur. Biophys. J.* **1997**, *26*, 215-225.
- (24) Takashima, S.; Schwan, H.P. *J. Membr. Biol.* **1974**, *17*, 51-68.
- (25) Handbook of Plastics; Reed Plastics, Inc., 1996.
- (26) CRC Handbook of Chemistry and Physics; CRC Press: Boston, 1990.

References to Chapter 2.

- (1) Thompson, T.E.; Sankaram, M.B.; Biltonen, R.L. ; Marsh, D.; Vaz, W.L.C. *Mol.Membr.Biol.* **1995**, *12*, 157.
- (2) Mouritsen, O.G.; Biltonen, R.L. in "Protein-Lipid Interactions, New Comprehensive Biochemistry" (A. Watts ed.) p.1. Elsevier, Amsterdam, 1993.
- (3) Thompson, T. ; Barenholz, Y.; Brown, R.; Correa-Freire, M.; Young, W.; Tillack, T. in "Enzymes of Lipid Metabolism II" (L. Freysz et al. eds.), p.387. Plenum Press, New York, 1986.
- (4) Thompson, T.E.; Brown, R.E. in "New Trends in Ganglioside Research: Neurochemical and Neuroregenerative Aspects" (R. Ledeen, E. Hogan, G. Tettamati, A. Yates and R. Yu eds.) Fidia Res. Series, Vol.14, p.65. Liviana Press, Padova, 1988.
- (5) Thompson, T.E.; Tillack, T.W. *Annu.Rev.Biophys.Chem.* **1985**, *14*, 361.
- (6) Marsh, D.; Watts, A.; Knowles, P.F. *Biochim.Biophys.Acta* **1976**, *858*, 161.

- (7) M.I. Kanehisa, and T.Y. Tsong, *J.Am.Chem.Soc.* **100**, 424 (1978).
- (8) Cruzeiro-Hansson, L.; Mouritsen, O.G. *Biochim.Biophys.Acta* **1988**, 944, 63.
- (9) Scott, H.L. *Biochim. Biophys. Acta* **1977**, 469, 264.
- (10) Scott, H.L. *Biochemistry* **1986**, 25, 6122.
- (11) Scott, H.L.; Jacobson, E.; Subramaniam, S. *Computers in Physics* **1988**, 12, 328.
- (12) Caille, A.; Pink, D.A.; de Verteuil, F.; Zuckermann, M.J. *Can.J.Phys.* **1980**, 58, 581.
- (13) Mouritsen, O.G. *Chem.Phys.Lipids* **1991**, 57, 178.
- (14) Heimburg, T.; Biltonen, R.L. *Biophys.J.* **1996**, 70, 84.
- (15) Heimburg, T.; Marsh, D. Thermodynamics of the interaction of proteins with lipid membranes. In "Biological Membranes. A Molecular Perspective from Computation and Experiment" (K.M. Merz, and B. Roux, eds.), p.405. Birkhauser, Boston, 1996.
- (16) Jerala, R.; Almeida, P.F.F.; Biltonen, R.L. *Biophys.J.* **1996**, 71, 609.
- (17) Sugar, I.P.; Biltonen, R.L.; Mitchard, N. *Methods in Enzymology* **1994**, 240, 569.
- (18) Sugar, I.P.; Thompson, T.E.; Biltonen, R.L. *Biophys.J.* **1999**, 76, 2099.
 Sugar, I.P., Biltonen, R.L. *Methods in Enzymology*, **2000**, 323, 340-372.
 Michonova-Alexova, E.I., Sugar, I.P. *J.Phys.Chem.B.* **2001**, 105, 10076-10083.
 Sugar, I.P., Michonova-Alexova, E., Chong, P.L.-G. *Biophys. J.* **2001**, 81, 2425-2441.
 Michonova-Alexova, E.I., Sugar, I.P. *Biophys. J.* **2002**, 83, 1820-1833.
 Sugar, I.P., Biltonen, R.L. *J.Phys. Chem. B.* **2005**, 109, 7373-7386.
 Sugar, I.P. *J. Phys. Chem. B.* **2008**, 112, 11631-11642.
- (19) Mabrey, S.; Sturtevant, J.M. *Proc. Natl. Acad. Sci. USA* **1976**, 73, 3862.
- (20) Van Dijck, P.W.M.; Kaper, A.J.; Oonk, H.A.J.; De Gier, J. *Biochim. Biophys. Acta* **1977**, 470, 58.
- (21) Wilkinson, D.A.; Nagle, J.F. *Biochemistry* **1979**, 18, 4244.
- (22) Knoll, W.; Ibel, K.; Sackmann, E. *Biochemistry* **1981**, 20, 6379.
- (23) Lu, D.; Vavasour, I.; Morrow, M.R. *Biophys.J.* **1995**, 68, 574.
- (24) Sankaram, M.B.; Thompson, T.E. *Biochemistry* **1992**, 31, 8258.
- (25) Sankaram, M.B.; Marsh, D.; Thompson, T.E. *Biophys. J.* **1992**, 63, 340.
- (26) Mendelsohn, R.; Maisano, J. *Biochim. Biophys. Acta* **1978**, 506, 192.
- (27) Brumm, T.; Jørgensen, K.; Mouritsen, O.G.; Bayerl, T.M. *Biophys.J.* **1996**, 70, 1373.
- (28) Vaz, W.L.C.; Melo, E.C.C. ; Thompson, T.E. *Biophys. J.* **1989**, 56, 869.
- (29) Schram, V.; Lin, H.-N.; Thompson, T.E. *Biophys.J.* **1996**, 71, 1811.
- (30) Pikhova, B.; Marsh, D.; Thompson, T.E. *Biophys. J.* **1996**, 71, 892.
- (31) Pedersen, S.; Jørgensen, K.; Bø kmark, T.R.; Mouritsen, O. *Biophys. J.* **1996**, 71, 554.
- (32) Gliss, C.; Clausen-Schaumann, H.; Gunther, R.; Odenbach, S.; Rand, O.; Bayerl, T.M. *Biophys.J.* **1998**, 74, 2443.
- (33) Von Dreele, P.H. *Biochemistry* **1978**, 17, 3939.
- (34) Ipsen, J.H.; Mouritsen, O.G. *Biochim. Biophys. Acta* **1988**, 944, 121.
- (35) Brumbaugh, E.E.; Johnson, M.L.; Huang, C. *Chem.Phys.Lipids* **1990**, 52, 69.
- (36) Brumbaugh, E.E.; Huang, C. *Methods in Enzymology* **1992**, 210, 521.
- (37) Priest, R. *Mol. Cryst. Liq. Cryst.* **1980**, 60, 167.

- (38) Sugar, I.P.; Monticelli, G. *Biophys. J.* **1985**, *48*, 283.
 (39) Jan, N.; Lookman, T.; Pink, D.A. *Biochemistry* **1984**, *3*, 3227.
 (40) Jørgensen, K.; Sperotto, M.M.; Mouritsen, O.G.; Ipsen, J.H.; Zuckermann, M.J. *Biochim. Biophys. Acta* **1993**, *1152*, 135.
 (41) Risbo, J.; Sperotto, M.; Mouritsen, O.G. *J.Chem.Phys.* **1995**, *103*, 3643.
 (42) Huang, K. in "Statistical Mechanics", p.336. Wiley, New York, 1963.
 (43) Nagle, J.F.; Scott, Jr. H.L. *Biochim.Biophys.Acta* **1978**, *513*, 236.
 (44) Kasteleyn, P.W. *J. Math. Phys.* **1963**, *4*, 287.
 (45) Glauber, R.J. *J.Math.Phys.* **1963**, *4*, 294.
 (46) Kawasaki, K. in "Phase Transitions and Critical Phenomena" (C. Domb and M.S. Green, eds.), Vol.2, p.443. Academic Press, London, 1972.
 (47) Sun, H.; Sugar, I.P. *J.Phys.Chem.* **1997**, *101*, 3221.
 (48) Mezei, M.; Beveridge, D.L. *Annals of The New York Academy of Sciences* **1986**, *482*, 1.
 (49) Ferrenberg, A.M.; Swendsen, R.H. *Phys.Rev.Lett.* **1988**, *61*, 2635.
 (50) Suurkuusk, J.; Lentz, B.R.; Barenholz, Y.; Biltonen, R.L.; Thompson, T.E. *Biochemistry* **1976**, *15*, 1393.
 (51) Mouritsen, O.G.; Jørgensen, K. *BioEssays* **1992**, *14*, 129.
 (52) D. Stauffer, In "Introduction to Percolation Theory" p.110. Taylor and Francis, London and Philadelphia, 1985.
 (53) Papahadjopoulos, D.; Jacobson, K.; Nir, S.; Isac, T. *Biochim. Biophys. Acta* **1973**, *311*, 330.
 (54) Blok, M.C.; Van der Neut-Kok, E.C.; Van Deenen, L.L.; De Gier, J. *Biochim. Biophys. Acta* **1975**, *406*, 187.
 (55) Van Hoogevest, P.; De Gier, J.; De Kruijff, B. *FEBS Lett.* **1984**, *171*, 160.
 (56) El-Mashak, E.M.; Tsong, T.Y. *Biochemistry* **1985**, *24*, 2884.
 (57) Georgallas, A.; McArthur, J.D.; Ma, X.P.; Nguyen, C.V.; Palmer, G.R.; Singer, M.A.; Tse, M.Y. *J.Chem.Phys.* **1987**, *86*, 7218.
 (58) Bramhall, J.; Hofmann, J.; DeGuzman, R.; Montestrucque, S.; Schell, R. *Biochemistry* **1987**, *26*, 6330.
 (59) Clerc, S.G.; Thompson, T.E. *Biophys.J.* **1995**, *68*, 2333.
 (60) Doniach, S. *J.Chem.Phys.* **1978**, *68*, 4912.
 (61) Anthony, F.H.; Biltonen, R.L.; Freire, E. *Analytical Biochemistry* **1981**, *116*, 161.
 (62) Heimburg, T. *Biochim.Biophys.Acta* **1998**, *1415*, 147.
 (63) Nagle, J.F.; Tristram-Nagle, S., *Biochim.Biophys.Acta* **2000**, *1469*, 159.

References to Chapter 3.

- (1) Brose, N.; Betz, A.; Wegmeyer, H. *Curr.Opin.Neurobiol.* **2004**, *14*, 328-340.
 (2) Dorn, G. W., II; Mochly-Rosen, D. *Annu.Rev.Physiol.* **2002**, *64*, 407-429.
 (3) Denisov, G.; Wanaski, S.; Luan, P.; Glaser, M.; McLaughlin, S. *Biophys.J.* **1998**, *74*, 731-744.
 (4) Sugar, I. P.; Mizuno, N. K.; Momsen, M. M.; Momsen, W. E.; Brockman, H. L. *Chem.Phys.Lipids* **2003**, *122*, 53-64.
 (5) Crisp, D. J. A two dimensional phase rule. II. Some applications of a two

dimensional phase rule for a single surface, in *Surface Chemistry*, London, editor; Butterworths: **1949**; pp. 23-35.

(6) Anderson, T. G.; McConnell, H. M. *Biophys.J.* **2002**, *83*, 2039-2052.

(7) Sugar, I. P.; Mizuno, N. K.; Momsen, M. M.; Brockman, H. L. *Biophys.J.* **2001**, *81*, 3387-3397.

(8) Crisp, D. J. A two dimensional phase rule. I. Derivation of a two dimensional phase rule for plane interfaces, in *Surface Chemistry*, London, editor; Butterworths: **1949**; pp.17-22.

(9) Sugár, I. P.; Mizuno, N. K.; Brockman, H. L. *Biophys.J.* **2005**, *89*, 3997-4005.

Sugar, I.P., Brockman, H.L. *J. Phys. Chem. B.* **2007**, *111*, 4073-4081.

(10) Galla, H.-J.; Hartmann, W.; Theilen, U.; Sackmann, E. *J.Membr.Biol.* **1979**, *48*, 215-236.

(11) MacCarthy, J. E.; Kozak, J. J. *J.Chem.Phys.* **1982**, *77*, 2214-2216.

(12) Vaz, W. L. C.; Clegg, R. M.; Hallmann, D. *Biochemistry* **1985**, *24*, 781-786.

(13) Peters, R.; Beck, K. *Proc.Natl.Acad.Sci.U.S.A.* **1983**, *80*, 7183-7187.

(14) Press, W. H.; Flannery, B. P.; Teukolsky, S. A.; Vetterling, W. R.

Multidimensional integrals, in *Numerical Recipes*, Cambridge University Press: New York, **1989**; Chapter 4.6.

(15) Momsen, M. M.; Dahim, M.; Brockman, H. L. *Biochemistry* **1997**, *36*, 10073-10081.

(16) Smaby, J. M.; Brockman, H. L. *Biophys.J.* **1990**, *58*, 195-204.

(17) Sugar, I. P.; Förster, W.; Neumann, E. *Biophys.Chem.* **1987**, *26*, 321-335.

(18) Papahadjopoulos, D.; Jacobson, K.; Nir, S.; Isac, T. *Biochim.Biophys.Acta* **1973**, *311*, 330-348.

(19) Kensil, C. R.; Dennis, E. A. *J.Biol.Chem.* **1979**, *254*, 5843-5848.

(20) Small, D. H.; Phillips, M. *Adv.Colloid Interface Sci.* **1992**, *41*, 1-8.

(21) Borgström, B. *Gastroenterology* **1980**, *78*, 954-962.

(22) Hoang, K. C.; Malakhov, D.; Momsen, W. E.; Brockman, H. L. *Anal.Chem.* **2006**, *78*, 1657-1664.

(23) Feller, W. Probability distribution in R^r , in *An introduction to probability theory and its applications*, Feller, W., editor; John Wiley & Sons: New York, **1966**; Vol. 2, Chapter 5, pp. 125-164.

(24) Press, W. H.; Flannery, B. P.; Teukolsky, S. A.; Vetterling, W. R.

Incomplete beta function, in *Numerical Recipes*, Cambridge University Press: New York, **1989**; Chapter 6.3.

(25) The subroutine calculating the derivatives of the incomplete beta function can be downloaded from. www.stat.ucla.edu/journals/jss/ 3, **2007**.

References to Chapter 4.

(1) DeWitt, A. E.; Dong, J. Y.; Wiley, H. S.; Lauffenburger, D. A. *J Cell Sci* **2001**, *114*, 2301.

(2) Dong, J.; Opresko, L. K.; Dempsey, P. J.; Lauffenburger, D. A.; Coffey, R. J.; Wiley, H. S. *Proc Natl Acad Sci U S A* **1999**, *96*, 6235.

(3) Janes, K. A.; Gaudet, S.; Albeck, J. G.; Nielsen, U. B.; Lauffenburger, D. A.; Sorger, P. K. *Cell* **2006**, *124*, 1225.

- (4) Maheshwari, G.; Wiley, H. S.; Lauffenburger, D. A. *J Cell Biol* **2001**, *155*, 1123.
- (5) Wiley, H. S.; Shvartsman, S. Y.; Lauffenburger, D. A. *Trends Cell Biol* **2003**, *13*, 43.
- (6) Monine, M. I.; Berezhkovskii, A. M.; Joslin, E. J.; Wiley, H. S.; Lauffenburger, D. A.; Shvartsman, S. Y. *Biophys J* **2005**, *88*, 2384.
- (7) Oehrtman, G. T.; Wiley, H. S.; Lauffenburger, D. A. *Biotechnol Bioeng* **1998**, *57*, 571.
- (8) Griffith, L. G.; Swartz, M. A. *Nat Rev Mol Cell Biol* **2006**, *7*, 211.
- (9) Nakashiro, K.; Hara, S.; Shinohara, Y.; Oyasu, M.; Kawamata, H.; Shintani, S.; Hamakawa, H.; Oyasu, R. *Am J Pathol* **2004**, *165*, 533.
- (10) Shaw, K. R.; Wrobel, C. N.; Brugge, J. S. *J Mammary Gland Biol Neoplasia* **2004**, *9*, 297.
- (11) Wrobel, C. N.; Debnath, J.; Lin, E.; Beausoleil, S.; Roussel, M. F.; Brugge, J. S. *J Cell Biol* **2004**, *165*, 263.
- (12) Zhu, T.; Starling-Emerald, B.; Zhang, X.; Lee, K. O.; Gluckman, P. D.; Mertani, H. C.; Lobie, P. E. *Cancer Res* **2005**, *65*, 317.
- (13) Nilson, L. A.; Schupbach, T. *Curr Top Dev Biol* **1999**, *44*, 203.
- (14) Spradling, A. C. Developmental genetics of oogenesis. In *The Development of Drosophila Melanogaster*; Cold Spring Harbor Laboratory Press, Plainview, 1993; pp 1.
- (15) Berezhkovskii, A. M.; Batsilas, L.; Shvartsman, S. Y. *Biophys Chem* **2004**, *107*, 221.
- (16) Bertoni, S.; Gabella, G. *J Anat* **2001**, *199*, 725.
- (17) Hijiya, K.; Okada, Y.; Tankawa, H. *J Electron Microsc (Tokyo)* **1977**, *26*, 321.
- (18) Ito, S.; Schofield, G. C. *J Cell Biol* **1974**, *63*, 364.
- (19) Steimer, A.; Haltner, E.; Lehr, C. M. *J Aerosol Med* **2005**, *18*, 137.
- (20) Bement, W. M.; Mooseker, M. S. The cytoskeleton of the intestinal epithelium: components, assembly, and dynamic rearrangements. In ; Hesketh, J. E., Pryme, I. F., Eds.; Elsevier, 1996; Vol. 3; pp 359.
- (21) Press, W. H.; Flannery, B. P.; Teukolsky, S. A.; Vetterling, W. T. *Numerical Recipes*; Cambridge University Press: Cambridge, 1989.
- (22) Sugár, I.P., Sealfon, S.C. *J. Phys. Chem. B.* **2009**, *113*, 10946-10956.